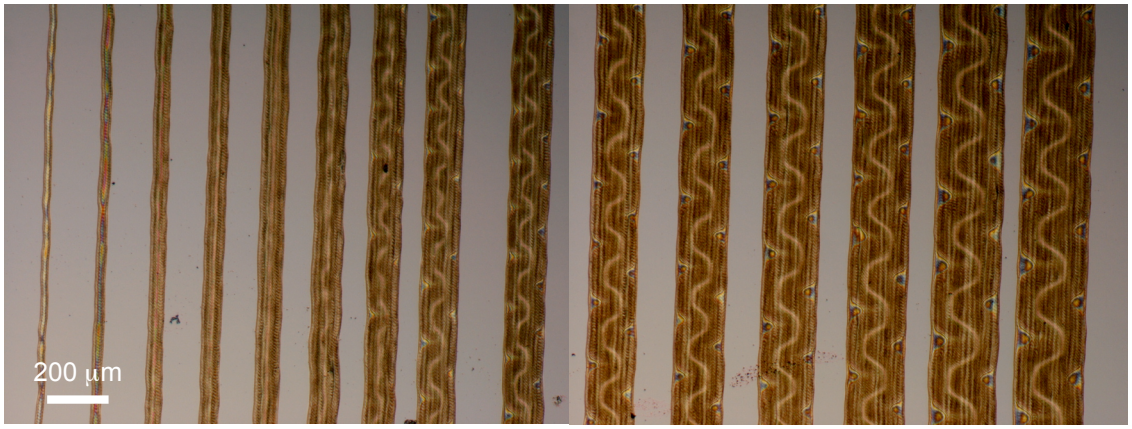

Figure 5.2.15 OM images of linear blister channels produced in 1200 nm PECVD oxide films on Si(100). The channel width was increased by laterally overlapping single pass channels. The leftmost channel was produced with a single pass of the sample through the focused laser beam. The number of lateral passes increases monotonically up to 15 passes for the rightmost blister channel. The telephone cord instability emerged when the channel width exceeds ~ 90

5.2.4 Linear blister channels

By overlapping circular blister features produced at normal laser incidence, linear blister channels were produced on samples with 1200 nm thermally grown and PECVD oxide [75]. A schematic of the technique is provided in Figure 5.2.14, while OM images of linear blister channels are provided in Figure 5.2.15. Overlap of circular blisters was achieved by translating the sample through the focused laser beam at a constant speed (typically 10 mm/s) under modest focusing conditions (using a plano-convex lens with focal length of 35-40 cm, yielding a focused beam diameter ($1/e^2$) of around 50-70 μm). The optimal laser fluence for channel production was found to be 0.35-0.4 J/cm^2, at the low end of the fluence range where single isolated blisters were produced (see Chapter 5.2.2). At a laser repetition rate of 1 kHz, a scan velocity of 10 mm/s yields a pulse-to-pulse overlap of 10μm on the sample surface. Under the laser focusing conditions discussed above, high sample translation speeds (≥ 20 mm/s) resulted in channels with non-uniform surfaces (isolated blisters were spaced too far apart); while slower translation speeds (≤ 5 mm/s) often resulted in fracture of the oxide film. The observed fracture produced at slower translation speeds was attributed to excessive accumulated fluence which produced excessive local heating or strain in the oxide film. Attempts to produce similar channels on

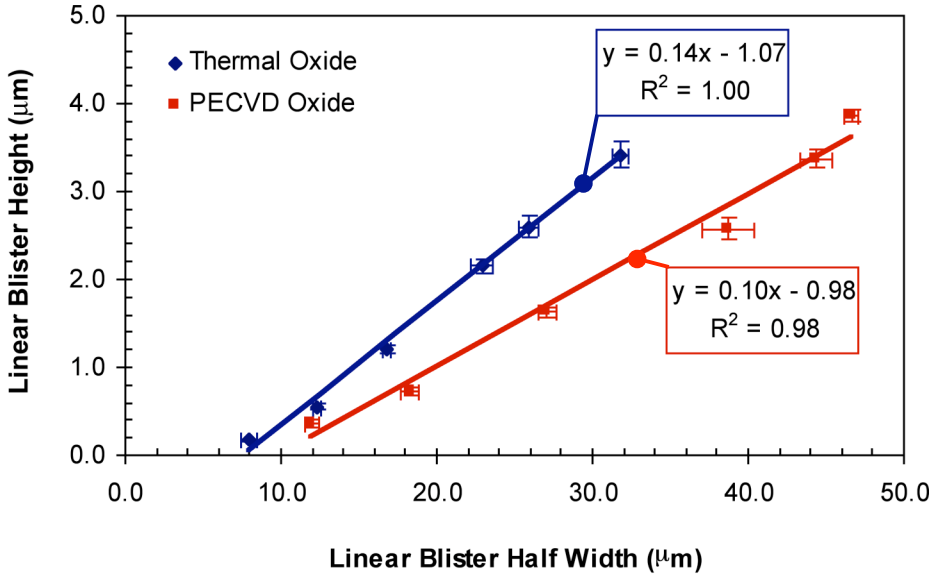

Figure 5.2.16 Measured linear blister height as a function of linear blister half width for blister produced with a fs pulsed laser on Si(100) with a 1200 nm thermal oxide film (laser fluence = 0.4 J/cm^2, lateral overlap = 10 μm) and Si(100) with 1200 nm PECVD oxide ((laser fluence = 0.4 J/cm^2, lateral overlap = 20 μm). Linear fits provided to the data indicate a minimum blister half width for fs laser induced buckling of b_0 = 7.64 μm for the thermal oxide film, and b_0 = 9.8 μm for the PECVD oxide film.

samples with thinner oxide films were not successful, as laser conditions were not experimentally determined which did not result in the fracture of the film when two circular blisters were overlapped.

Channels produced with a single pass or translation of the sample through the focused laser beam had widths of around 20 μm and maximum heights of around 300-400 nm. Wider channels were produced by laterally overlapping single pass channels with a typical spacing of around 10-20 μm. In Figure 5.2.15, linear blister channels produced with up to 15 laterally overlapped passes are shown. The measured height of the channels as a function of channel radius (or half width) for linear blister channels produced with 1200 nm thermally grown and PECVD oxide films on Si(100) is shown in Figure 5.2.16. Channels up to around 90 μm in width produced in 1200 nm PECVD oxide films, and around 60 μm width in thermally grown oxide films exhibited the Euler mode of thin film buckling [145, 149], while channels of width exceeding these values resulted in a channel with the telephone cord mode [149, 150, 152, 245, 246]. The presence of these

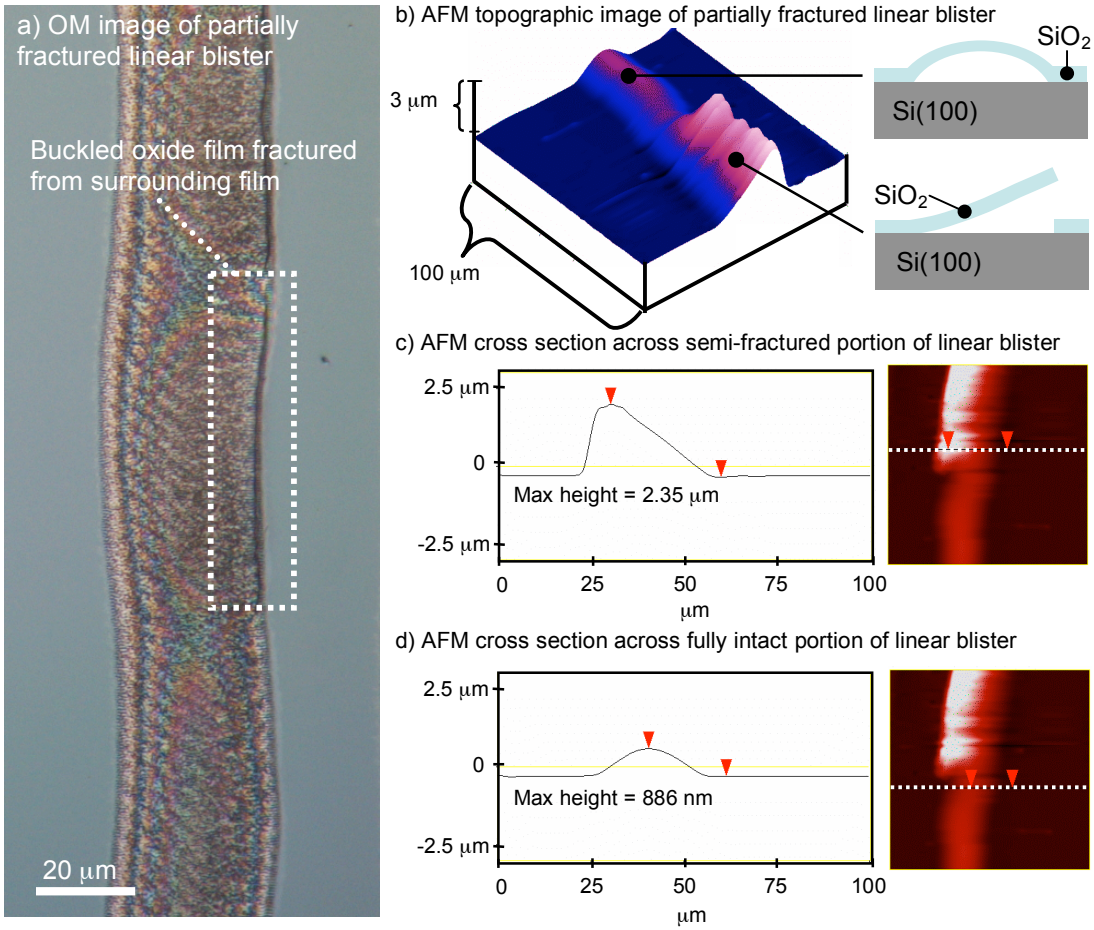

Figure 5.2.17 Examples of fractured blister channels produced in Si(100) with 1200 nm thermally grown oxide at a laser fluence of 0.40 J/cm^2, translation velocity of 6 mm/s, 2-pass channel with a lateral overlap of 10 μm. a) OM image of linear blister channel height where location of partial fracture is indicated. b) AFM topographic image of partially fractured linear blister channe. c) AFM cross section over semi-fractured portion of linear blister. d) AFM cross section over fully intact portion of linear blister channel.

buckling modes will be discussed in the context of thin film buckling mechanics in the following section (Chapter 5.2.5)

The 1200 nm PECVD oxide film was found to be superior for linear blister channel production relative to the 1200 nm thermally grown oxide on silicon. For the 1200 nm thermally grown oxide film, the delaminated oxide film often fractured during the production of multiple lateral pass blister channels. Typically the fracture was observed along the outer edge of the film delaminated by the first pass of the laser across the sample surface after the application of additional laterally overlapped passes. An example of a partially fractured linear blister channel produced in 1200 nm thermally grown oxide film are presented in Figure

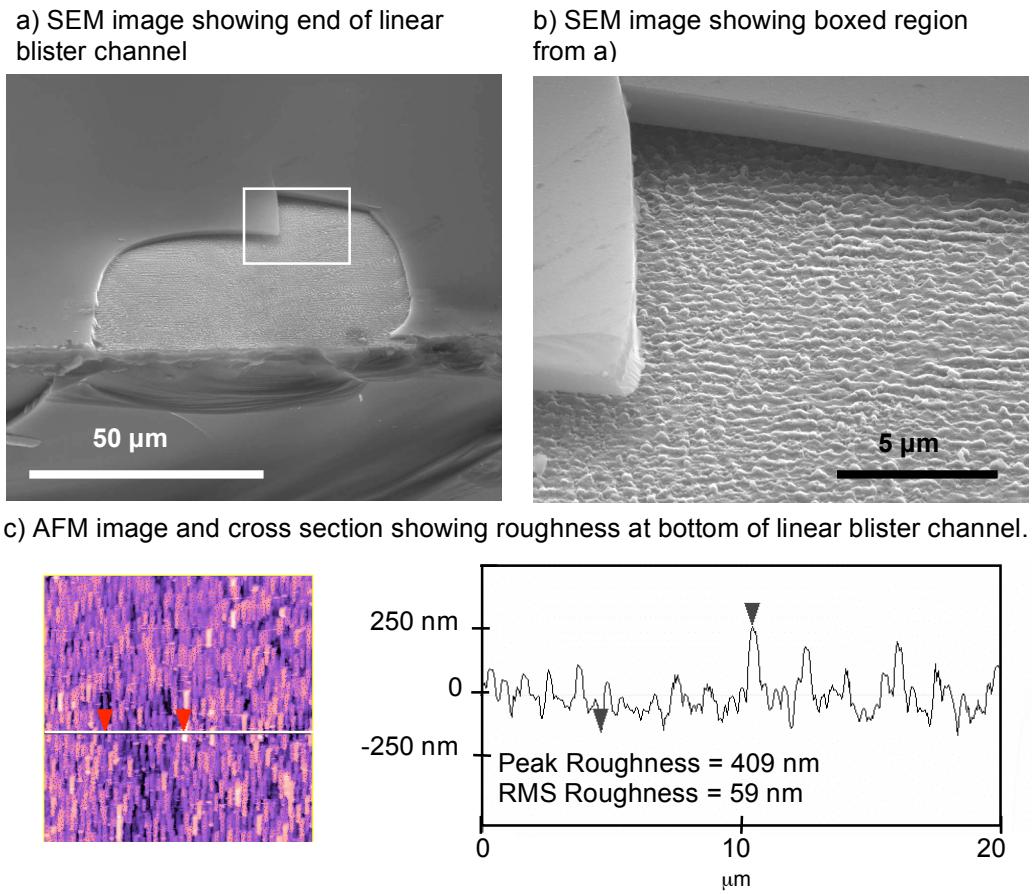

Figure 5.2.18 SEM and AFM characterization of interior of linear blister channels produced on Si(100) with 1200 nm PECVD oxide. a) SEM image showing end of blister channel produced with a laser fluence of 0.3 J/cm^2, a translation speed of 10 mm/sec, with 4 laterally overlapped passes at 20 µm lateral spacing. Image taken with sample tilted at 59°. b) SEM image showing close up image from boxed region in a). c) AFM of bottom surface of linear blister channel produced with laser fluence of = 0.19 J/cm^2, and a translation speed of 5 mm/s. The laser was passed over the same region twice to remove the oxide film and expose the bottom surface of the channel.

5.2.17. Similar fracture phenomena in delaminated oxide films have been observed by other groups [151], however the location of the fracture was typically along the line of maximum vertical displacement of the delaminated film, in contrast to our observations where the ridge cracks form along one side of the linear blister. This might be expected from the manner in which our linear blister channels our produced (i.e. by laterally overlapping several single pass blister channels, see schematic in Figure 5.2.14 for more detail) in contrast to a load applied by a wedge as in previously published work [151]. The portion of the blister channel that has been fractured appears flat relative to the portion of the

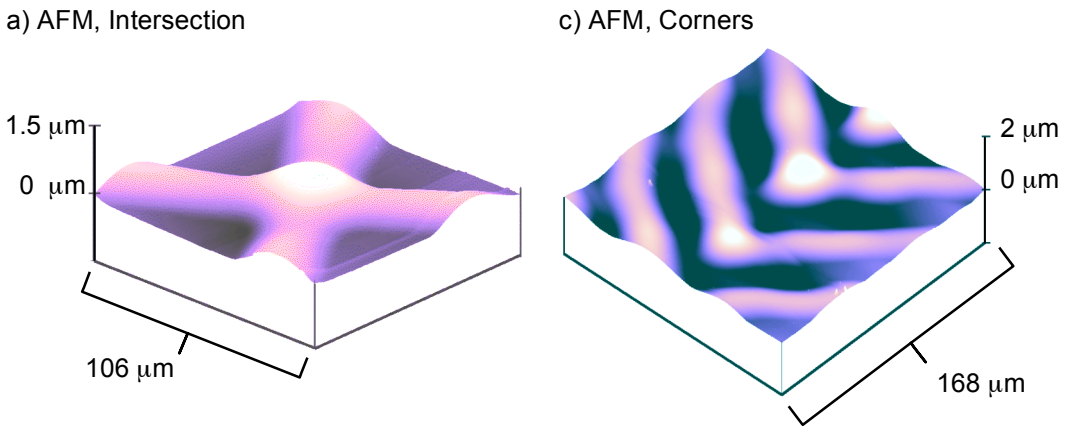

Figure 5.2.19 a) AFM topographic image of an intersection between 2 linear blister channels (1 pass intersecting with a 2 pass) written in Si(100) with 1200 nm PECVD oxide. b) AFM topographic image of linear blister channels with corners. For both a) and b), the laser fluence was 0.40 J/cm^2 with a translation velocity of 10 mm/s.

channel that remained intact, suggesting that the delaminated oxide undergoes elastic deformation alone. This may further indicate that the entire film may not achieve temperatures appropriate for melting.

With respect to the films examined here, the 1200 nm thermally grown oxide film may be more prone to fracture due to presence of greater intrinsic compressive stress in the film relative to the oxide films prepared via PECVD [242]. These films were prepared by the Michigan Nanofabrication Facility (MNF), and the intrinsic film stresses were characterized Brian VanderElzen (Lead Research Engineer, MNF) and Cedric Whitney (Senior Process Engineer, MNF) using the technique of wafer curvature indicating a compressive stress of 300 MPa for the low temperature (200 °C) PECVD oxide, and 380 MPa for the thermally grown oxide. Calculation of this intrinsic stress based on linear blister channel dimensions is discussed below in Chapter 5.2.5.

The interior surfaces of the channels were characterized using SEM and AFM. A SEM image showing the end of a linear blister channel written off the edge of a Si(100) wafer with 1200 nm is presented in Figure 5.2.18. From Figure 5.2.18 b), it can be seen that the bottom surface of the delaminated oxide film is very smooth, with roughness less than 10 nm. The bottom (or substrate) surface of the linear blister channel exhibits roughness due to the ablation event initiated by the incident laser pulse. This roughness appears periodic in nature, yielding

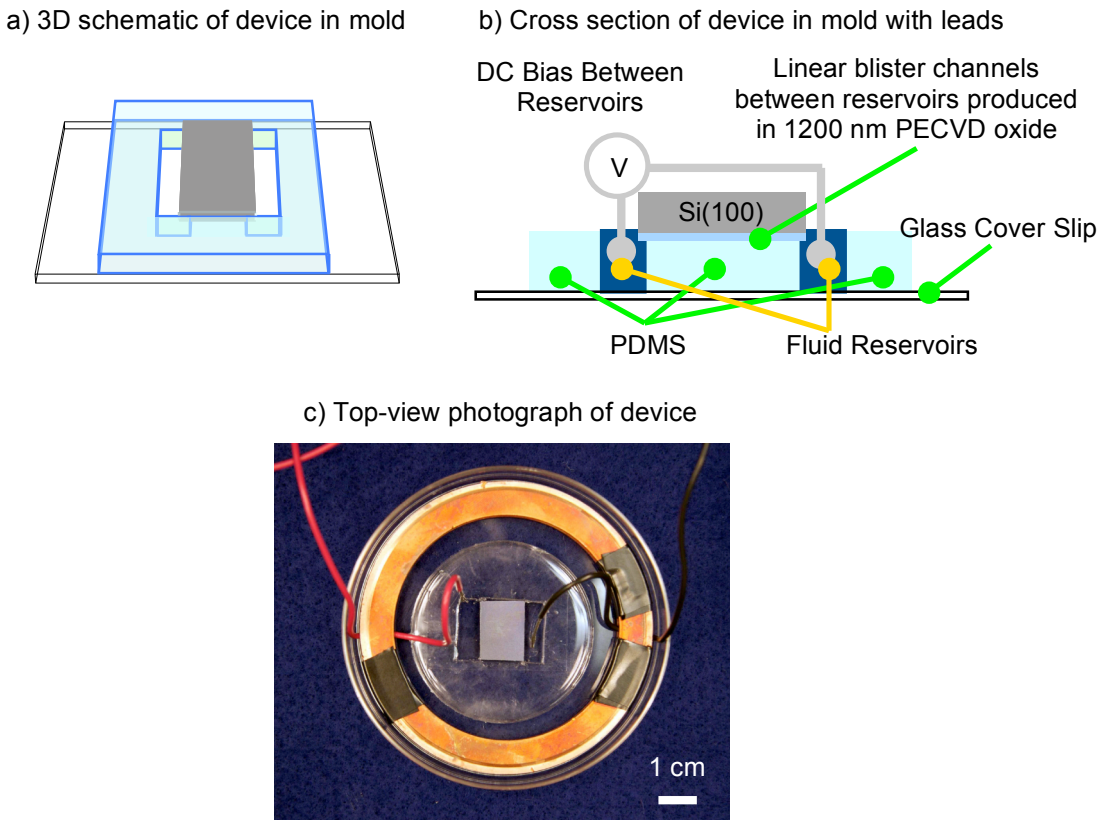

Figure 5.2.20 a) Schematic showing fluidic device in dual reservoir mold mounted on glass cover slip. The channels through which fluid flows are facing downward to facilitate viewing with an inverted fluorescence microscope. b) Side-view of device. c) Top-view photograph of device showing leads, which are clamped in with two copper gaskets for tension relief.

ripples or laser induced periodic surface structures (LIPSS) [46, 130]. Atomic force microscopy of the bottom surface of a channel for which the oxide film was intentionally removed (by over-exposing the surface to the laser) showed a peak roughness of around 409 nm, while the RMS roughness was around 59 nm (see Figure 5.2.17 c)). If a linear blister channel is written off the edge of a substrate, we expect that exposure to air produces a native oxide on all interior surfaces within 1 μs (assuming a sticking coefficient of 1 [247]). As such, the interior of the blister channel is expected to have the surface properties of SiO_2.

The technique for producing linear blister channels was used to generate simple microfluidic channels in 1200 nm PECVD oxide films on Si(100) [75]. Figure 5.2.19 shows examples of device elements such as channel intersections and corners that were produced by varying the translation path of the sample through the focused laser beam. Experiments were performed to determine if the

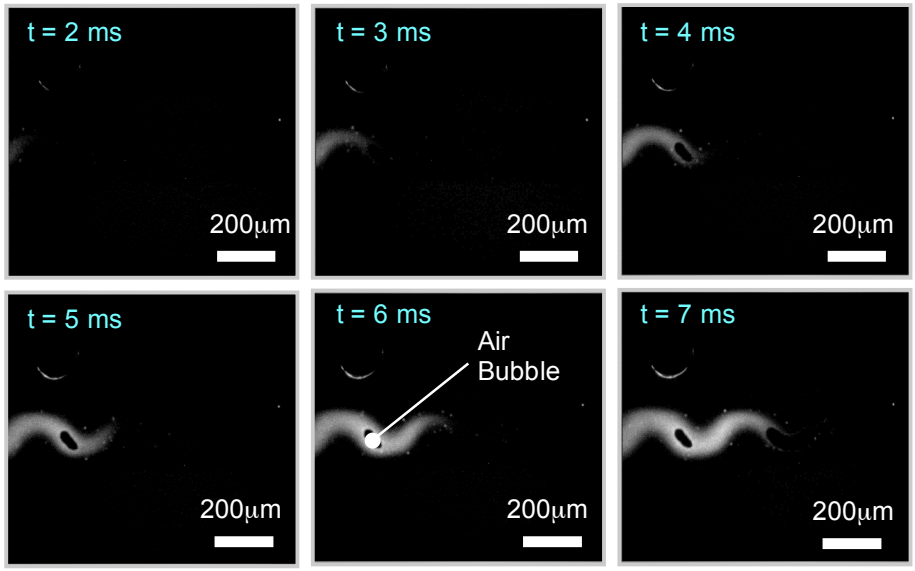

Figure 5.2.21 Time-lapse fluorescence microscopy of 20 nm carboxolate modified polystyrene spheres propagating in a blister channel produced on a sample with 1200 nm PECVD oxide on Si(100). A static DC electric field (20 V/cm) was applied to produce the electrophoretic flow. The delaminated oxide surface exhibits the telephone cord instability resulting in the wavy path of the nanospheres. Air bubbles are visible as the solid black regions within the channels. Some of the spheres have clumped together and travel near the outside of the flow.

channels were capable of propagating fluids. Linear channels of varying widths (single pass channel ~20 μm in width up to 22 laterally overlapped channels of width exceeding 320 μm) were drawn across a 1 cm wide sample. While recording video through an optical microscope, water was observed to fill linear channels via capillary action with flow rates ranging from 6.2 – 17.5 mm/s (± 1.6 mm/s) for channels ranging in width from 105 – 320 μm respectively.

A device was also designed for the purpose of performing electrophoresis in linear blister channels produced on Si(100) with 1200 nm PECVD oxide. In general, electrophoresis is the movement of charged particles under the influence of an electric field [248-251]. Electrophoresis experiments required a means for controlling delivery of fluids to the ends of linear blister channels. This macro-micro interfacing was achieved using a PDMS (poly(dimethysiloxane) from Dow Corning, Sylgard 184) mold with isolated fluid reservoirs. Several techniques for producing these molds were attempted, the most successful of which is discussed in Appendix A3, with a schematic of the procedure presented

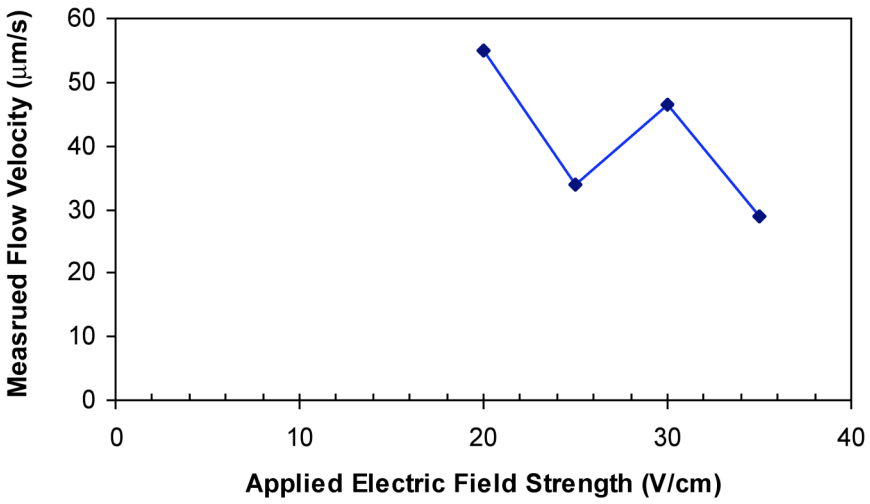

Figure 5.2.22 Measurement of electrophoretic flow velocity of 20 nm carboxolate modified polystyrene spheres through a channel ~220 μm in width and ~ 10 μm height (at maximum), as a function of applied electric field. Measurements made from time-lapse fluorescence microscopy similar to those presented in Figure 4.2.20

in Figure A3.1. A simplified diagram and picture of the device is presented in Figure 5.2.20.

Electrophoretic flow was produced by applying a DC potential difference the two reservoirs, thereby forcing charged nanospheres between the reservoirs via the only available path which was through the linear blister channels. The potential difference was established by placing wire leads into the open tops of the reservoirs. The lead were connected to a 1250 V DC power supply (Stanford Research Systems, model PS310). The charged particles used for electrophoresis experiments were fluorescent, 20 nm diameter, carboxolate modified polystyrene spheres (Fluo Spheres from Invitrogen Corp.). The nanospheres had a maximum excitation wavelength of 625 nm, and a maximum fluorescence wavelength of 645 nm. The spheres were suspended in a buffered 1 M TRIS (trishydroxymethylaminomethane) solution with a 10:1 ratio of TRIS to suspended nanospheres. The nanosphere/TRIS solution was placed in one of the reservoirs with DI water placed in the other reservoir. With the electrical leads in place in the reservoirs and separated by about 1-1.5 cm, a range of potential differences was applied (5V – 50V), yielding electric fields on the order of 5 – 50

V/cm, and currents on the order of 100's of μA. Time-lapse fluorescence microscope images showing flow of particles within the channels are shown in Figure 5.2.21.

As demonstrated by the plot in Figure 5.2.22, the flow rate of the spheres through a particular channel was observed to generally decrease with increasing potential difference. Flow rates ranging from 55 μm/sec to 28 μm/sec for potential differences ranging from 20-35 V (fields of ~ 20 V/cm – 35 V/cm) respectively. The decrease in flow velocity was attributed to the formation of air bubbles within and near the end of channels which limited flow of the spheres from the channels to the reservoirs. These bubbles formed due to current leakage into the Si(100) substrate, which resulted in local resistive heating and subsequent boiling of the water and TRIS solutions [249, 252]. Future work will attempt to minimize this effect by coating the interior surfaces of the channels with insulating materials [252] in order to achieve greater flow rates.

It was further observed that regions of delaminated film with arbitrary footprint could be created by simply "drawing" the desired feature with the fs laser across the sample surface. In this fashion, channel networks were assembled square regions of film delamination on samples with the 1200 nm PECVD oxide films. The so called "bitwise" writing technique used a reduced laser fluence (0.3 J/cm^2) and a slower scan velocity (5 mm/s) relative to the linear channel writing method. In contrast to the linear channel writing technique in which channels were produced by scanning the sample at a fixed velocity through the focused laser beam, the sample was translated in a square path (typically 50-100 μm on a side), yielding "bits" that were connected together to form desired features. An example of a simple 3-input mixing device created with the bitwise technique on Si(100) with 1200 nm PECVD oxide is presented in Figure 5.2.23. The top surface of channels produced with the bitwise writing technique possessed a non-uniform cross section with the delaminated glass film exhibiting a rumpled surface. Channel intersections were however, easier to produce with the bitwise technique than with the linear channel writing technique, where fracture of the delaminated film at channel intersections was often observed.

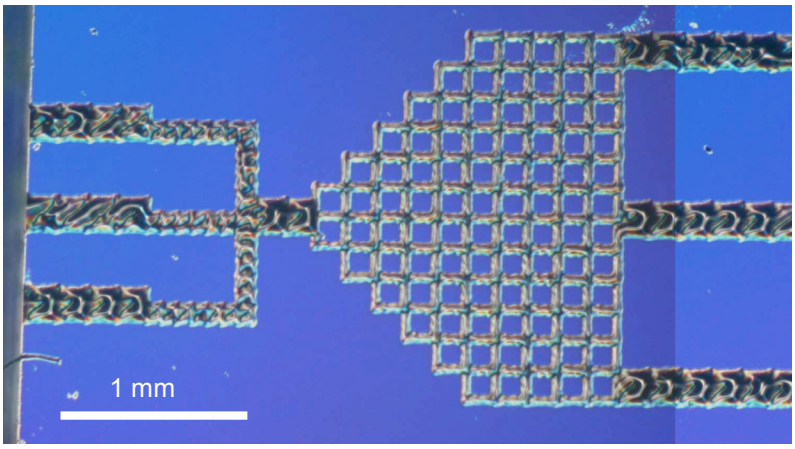

Figure 5.2.23 Nomarski OM image of three input grid device written on Si(100) with 1200 nm PECVD oxide with bitwise writing technique.

In summary, simple fluidic channel devices were created using the phenomenon of fs laser induced buckling of thin oxide films from Si(100) substrates. Channels were written at a speed of 1 cm/s, and channels width ranged from 16 – 320 μm, with channel heights ranging from 170 nm - ~15 μm respectively. Fluid flow of H_2O in linear blister channels via capillary action was observed, revealing flow rates ranging from 6.2 – 17.5 mm/s (± 1.6 mm/s) for channels ranging in width from 105 – 320 μm respectively. DC electrophoretic flow of fluorescent nanospheres in a ~220 μm wide linear channel was also demonstrated, and flow rates ranging from 55 – 29 μm/s were measured for applied electric fields ranging from 20 – 35 V/cm respectively. Air bubble formation in the channels due to current leakage from the fluid to the Silicon wafer impeded fluid flow and was cited as the source of decreasing fluid flow rates with increased applied electric field. A bitwise writing technique was also developed that provided for easier creation of channel corners and intersections. A review of other fluidic channel fabrication methods is presented elsewhere [253, 254]. Other fs laser based machining techniques have been used to create fluidic channels [255-258], but are typically orders of magnitude slower than the technique presented here (due to debris accumulation in sub-surface machining [255-257]), or involved multiple steps including the bonding of a top glass layer to a fs laser micromachined silicon substrate [258]. Future work will address the

issue of air bubble formation within the channels during electrophoresis, and will explore more complicated device designs.

5.2.5 Mechanics of fs laser induced buckling of thin oxide films.

A wide body of work has been devoted to study of the mechanical properties of thin films by characterizing the dimensions of naturally occurring [245, 246] or intentionally produced delamination or film buckling events [144-151]. These methods were applied to fs pulsed laser induced buckling of thin oxide films from Si(100) substrates in order to assess the role of the fs laser ablation on the buckling event. This work was performed in collaboration with Michael Thouless (Professor, Department of Mechanical Engineering and Department of Materials Science and Engineering, University of Michigan).

In order to investigate the role of fs laser ablation on the observed film buckling, the intrinsic compressive stress in 300 nm and 1200 nm thermally grown oxide films on Si(100)the films was inferred from the dimensions of circular blisters [259]. In a similar fashion, the intrinsic compressive stress present in 1200 nm thermally grown and PECVD oxide films was inferred from the dimensions of linear blister channels [150]. The results of these analyses indicated that the fs laser ablation event at the interface between the oxide thin film and the underlying Si(100) substrate participates in the film buckling event. Comparing the intrinsic film stress obtained from blister dimensions with measurements of the stress made ex-situ, it was apparent that the laser ablation event produced a vertical deflection or buckling of the film for smaller widths of film delamination than would be expected for the film to buckle under the naturally occurring compressive stress alone. It was further concluded the upward force of the ablation event at the substrate/film interface was responsible for this effect. A distinction should be made between buckling driven delamination of thin films and laser induced buckling. The mechanics theory used here was developed to address thin film delamination which begins at a local defect between the film and the substrate and propagates due to the energy release associated with the buckling of a compressively stressed film [259]. In

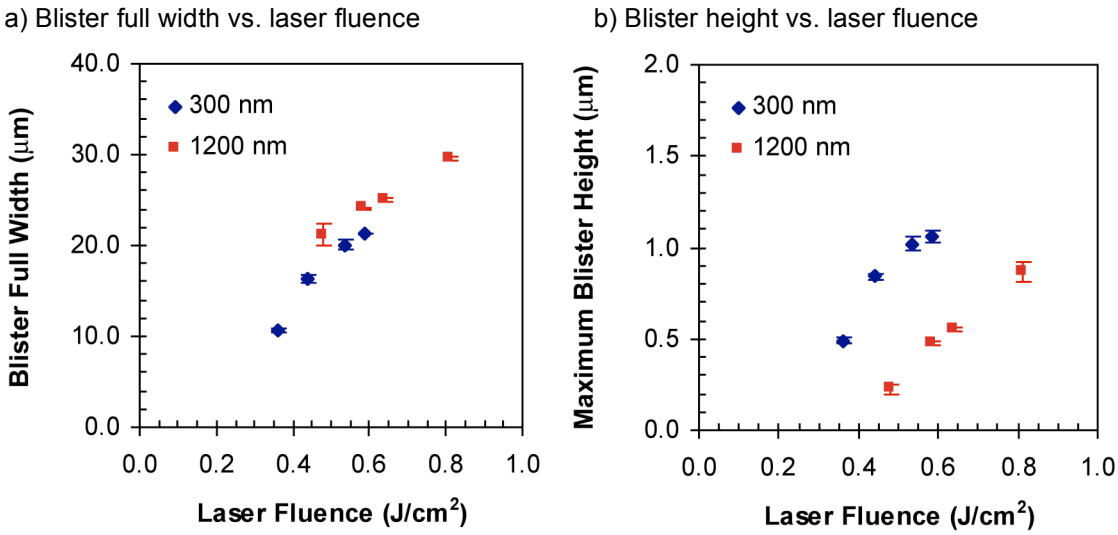

Figure 5.2.24 Dimensions of circular blisters used for study of film mechanics. a) Blister full width as a function of incident laser fluence. b) Blister maximum height as a function of incident laser fluence.

the results discussed here, propagation of the delamination beyond the region defined by the focused laser beam was not observed, and thus likely results from a different physical mechanism associated with the capped fs laser ablation that occurs at the substrate-film interface. The details of this study for both circular blisters and linear blister channels are presented in the following section.

Circular blisters were produced in 300 nm and 1200 nm thermally grown oxide films with single laser pulses at normal laser incidence. The general experimental setup for these experiments is presented in Figure 3.3.1. Briefly, the laser was focused onto the sample surface with a 20 cm focal length, plano-convex lens yielding of focused beam diameter ($1/e^2$) of 18.3 ± 0.5 μm. Variation in blister dimensions (width and height) was achieved by creating features with a range of incident laser fluences. For the 300 nm thermally grown oxide on Si(100), a range of laser fluences from 0.36 – 0.59 J/cm^2 was used, while a similar range in laser fluence from 0.48 – 0.81 J/cm^2 was used to produced blisters in the 1200 nm thermally grown oxide film. Once generated, the blister dimensions were measured via AFM, with the blister full width defined according to the location of vertical deflection of the film exceeding 10 nm. The blister dimensions (blister diameter or full width, and maximum blister height) as a

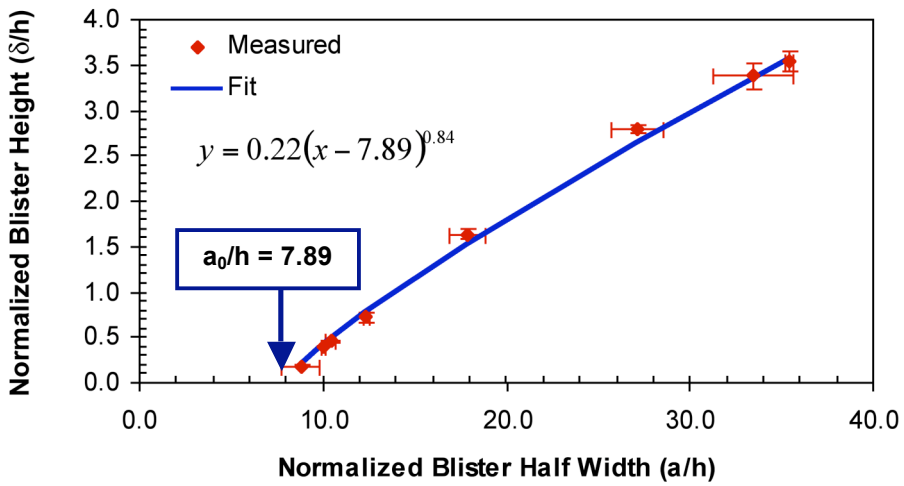

Figure 5.2.25 Normalized blister height vs. normalized blister half width for circular blisters. Note that data sets for 1200 nm and 300 nm thermal oxide on Si(100) have been combined for the normalized results. A power law fit to the measured data indicates a minimum width for buckling of $a_0/h = 7.89$.

function of laser fluence are shown in Figure 5.2.24, while the normalized blister height (normalized to the film thickness *h*) as function of normalized blister half width is provided in Figure 5.2.25. For each data point the dimensions of three blister features were measured and averaged.

Modeling the thin film as a clamped circular plate of radius *a* on a non-compliant substrate (for details on the development of these equations see [144, 259]), the critical stress for buckling is given by:

$$\sigma_C = 1.2235 \frac{E_1}{1-\nu_1^2}\left(\frac{h_1}{a}\right)^2 \qquad (5.2.1)$$

where E_1 = 70 GPa is the bulk modulous of the oxide film, and h_1 = 300 nm or 1200 nm is the thickness of the film, and ν_1 = 0.3 is the Poisson ratio of bulk SiO_2 (all properties at room temperature). Figure 5.2.25 demonstrates that once normalized to their respective film thicknesses, the blister dimensions produced on both samples with 300 nm and 1200 nm thermally grown oxide fell along the same trend line. As such, the data was regarded as a single dimensionless data set (normalized blister height a function of normalized blister half width) and calculations were performed under this assumption.

In general, buckling or vertical deflection of compressively stressed films occurs once a critical width of film is delaminated or freed from the underlying substrate [144, 146, 259]. In other words, delamination does not always lead to buckling of the film, and under the presence of intrinsic compressive stress within the film a critical width of delamination is required for buckling to occur. By determining the minimum delamination width for buckling a_0, the intrinsic compressive stress in a film can be determined via Equation 5.2.1. By applying a power law fit to the normalized blister height vs. blister half width, the minimum normalized delamination half width a_0/h for fs laser induced buckling was determined to be $a_0/h = 7.89$. Using this value, the intrinsic compressive film stress was determined from Equation 5.2.1 above (with $a/h = a_0/h = 7.89$) to be 1.5 GPa. As the minimum normalized blister half width for buckling was determined for the combined data sets for the 1200 nm and 300 nm thermal oxide films, this calculated stress of 1.5 GPa was assumed to be represent the intrinsic stress in both films.

In a previous work, the intrinsic compressive stress in thermally grown SiO_2 films on crystalline silicon substrates was found to depend on the oxide film thickness [243]. At film thicknesses exceeding 150 nm, the intrinsic compressive stress in the films was approximately 0.3 GPa [243]. This validates the normalization and combination of data sets from the 300 nm and 1200 nm thermally grown oxide films as both films would be expected to posses approximately the same intrinsic stress. Samples with thermally grown oxide (and PECVD oxide) films were obtained from the Michigan Nanofabrication Facility (MNF). These films were characterized Brian VanderElzen (Lead Research Engineer, MNF) and Cedric Whitney (Senior Process Engineer, MNF) using the technique of wafer curvature indicating a compressive stress of 300 MPa for the low temperature (200 °C) PECVD oxide, and 380 MPa for the thermally grown oxide. The magnitude of the intrinsic stress inferred from the fs laser induced blisters of the combined data sets (1.5 GPa) exceeds the literature value (~0.38 GPa). This suggests that the laser ablation event at the substrate/film interface participates in some manner during the buckling event.

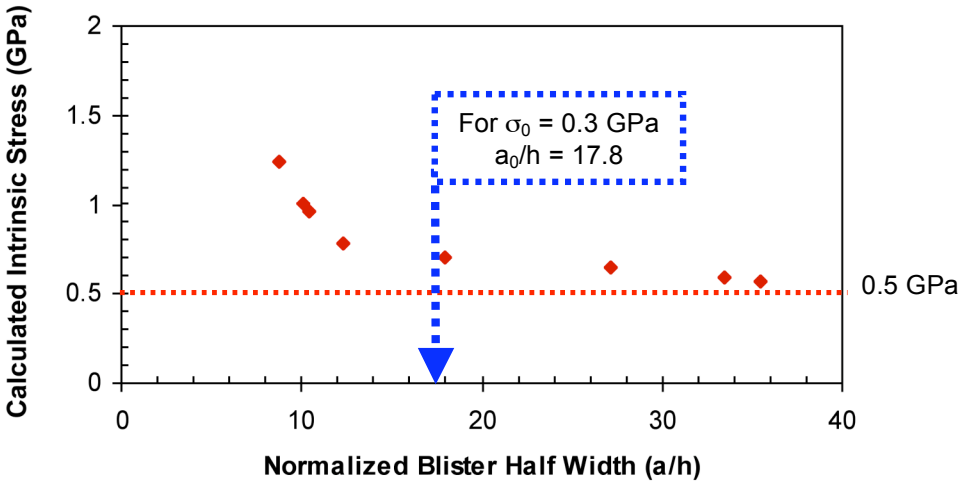

Figure 5.2.26 Calculated intrinsic film compressive film stress in thermal oxide as a function of normalized blister half width (a/h) from individual blister dimensions via Equation 5.2.2. The stress appears to asymptote to ~0.5 GPa as the normalized blister half width increases.

With respect to Equation 5.2.1, the excessive compressive stress inferred from the minimum half blister half width for fs laser induced buckling implies that the laser ablation event effectively reduces the minimum delamination width for buckling a_0. According to Equation 5.2.1, an intrinsic compressive stress of 0.3 GPa yields a minimum normalized half width for buckling of $a_0/h \approx 17.8$, significantly exceeding the estimated $a_0/h = 7.89$ presented here. It is likely that the combination of heat and upward force provided by the ablation event would produce film buckling for smaller widths of delamination that would occur in the absence of the laser/material interaction. The force provided by the ablation event is discussed further in Chapter 6.1.2, where the dynamics of fs laser ablation of silicon with thermally grown oxide films is presented.

The intrinsic (or naturally occurring [260]) film stress σ_0, was also calculated from the individual normalized blister height δ and half width a using the following expression [259]:

$$\sigma_0 = \sigma_C\left[c_1\left(\frac{\delta}{h}\right)^2 + 1\right] = 1.2235\frac{E_1}{1-\nu_1^2}\left[c_1\left(\frac{\delta}{a}\right)^2 + \left(\frac{h}{a}\right)^2\right] \qquad (5.2.2)$$

where c_1 is a constant in terms of the Poisson ratio ν_1:

$$c_1 = 0.2473(1+\nu_1) + 0.2231(1-\nu_1^2) \qquad (5.2.3)$$

The intrinsic film stress as a function of normalized blister half width for the combined data sets (both 300 nm and 1200 nm thermal oxide) is provided in Figure 5.2.26, where it is shown that the film stress asymptotes to approximately 0.5 GPa as the normalized half width increases. This inferred value differs from the measured compressive film stress of 0.3 GPa for the thermal oxide films. The asymptotic behavior for the inferred stress shown in Figure 5.2.26 does however provide additional evidence that the laser ablation event at the film/substrate interface reduces the critical width for buckling relative to that which would be expected from the intrinsic compressive film stress alone. From the plot in Figure 5.2.26 it can be seen that the calculated intrinsic film stress decreases rapidly until the normalized blister half widths exceeds the value of $a_0/h = 17.8$ (shown with arrow) expected for an intrinsic film stress of 0.3 GPa. As film buckling is expected to occur, the variation in the calculated film stress shown in Figure 5.2.26 may not be as dramatic for normalized half widths exceeding $a_0/h = 17.8$.

Two possible sources for this discrepancy between the asymptotic inferred intrinsic stress (~ 0.5 GPa) and the measured intrinsic compressive stress in the thermal oxide films (0.38 GPa) were cited; a fixed additional height may be provided to the blisters by the force of the ablation event, or the measured blister half width made via AFM may have been less than the actual half width of delamination. With respect to the former, quantifying the mechanism which introduces additional blister height would require knowledge of the thermo-physical properties of the oxide film during ablation and a measure of the force exerted on the delaminated film by the ablation event (discussed further in Chapter 6.1.2). With respect to the latter, measurements of blister widths were made relative to the location where the initial vertical deflection (exceeding 10 nm from the surrounding film) of the blister was apparent along the AFM cross section which contained maximum blister height. Some modification to the film/substrate interface was observed via optical microscopy at half widths exceeding those measured via AFM (typically 2-5 μm greater than the half width measured via AFM). This modification may be local laser induced amorphization of the underlying silicon substrate [70]. Examples of this are apparent in Figure

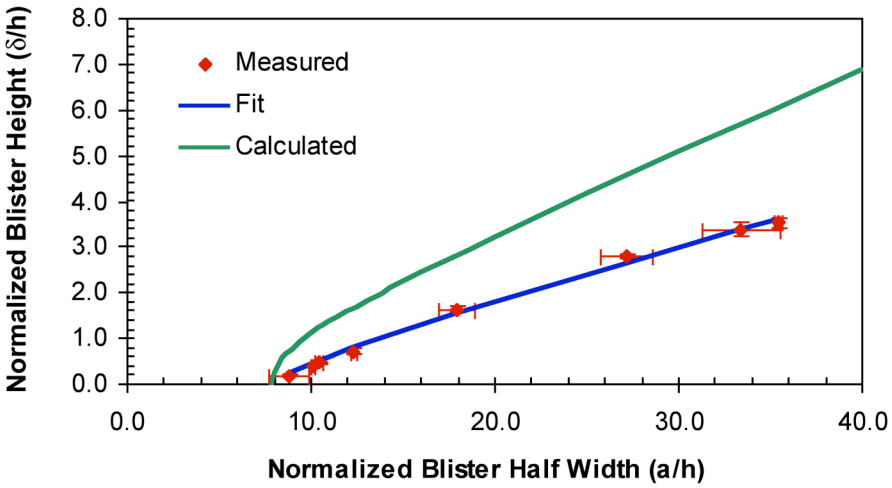

Figure 5.2.27 Measured and calculated normalized blister height as a function of normalized blister half width. Calculation of the normalized blister height made with Equation 5.2.4 using an intrinsic compressive film stress of σ_0 = 1.51 GPa based on the minimum blister half width for buckling (a_0/h = 7.89).

5.2.6 c) and d), where contrast associated with the laser ablation event is apparent in the image beyond the presumably buckled area. However, a significantly greater critical half width for buckling ($a_0/h \approx 10$) was not obtained by defining the blister half width by the according to contrast present in OM images of the blister features. Thus we assume that the force of the ablation event likely contributes a fixed additional height to the blister features, possibly due to impedance mismatch encountered by the blast wave accompanying the ablation event at the oxide film/air interface [261]. Further evidence and understanding of how the thermal oxide film responds to the shock and heat associated with the ablation event should be addressed in future work.

The predicted blister height as a function of the intrinsic film stress can be obtained by rearranging Equation 5.2.2 into the following form:

$$\frac{\delta}{h} = \sqrt{\frac{1}{c_1}\left[\sigma_0\left(\frac{1-\nu_1^2}{1.2235E_1}\right)\left(\frac{a}{h}\right)^2 - 1\right]} \qquad (5.2.4)$$

The normalized blister height δ/h as a function of the normalized blister half width was calculated using Equation 5.2.4 with an intrinsic compressive film stress (σ_0 = 1.51 GPa) inferred from the minimum normalized blister width for buckling (a_0/h = 7.89). The results of this calculation are presented in Figure

5.2.27, where the measured normalized blister height vs. half width is also presented. It is clear that the calculated blister height using an assumed intrinsic compressive of σ_0 = 1.51 GPa stress exceeds the measured height as a function of the blister half width. This observation again demonstrates that the intrinsic film stress inferred from the minimum delamination width for buckling is much higher than the actual compressive stress present in the film, further supporting the hypothesis that the laser ablation event results in a buckling event at a reduced width of oxide film delamination.

A similar mechanics analysis was applied to linear blister channels produced by overlapping isolated circular blisters on Si(100) with 1200 nm thermal oxide and 1200 nm PECVD oxide films. Linear blister channels were produced with the technique described in Chapter 5.2.3 above. For blister channels produced in the 1200 nm thermal oxide film, a laser fluence of 0.40 J/cm^2 was used to produced channels with a focused laser spot size (1/e^2) of ~20 μm , with wider channels produced by successively laterally overlapping single pass channels by 10 μm. For linear blister channels produced in the 1200 PECVD oxide film, a laser fluence of 0.40 J/cm^2 was used to produce channels with a focused laser spot size (1/e^2) of ~30 μm, with a lateral overlap of 20 μm used to create wider channels with multiple single pass channels. The analysis was applied to blister channels exhibiting the Euler buckling mode [150], and blisters exhibiting the telephone cord mode were not addressed.

The measured (via AFM) linear blister channel height δ as a function of its width *b* is presented in Figure 5.2.16 for both the thermal oxide and PECVD oxide film. Assuming the Euler buckling mode, the following equation gives the critical stress for buckling σ_c [150]:

$$\sigma_C = \frac{12}{\pi^2}\frac{E_1}{1-\nu_1^2}\left(\frac{h}{b}\right)^2 \qquad (5.2.5)$$

Where E_1 = 70 GPa is the modulus of oxide film, ν_1 = 0.3 is the Poisson ratio of the oxide film, and h = 1200 nm is the thickness of the film. The minimum width for buckling was determined to be b_0 = 7.59 μm and 9.8 μm for the 1200 nm thermally grown oxide and PECVD oxide respectively by applying a linear fits

to the measured blister height vs. width data presented Figure 5.2.16. Similar to the analysis for circular blisters, the intrinsic compressive film stress was determined using the minimum blister width b_0 for buckling in Equation 5.2.4 above [150]. This calculation yielded values of 1.58 GPa and 0.91 GPa for the intrinsic compressive film stress in the 1200 nm thermally grown and PECVD oxide films respectively. The reported values for the intrinsic compressive stress in thermally grown oxide films and PECVD oxide films are ~0.3 GPa [243] and ~0.1-0.2 GPa [242] respectively. As mentioned early, measurements of the compressive stress of oxide films produced under similar conditions via wafer curvature techniques found the intrinsic compressive stress to be 0.3 GPa for the PECVD oxide and 0.38 GPa for the thermally grown oxide film.

As with intrinsic stress inferred from analysis of circular blisters, the compressive stress inferred from the minimum delamination width for buckling exceeds the reported and measured values. The relative value of the inferred stress between the thermal and PECVD oxide were however similar to the relative reported and measured values, with the inferred stress in the PECVD oxide being approximately 2/3 the inferred stress in the thermally grown oxide film. The discrepancy between the inferred compressive film stress from the minimum width for buckling b_0 and the reported and measured values was again attributed to the fs laser ablation event encouraging film buckling at a delamination width that would not be expected to produce a vertical deflection of the delaminated film under relaxation intrinsic compressive stress alone. It should also be noted that other groups have identified discrepancies between theoretical and measured film properties for linear blisters near the critical width for buckling [147, 148]

The intrinsic film stress was also calculated from individual blister channel dimensions. The following equation gives the intrinsic film stress σ_0 in terms of the blister half width b, and maximum linear blister height δ [150]:

$$\sigma_0 = \sigma_C \left[\frac{3}{4} \left(\frac{\delta}{h} \right)^2 + 1 \right] = \frac{\pi^2}{12} \frac{E_1}{1-\nu_1^2} \left[\frac{3}{4} \left(\frac{\delta}{b} \right)^2 + \left(\frac{h}{b} \right)^2 \right] \qquad (5.2.6)$$

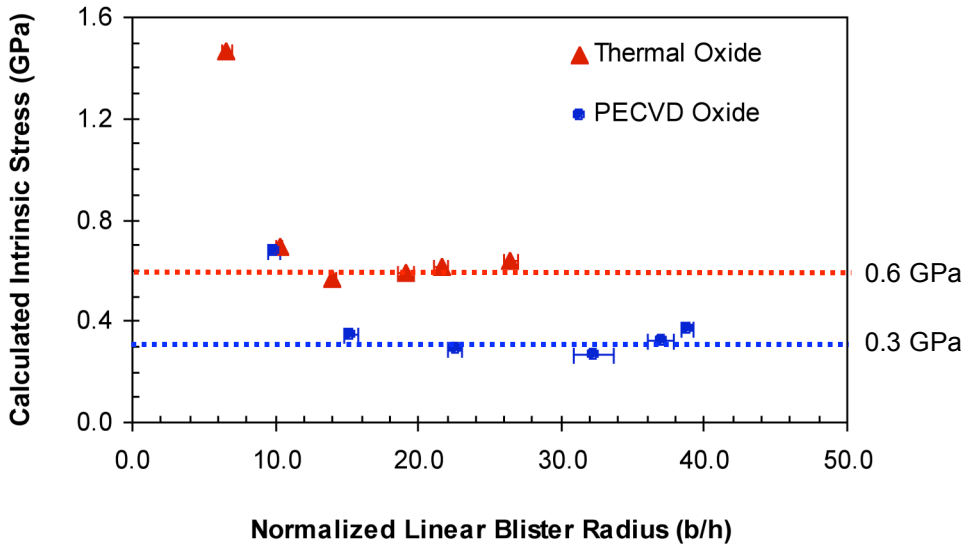

Figure 5.2.28 Calculated intrinsic compressive film stress as a function of normalized linear blister half width. Calculation of the intrinsic compressive film stress made with Equation 4.2.6.

where E_1 = 70 GPa is the modulus of oxide film, ν_1 = 0.3 is the Poisson ratio of the oxide film, and h = 1200 nm is the thickness of the film. Figure 5.2.28 shows the inferred intrinsic film stress as a function of the normalized blister half width for the 1200 nm thermally grown and PECVD oxide films. For both films, the intrinsic compressive stress begins at a higher value (σ_0 (b/h = 6.62) = 1.47 GPa for thermal oxide film, and σ_0 (b/h = 9.96) = 0.68 GPa) and quickly asymptotes to a lower value (σ_0 (b/h ≥ 10.3) ≈ 0.6 GPa for the thermal oxide film, and σ_0 (b/h ≥ 15.2) ≈ 0.3 GPa for the PECVD oxide film). Recall that for circular blisters produced in the 300 nm and 1200 nm thermally grown oxide films, the intrinsic film stress inferred from the blister dimensions also showed an asymptotic behavior, with σ_0 ≈ 0.6 GPa as the normalized blister half width increased (see Figure 5.2.26).

The asymptotic inferred intrinsic values obtained here (σ_0 (b/h ≥ 10.3) ≈ 0.6 GPa for thermal oxide film, and σ_0 (b/h ≥ 15.2) ≈ 0.3 GPa) again exceed the reported (~0.3 GPa for thermal oxide films greater than 147 nm in thickness [243], ~0.1-0.2 GPa for the PECVD oxide [242]) and measured values (0.38 GPa for thermal oxide films greater than 147 nm in thickness, 0.3 GPa for the PECVD oxide). This discrepancy is consistent with the conclusion drawn earlier; the laser

ablation event contributes an additional fixed height to linear blister channels for normalized channels widths exceeding the delamination width which would result in buckling of the film in the absence of fs laser irradiation (b/h ≈ 17.8 using σ_c = σ_0 = 0.3 GPa in Equation 5.2.5).

The interface fracture toughness was inferred for the 1200 nm thermally grown and PECVD oxide films by calculating the lateral energy release rate at the from the linear blister channel dimensions [150]. The energy per area G_0 stored in the film in the unbuckled state of equibiaxial compression that is available for release under plane-strain conditions is given in terms of the film thickness h, the bulk modulus E_1, the Poisson ratio ν_1, and the intrinsic film stress σ_0 [150]:

$$G_0 = \frac{\sigma_0^2 h}{2E_1}\left(1-\nu_1^2\right) \tag{5.2.7}$$

The energy release rate G_L along the sides of linear blisters in the buckled state for the Euler mode is given by:

$$G_L = G_0\left(1-\frac{\sigma_C}{\sigma_0}\right)\left(1+3\frac{\sigma_C}{\sigma_0}\right) \tag{5.2.8}$$

where σ_c is given by Equation 5.2.5 above. The energy release rate G_{SS} at the leading tip of linear blisters in the buckled state for the Euler mode is given by:

$$G_{SS} = G_0\left(1-\frac{\sigma_C}{\sigma_0}\right)^2 \tag{5.2.9}$$

The energy release rate as a function of the normalized blister half width in the 1200 nm thermally grown and PECVD oxide films is shown in Figure 5.2.29, where the intrinsic stress inferred from the interpolated minimum width for buckling was used for σ_0 in Equation 5.2.8 (σ_0 = 1.58 GPa for thermal oxide, (σ_0 = 0.91 GPa for PECVD oxide). If the asymptotic intrinsic stress were used to calculate the G_L or G_{SS} (i.e. $\sigma_0 \approx 0.6$ GPa for the thermal oxide, $\sigma_0 \approx 0.3$ GPa for the PECVD oxide), the energy release rates took on a negative values for normalized blister half widths b/h < 10.3 for the thermal oxide film, and b/h < 15.2 for the PECVD oxide. This demonstrates that the standard theory for buckling

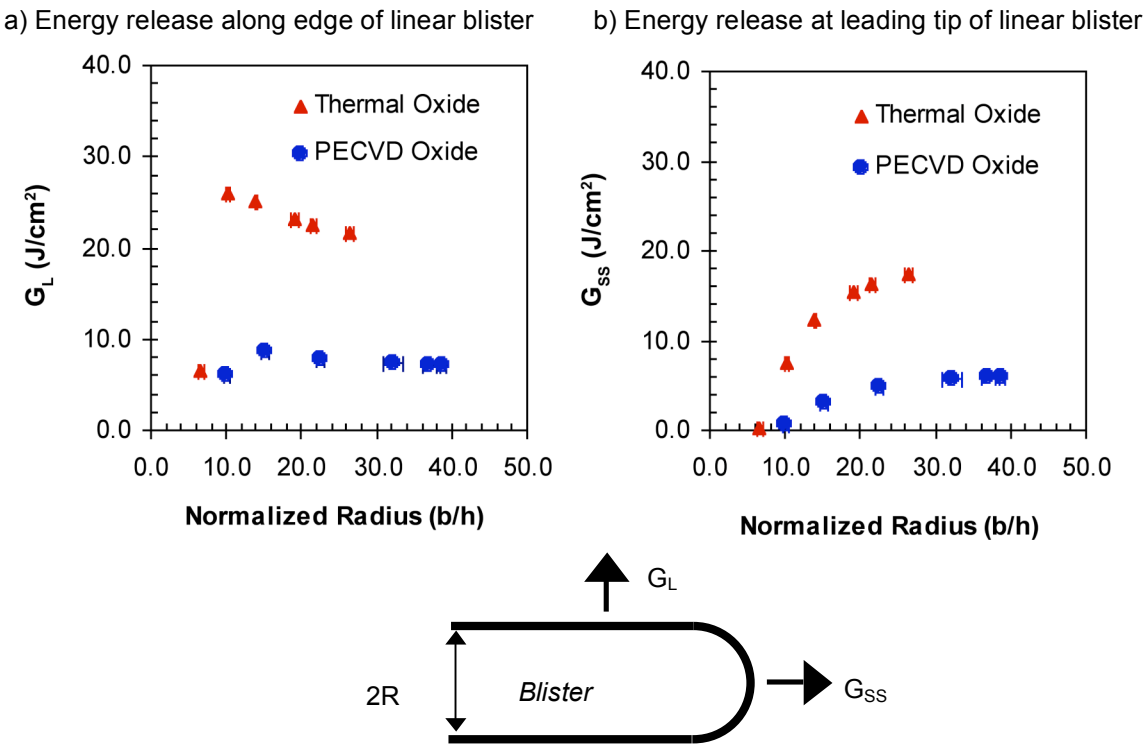

Figure 5.2.29 a) Calculated energy release rate at blister edge as a function of normalized linear blister half width (Equation 5.2.8). b) Calculated energy release rate at blister tip as a function of normalized linear blister half width (Equation 5.2.9).

can provide unphysical results when the fs laser ablation event participates in film buckling, and that care must be taken in interpreting results.

The energy release rate at the blister tip (G_{SS}) for the blister channel with the smallest half width can be used to place an upper bound on the interface fracture toughness for the thermally grown and PECVD oxide films. Provided the observation that the fs laser ablation participates in the blister formation, this bound on the fracture toughness is only valid under fs laser induced buckling at a laser fluence of 0.4 J/cm^2, and does not represent the fracture toughness of the film in the absence of laser irradiation. The energy release rate for the blister channel with the smallest normalized half width is 0.15 J/m^2 and 0.58 J/m^2 for the 1200 nm thermally grown and PECVD oxide films respectively. A lower bound could be placed on the fracture toughness if different laser beam focusing conditions had been pursued which produced a narrower focused beam (thus narrow region of film delamination) which did not yield buckling of the film at a

fixed laser fluence of 0.4 J/cm^2 [150], however no experiments were performed and the topic must be delegated to future work. Furthermore, the adhesion of the oxide film silicon substrate can be obtained through analysis of linear blister channels exhibiting the telephone cord instability [245]. This analysis was not performed because the height of linear blisters exhibiting the telephone cord instability exceeded the limits of the AFM (see Chapter 3.6.3), such that accurate measurement of necessary blister dimensions was not performed. Such analysis should be addressed in future work.

As alluded to earlier, analysis of pump-probe imaging experiments discussed in section 6.2.1 provide further insight into the manner in which the laser ablation event influences film buckling and blister formation. The energy release underlying the production of a shock wave associated with the fs laser ablation event can be determined by analyzing the dimensions of the shock wave as a function of time (see Chapter 6.1.2). This analysis showed that at the same incident laser fluence, the presence of a 1200 nm thermal oxide reduced the energy release relative to Si(100) samples with only native oxide. In other words, the shock wave generated by ablation at the substrate film interface appears to have lost energy upon traversing the thermal oxide film. This energy may be responsible buckling of the film at delamination radii which would not produced buckling under relaxation of the intrinsic film stress alone.

In summary, the dimensions of fs laser induced circular blisters in 300 nm and 1200 nm thermally grown oxide films, and linear blister channels in 1200 nm thermally grown and PECVD oxide films were analyzed according to the mechanics of thin film buckling. The intrinsic film stress was determined in two ways; first from the minimum blister width for buckling inferred from fits to the measured blister height vs. blister width, and second from the individual blister dimensions. The inferred intrinsic compressive film stress from the minimum delamination width for buckling exceeded the measured compressive stress in similar films. The excessive inferred intrinsic compressive stress led to the conclusion that the laser ablation event at the substrate film interface produced

buckling of the film at a smaller delamination widths than would be expected from the naturally occurring compressive stress alone.

The intrinsic compressive stress determined from individual blister dimensions was found to asymptotically decrease as a function of normalized blister half width. For the combined data sets of the circular blisters, the asymptotic value was ~0.6 GPa, while for the linear blister channels the asymptotic intrinsic compressive stress values were ~0.6 GPa and 0.3 GPa for the 1200 nm thermally grown and PECVD oxide films respectively. These asymptotic intrinsic stress values still exceeded the measured and reported values, leading to the suggestion that the shock wave associated fs laser ablation event originating at the substrate/film interface yields additional energy to the delaminated oxide film. Analysis of the ablation shock dynamics in later sections (Chapter 6.1.2) elucidates the role of ablation on film buckling by showing that energy is lost by the shock wave as it traverses the oxide film from its plane of origin at the substrate/film interface.

An upper bound on the interface fracture toughness in the presence of the fs laser irradiation was determined from the dimensions of linear blister channels to be around 0.15 J/m^2 for the 1200 nm thermal oxide, and 0.58 J/cm^2 for the 1200 nm PECVD oxide. Future work will investigate whether the interface fracture toughness can be bracketed with a lower bound by experimentally determining a blister half width for which film buckling does not occur at a laser fluence of 0.4 J/cm^2. Furthermore, analysis of the linear blisters exhibiting the telephone cord instability will provide a measure of the adhesion of the thin oxide film to the silicon substrate under the influence of fs laser irradiation.

5.3 Femtosecond laser ablation morphology of CMSX-4 Ni-based superalloy

The surface morphology resulting from single pulse femtosecond laser ablation of the CMSX-4 Ni-based superalloy was study over a range of incident laser fluences using optical and atomic force microscopy (Nomarski OM and AFM). As discussed in Chapter 4.3, two regimes of ablation were observed to result from single-pulse fs laser ablation. The transition between these regimes

was marked by an increase in the depth of ablation craters as a function of incident laser fluence, with the transition occurring at a laser fluence of 5.3 J/cm^2. The surface morphology of single pulse fs ablation was also observed to transition at a similar laser fluence with the emergence of a melt-like morphology in the center of an otherwise smooth ablation crater. The emergence of this morphology may be related to a change in the mechanism for material removal between the two ablation regimes [132]. Characterization of the ablation morphology suggests that for optimal fs laser machining, laser fluences near the ablation threshold should be used to provide for greater feature quality and reproducibility. The results of the single pulse fs laser ablation morphology of the CMSX-4 superalloy is presented in the following section.

5.3.1 Single pulse fs laser ablation morphology on the CMSX-4 superalloy.

Single pulse fs laser ablation studies were performed with the experimental technique presented in Chapter 3.3. Briefly, single pulse ablation features were generated over a wide range of laser fluences (0.49 J/cm^2 – 62.8 J/cm^2) exceeding the ablation threshold for CMSX-4 superalloy (measurements of the ablation threshold range between 0.3 ± 0.03 J/cm^2 [116], 0.332 ± 0.014 J/cm^2 [115], and 0.38 ± 0.2 J/cm^2 (see Chapter 4.3.1). The ablation morphology was characterized by Nomarski OM and AFM, revealing the presence of two distinct ablation morphologies as a function of the incident laser fluence. The observation of two fs laser ablation regimes is discussed in detail elsewhere [116], and results consistent with that work is presented here. It must be emphasized that qualitative observation of the fs laser ablation morphology is highly subjective, and therefore little can be said of the ablation mechanisms simply by looking at images (SEM or OM) of ablation features. Connection between qualitative ablation features and ablation mechanisms should only be made when correlated with appropriate quantitative observations, such as the study of ablation crater depth as a function of incident laser fluence presented in Chapter 4.3.2.

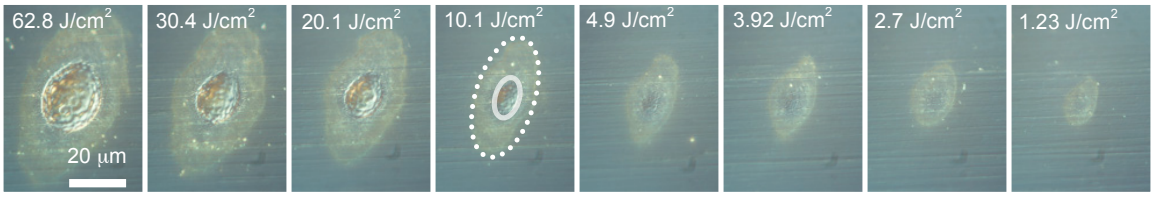

Figure 5.3.1 Nomarski optical microscope images of single pulse fs laser induced ablation features on the Ni-based superalloy CMSX-4. The laser fluence used to produce each feature is shown at the top of the image, and the scale bar in the left-most image (62.8 J/cm^2) applies to all images. In the image corresponding to a laser fluence of 10.1 J/cm^2, two distinct ablation morphologies are indicated. Inside the solid ellipse is the high fluence ablation morphology, consistent with material that has re-solidified from a molten state. Between the solid ellipse and the dotted ellipse is the low fluence ablation morphology, does not appear to have undergone significant melting.

As shown in the Nomarski OM images of Figure 5.3.1, for laser fluences less than or equal to 4.9 J/cm^2 the damage morphology qualitatively consists of a crater with approximately uniform surface roughness. In this low fluence regime (~0.3 J/cm^2 ≤ peak laser fluence ≤ 4.9 J/cm^2), the ablation morphology was also found to be quantitatively repeatable, with consistent surface roughness and ablation depths (as demonstrated by the small error bars (standard deviation) on measurements of the feature depth in Figure 4.3.2 of Chapter 4.3.2). As shown in Figure 5.3.1, in the high fluence regime (peak laser fluence ≥ 10.1 J/cm^2), a damage morphology emerged at the center of the ablation feature which suggested a more violent explosion of material. The high fluence region appears smooth and highly reflective in the Nomarski OM images, while the low fluence regime appears rougher and less reflective than the surrounding, un-ablated surface. A distinction should be made between the melt-like morphology and the onset of an explosive appearance to the ablation crater. As discussed in Chapter 4.3.2, the threshold for observation of the melt-like morphology was determined to be 2.35 ± 0.3 J/cm^2, much lower than the fluence associated with the explosive increase in ablation crater depth as a function of incident laser fluence (~ 6.3 J/cm^2). We conclude that the same physical mechanisms are not responsible for

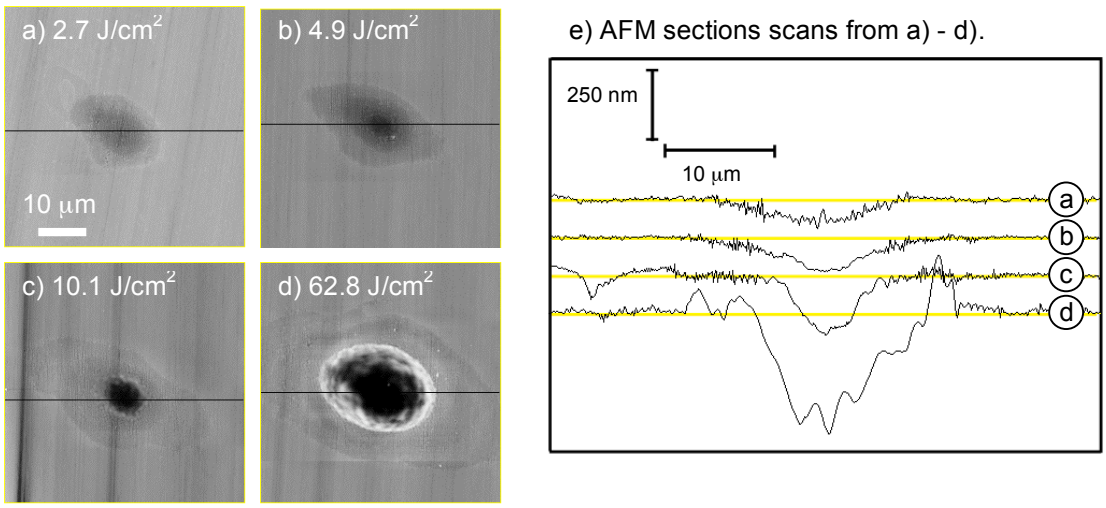

Figure 5.3.2. AFM of single pulse fs laser ablation of the Ni-based superalloy CMSX-4 at normal laser incidence with incident laser fluence: a) 2.7 J/cm^2 b) 4.9 J/cm^2 c) 10.1 J/cm^2 and d) 62.8 J/cm^2. e) Cross sections taken from AFM images a) – d) as indicated.

both the melt-like morphology, and the explosive increase in ablation crater depth.

Characterization of the damage morphology via AFM (Figure 5.3.2 c) and d)) showed that the high fluence morphology was smooth on the sub-micrometer length scale consistent with solidification from a molten state. In the low fluence regime (Figure 5.3.2 a) and b)), sub-micrometer surface roughness was present throughout the entire ablation crater, which appeared to be related to the initial roughness of the polished surface (i.e. polishing lines continued through the ablation region). On the micrometer to 10's of micrometer length scale however, the high fluence morphology was considerable rougher than features produced in the low fluence regime. Furthermore, the high fluence morphology was found to be highly variable both qualitatively and quantitatively with variations in crater morphology and depth removed per pulse at the same laser fluence (see Figure 4.3.2 in section 4.3.2). Similar transitions in the qualitative nature of fs laser ablation morphology have been observed for other materials, including Al [136], Au, Cu, and Ag [262].

As discussed in the Background Chapter (see Chapter 2.2.3), the distinct change in the ablation morphology in the high laser fluence regime may be related to transition from an ablation mechanism dominated by the spallation of

material to one in which heterogeneous boiling becomes important [41, 168]. It has been proposed that the low fluence regime, homogeneous nucleation of voids leads to the ejection or spallation of a liquid like layer from the surface of the material [34, 35, 37, 38]. At higher laser fluences, in-situ observation of fs laser ablation of metals with pump-probe techniques the ablation event is characterized by two phases of material removal [41]. The first phase proceeds as described above, homogeneous nucleation of voids at a depth within the material results in the ejection of a liquid like layer from the surface (within the first 30 ns) [34, 35, 41]. The second phase of material removal is associated with heterogeneous (or possibly homogeneous) boiling of the hot material remaining on the surface (begins at around 40 ns) [41]. Why these two ablation mechanisms result in different surface morphologies is not yet understood, and should be addressed in future work.

In summary, the single pulse fs laser ablation morphology produced on the Ni-based superalloy CMSX-4 was studied over a range of incident laser fluences (0.49 J/cm^2 – 62.8 J/cm^2) above the ablation threshold. Two distinct morphologies were observed as a function of laser fluence. For laser fluences less than or equal to 4.9 J/cm^2, an ablation crater with sub-micrometer roughness was produced which was highly repeatable from shot to shot. For laser fluences greater than or equal to 10.1 J/cm^2, an ablation morphology was produced with considerable roughness on the micrometer scale with greater variability from shot to shot which was correlated with a sudden increase in the ablated crater depth as a function of laser fluence. A melt-like morphology was observed in OM images of ablation features for laser fluences greater than 2.35 ± 0.3 J/cm^2 which was not correlated with the onset the “explosive” morphology for laser fluences greater than or equal to 10.1 J/cm^2. For fs laser micromachining applications where fine control over features is desired, laser fluences in the low fluence regime should be used due to the repeatability of ablation morphologies observed shot to shot, and due to the minimal presence of re-solidified molten materials [20, 22, 113, 134, 135, 262].

Chapter 6

Femtosecond laser ablation dynamics

6.1 Dynamics of fs laser ablation of Si(100) with native oxide and thermally grown oxide films.

The dynamics of single pulse fs laser ablation were studied using the technique of fs laser based pump-probe microscopy [3, 34, 35, 41, 65, 72, 118]. The experimental details of the pump-probe microscopy technique are presented in Chapter 3.3 with a discussion of previous studies is presented in Chapter 2.3. Images of the fs laser ablation event with sub-picosecond exposure times were captured by using the fs laser pulse as the flash of a camera. The ablation event was viewed from the front of sample, similar to traditional reflection optical microscopy, and from the side of the sample, in a mode similar to shadowgraphy. For front-view imaging, single pulse fs laser ablation of Si(100) samples with thermally grown oxide films ranging in thickness from 20 nm – 1200 nm was studied. For side-view imaging, samples also included Si(100) with native oxide, as well as Si(100) with thermally grown oxide films.

The ablation dynamics were observed to depend qualitatively and quantitatively on the thickness of the oxide film. The velocity of the ablated material was determined as a function of film thickness and laser fluence. Furthermore, by comparing the side-view and front-view observations of the ablation dynamics at a common laser fluence, the optical properties of the material during the ablation event were ascertained. Time-resolved side-view images showed the presence of the shock wave associated with the ablation event propagating in the air in front of the sample [41, 65, 72]. Analysis of the dynamics of the air shock [169] demonstrated that more energy was lost by the

shock upon traversing a thicker oxide film, clarifying the role of ablation on blister formation discussed in Chapter 6.2.4.

The technique of dual-pulse laser induced breakdown spectroscopy (DP-LIBS) in the orthogonal beam geometry [192-196, 199] was used to further probe the dynamics of ablation. As discussed in detail in Chapter 2.3.2, LIBS is a spectroscopy technique that utilizes the optical emission accompanying laser induced breakdown to determine the elemental constituents of a material. A fundamental feature of LIBS analysis is ablation or removal of material from a sample surface, which may destroy the value or functionality of a material or device. DP- LIBS of silicon was performed to explore the limits of minimum damage to a material surface associated with the LIBS technique. This experiment was performed as a precursor to LIBS studies on the CMSX-4 superalloy (presented in Chapter 6.2.2), where the technique was explored as possible means for minimally invasive surface characterization of this material of choice for many jet and power turbines [54, 55]. The results of these investigations of fs laser ablation dynamics of Si(100) with native and thermally grown oxide films will be presented in the following sections.

6.1.1 Front view imaging of fs laser ablation of Si(100) with thermally grown oxide films

Pump-probe front-view microscopy of fs laser ablation at a laser fluence of 1.3 J/cm^2 was performed on Si(100) samples with 20 nm, 54 nm, 147 nm, 300 nm, and 1200 nm thermally grown oxide films. Images of the ablation event (see Figure 5.1.1) showed the presence of an interference phenomenon known as Newton's rings, which have been observed under front-view pump-probe imaging of fs laser ablation of several materials which possessed only native oxide on the surface [34, 35]. The presence of the Newton's rings has been attributed to a near threshold fs laser ablation phenomenon in which a thin layer of molten material is ejected from the sample surface [34-38]. This thin molten layer of material is well defined, and was proposed to have a thickness on the order of nanometers [34, 35]. The Newton's ring phenomena results when probe light

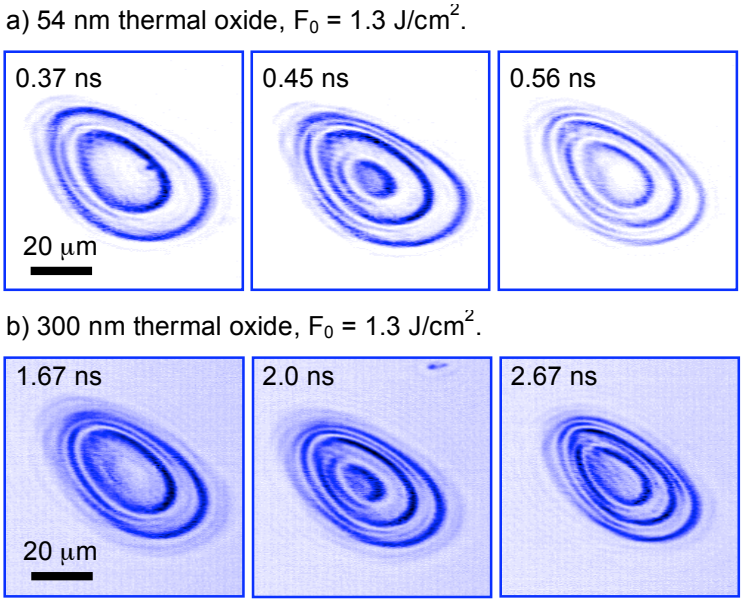

Figure 6.1.1 Time resolved front-view images of single pulse fs laser ablation at a laser fluence of 1.3 J/cm^2. The error in the time stamp is ± 0.05 ns, and the scale bar in the left-most images applies to all images within the set. Images are shown for Si(100) with a) 54 nm thermal oxide and b) 300 nm thermal oxide.

reflecting from the surface of ejected molten layer interferes with light reflected from the underlying molten pool of material remaining on the sample surface.

The Newton's rings are proposed to result from a similar ablation mechanism in the experiments discussed here. The schematic in Figure 6.1.2 presents the model for the ablation event that underlies the analysis of the Newton's rings presented in the following. The incident laser pulse traverses the oxide where slight modification to the oxide film may occur if the laser fluence exceeds the proposed modification threshold of the oxide film (see Chapter 5.1.2 and 5.2.2). The bulk of the laser energy is absorbed by the substrate at the substrate/film interface where ablation of substrate material proceeds. A thin molten layer of material is then ejected upward against the overlying oxide film, which is in turn propelled upward due to the momentum transferred from the molten layer and the relaxation of the intrinsic compressive stress in the film (see Chapter 5.2.2 for more details). In this fashion, the Newton's rings result from interference of probe light reflected from the molten silicon layer attached to the bottom of the oxide film, and probe light reflected from the molten pool of silicon remaining on the substrate. The fringe contrast of the Newton's rings we observe supports a model

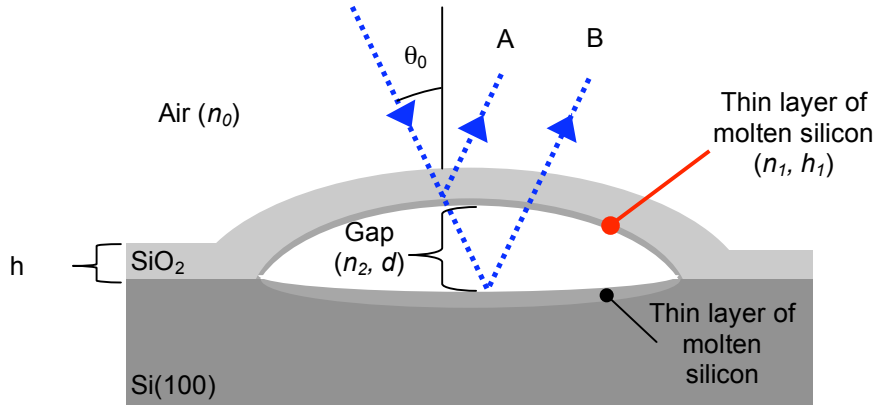

Figure 6.1.2 Schematic showing model for single pulse fs laser ablation of Si(100) with a thin thermally grown oxide film. Ablation event proceeds at the substrate/film interface, where a thin layer of molten silicon is launched upward into the thermal oxide film. Coupled with the relaxation of compressive stress in the film, the momentum transferred from the thin molten silicon layer forces the oxide film upward. The Newton's rings result from interference of probe light reflected from the top surface of the ejected liquid silicon layer (reflection A) and probe light reflected from the liquid silicon remaining on the substrate surface (reflection B).

in which a relatively highly reflecting molten layer of silicon is present on the bottom surface of the oxide film. In other words, the oxide film is not expected to have a reflectivity sufficient to produce the fringe contrast. As the film continues to propagate away from the substrate over time, more Newton's rings emerge within the ablation feature as the separation between the molten silicon layer and the underlying molten substrate increases. Recall that the pump-pulse initiating the ablation event has a Gaussian fluence profile, such that the material in the center of the ablation feature received more energy and therefore ablates the fastest.

The Newton's rings within the ablation features were counted as a function of the time delay of image collection. The time delay at which interference minima (or equivalently a new set of Newton's rings) were observed at the center of the feature is presented in Figure 6.1.3 for each of the thermal oxide films thicknesses at a pump-laser fluence of 1.3 J/cm^2. The linear fits applied to the data in Figure 6.1.3 (note that it is a semi-log plot) demonstrate the propagation of the films away from the substrate was highly linear for all oxide film thicknesses. Furthermore, the propagation rate decreases as the oxide thickness increases (provided that the interference phenomenon is not fundamentally

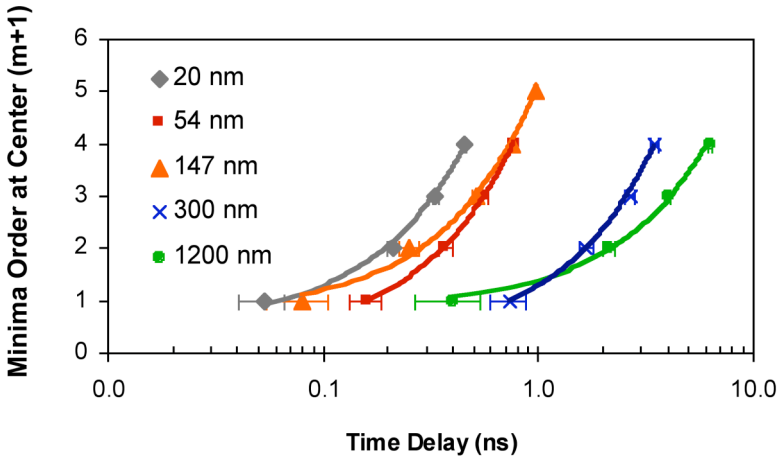

Figure 6.1.3 Minima order at center of ablation feature as a function of time delay between pump and probe pulse at the sample surface. The minima order + 1 corresponds to the number of Newton's rings exhibited by an ablation feature, such that the plot shows the time at which consecutive Newton's rings emerge for a particular feature. Linear fits to the data indicate that the material expands with a nearly constant velocity for all oxide film thicknesses.

dependent on the thickness of the oxide film, as shown in Figure 6.1.2 and presented theoretically in Appendix 2).

In order to determine the ablated material velocity of the material from the time-resolved front-view images, it was necessary to connect a physical material height to the particular number of Newton's rings or fringes exhibited by an ablation feature at a particular time. Appendix 2 presents the details of the derivation of an expression for the gap width d (see Figure 6.1.2) as a function of the optical properties of the ablating materials.

The expression is dependent on the following variables: the angle of observation θ_0, the wavelength of the probe light λ_0, the real refractive index of the ambient atmosphere n_0, the thickness and real refractive index of the ablated silicon layer on the bottom of the expanding glass film h_1 and n_1 respectively, the width and real refractive index of the gap between the bottom of the ablated silicon layer and the underlying substrate d and n_2 respectively, and the number of accumulated interference minima $m(t)$, which was assumed to be the only time dependent variable. For our purposes absorption of radiation by the oxide film or by the liquid silicon was not considered so that only real refractive indices of these materials were used. Known quantities include the refractive index of

ambient atmosphere, n_0 = 1, the angle observation, θ = 49 ± 1°, and the wavelength of the probe light, λ_0 = 388 nm. When destructive interference occurs between reflected rays A and B in the center of the ablation feature, the gap width *d* is given by the following expression:

$$d = \frac{\frac{\lambda_0}{4}(2m+1) - \frac{h_1}{\sqrt{n_1^2 - n_0^2 \sin^2\theta_0}}\left(n_1^2 - n_0^2 \sin^2\theta_0\right)}{\frac{1}{\sqrt{n_2^2 - n_0^2 \sin^2\theta_0}}\left(n_2^2 - n_0^2 \sin^2\theta_0\right)} \qquad (6.1.1)$$

Differentiating Equation (6.1.1) with respect to time *t* yields the velocity of the ablated material:

$$v(t) = \frac{\partial d}{\partial t} = \frac{\frac{\lambda_0}{2}\left(\frac{\partial m(t)}{\partial t}\right)}{\frac{1}{\sqrt{n_2^2 - n_0^2 \sin^2\theta_0}}\left(n_2^2 - n_0^2 \sin^2\theta_0\right)} \qquad (6.1.2)$$

where again we have assumed that the only time dependent variable on the ns time scale is the number of minima exhibited by the ablation feature, *m(t)*. The velocity of the ablated material can be calculated provided that the real refractive index of the gap material n_2 is known or can be determined. To make connection with the actual material height as a function of time (Equation (6.1.1)) it was necessary to determine the thickness h_1 and real refractive index n_1 of the ablated silicon layer on the bottom surface of the expanding glass film. Two related calibration techniques were used to determine the variables of Equations (6.1.1) and (6.1.2) above to connect the Newton's rings phenomenon to a measurable material height and ablated material velocity. The first technique, called the *blister calibration*, will be discussed here, while the second technique, called the *dynamic calibration*, will be discussed in Chapter 6.1.3 following the results of side-view imaging experiments presented in Chapter 6.1.2.

As the name implies, the blister calibration made use of the ablation morphology discussed in Chapter 5.2.2, in which the oxide film is delaminated upward from the underlying silicon substrate but remains intact with the surrounding film, producing a void or blister between the film and the substrate

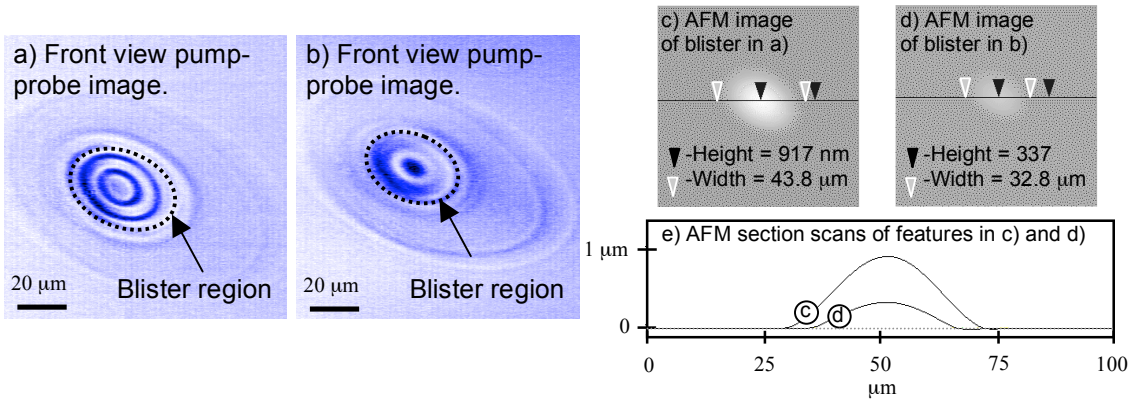

Figure 6.1.4 a)-b) Front view images of blisters in produced in 1200 nm thermal oxide on Si(100) at normal laser incidence. The images were collected at an effective time delay = ∞ following exposure to the pump laser pulse. Both images have been inverted and corrected for off normal imaging. Given that the images have been inverted, the image in d) shows 3 full Newton's rings, while the image in e) shows 1 ring. The blistered or buckled region of the film is indicated. Features in the image outside the buckle region are laser induced modifications to the film/substrate interface (such as amorphization of the silicon substrate) which do not result in buckling. c)-d) Atomic force microscopy (AFM) of a blisters produced in 1200 nm thermal oxide on Si(100) used for the blister calibration of front view imaging. The total width of each image is 100 μm. e) AFM cross sections of blister features in a) and b).

[74]. Front-view pump-probe images were taken of blister features produced at normal laser incidence in a 1200 nm thermally grown oxide film on a Si(100) substrate. Images were collected of the blisters at an effectively infinite time delay after the material had reached steady state conditions. The number of interference minima exhibited by the blisters was counted from the images, and these same blister features were then measured ex-situ via atomic force microscopy (AFM) such that the height of the blister as a function of the number of Newton's rings could be determined. Seven such blister features were produced, with the number of interference minima (or total Newton's rings) ranging from 1.25 ± 0.25 to 3.75 ± 0.25 (with fractional amounts indicating the state of interference at the center of the feature was between a maximum and a minimum). The height of these blisters measured via AFM ranged from 283 nm to 968 nm respectively. Figure 6.1.4 presents examples of front-view images of blister features and associated AFM images and cross sections of features used for the blister calibration.

The blister calibration proceeded by assuming that the blister height measured via AFM was approximately equal to the gap width *d*. This assumption

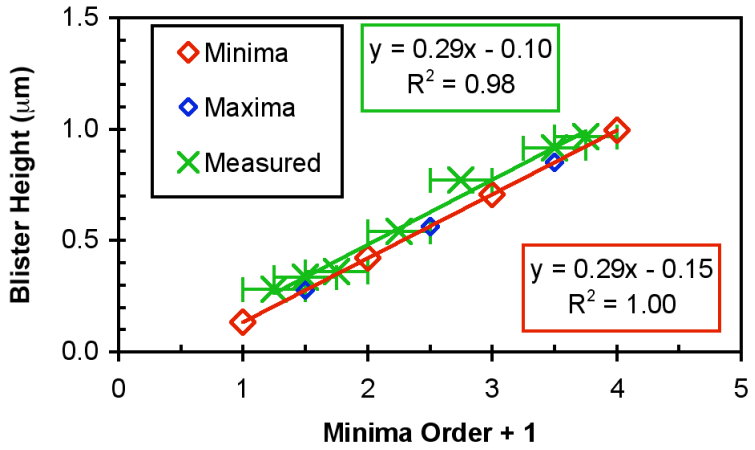

Figure 6.1.5 Results of blister calibration of Equation (6.1.1) for the material height as a function of the number of Newton's rings or minima present in the image a particular ablation feature. A series of blisters were produced on a sample with 1200 nm thermal oxide on Si(100). Pump probe front-view images of these blisters were collected long after the ablation event had ceased, and the number of Newton's rings or minima exhibited by each blister was counted. The maximum height of these same blisters was then measured via AFM. The thickness of the ablation silicon layer on the bottom surface of the delaminated oxide film was then adjusted in expression for the gap height (Equation (6.1.1)) to produce the best match to the measured data, yielding a thickness of $h_1 = 1$ nm.

is valid if we assume negligible volumetric expansion or contraction of the oxide film. The optimal values for the real refractive index, n_1 and thickness, h_1 of the ablated silicon layer on the bottom of the delaminated oxide film, and the real refractive index of the gap material were then determined by forcing Equation (6.1.1) for the gap height as a function of the minima order (or number of Newton's rings) to match the measured blister height as a function of the minima order. As the pump-probe images were collected at an infinite time delay under steady state material conditions, the refractive index of the gap material n_2 was assumed to be that of air or vacuum, such that $n_2 = 1$. Furthermore, the refractive index of the ablated silicon layer on the bottom surface of the buckled oxide film was assumed to be $n_1 = 6.062$, the refractive index of crystalline silicon at a wavelength of $\lambda_0 = 388$ nm. With values for all other variables known or assumed, the thickness of the ablated silicon layer was the only fitting variable, for which a thickness of $h_1 = 1$ nm was found to provide the best match between the measured and inferred blister height as a function of the number of Newton's rings.

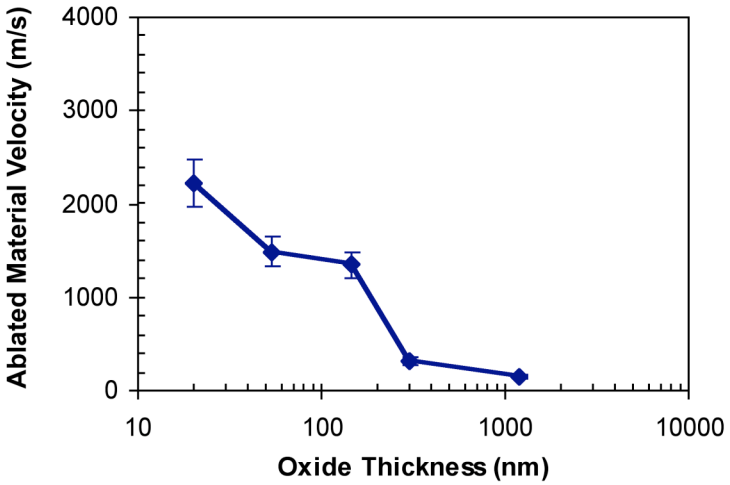

Figure 6.1.6 Ablated material velocity as a function of thermally grown oxide thickness on Si(100) substrates. Velocity determined from blister calibration of Newton's rings interference phenomenon. Laser fluence for all thicknesses was 1.3 J/cm^2.

The results of the blister calibration are shown in Figure 6.1.5. The slope of the theoretical and measured blisters heights matches nicely, however the absolute blister height is under predicted by Equation (6.1.1) by ~ 50 nm relative to the measured results. This discrepancy is not fully understood, and is not accounted for by the thinning of the glass film that would be expected from the relaxation of compressive stress alone. For typical blisters in 1200 nm thermal oxide, the increase in film length upon delamanation to the buckled state is on the order of 10's of nm for delamination widths on the order of 20 μm. Assuming a Poisson ratio of 0.3 [243], this change in length roughly corresponds to a change in film thickness of less than 1 nm (assuming a linear strip of delamination as opposed to a circular disk). Recall from Chapter 5.1.2 that a modification mechanism was proposed for the native oxide film on silicon to explain the observed ring of ablation feature [73]. This modification may be related to the densification of glass observed for waveguide writing in bulk glasses [78, 79, 237]. Investigation of a fs laser induced modification and densification of an oxide film on a crystalline silicon substrate will be the topic of future work.

Applying the blister height vs. minima order obtained from the blister calibration (Figure 6.1.5) to the minima order vs. delay time obtained from the

time-resolved pump-probe images of ablation (Figure 6.1.3) yields the inferred velocity of the ablated material as a function of thermal oxide film thickness at a laser fluence of 1.3 J/cm^2 (Figure 6.1.6). The ablated material velocity was found to decrease with increasing oxide film thickness, with the 20 nm thermal oxide film ablating at a speed of 2220 ± 240 m/s and the 1200 nm thermal oxide film ablating at a speed of 140 ± 21 m/s. It should be noted that the ablation event in all cases was produced with an *incident* peak laser fluence of 1.3 J/cm^2, however the reflectivity changes and ablation threshold variation with oxide film thickness were not used to normalize the velocity measurements (see Chapter 4.2.1). The reflectivity of the silicon substrate at a wavelength of 780 nm as a function of the oxide film thickness is presented in Figure A2.1. There is an increase in the Fresnel intensity reflection coefficient from R = 0.08 for Si(100) with a 147 nm thermally grown oxide film to R = 0.28 for Si(100) with 300 nm thermally grown oxide film. As a result, the ablation threshold increases for the 300 nm film relative to the 147 nm thermal oxide film (see Figure 4.2.2). The increase the ablation threshold between samples with 147 nm and 300 nm thermal oxide may explain the sudden drop in ablated material velocity measured between these two thicknesses (i.e. a higher ablation threshold at a fixed incident laser fluence results in a slower ablation velocity).

While the blister calibration performed here is applicable for observations made at infinity once the system has reached a steady state, it may not apply to real time observation made during the ablation event (i.e. during the first several nanoseconds when the pump-probe front view images were captured). Specifically, air or vacuum was assumed to fill the gap between the ablated silicon layer on the bottom surface of the expanding oxide film and the underlying silicon substrate. It is likely, however, that during the ablation event the gap is filled with other by-products of the ablation event such as energetic plasma of electrons and ions, and droplets of molten material [34, 35]. In order to determine the optical properties of the gap material during the ablation event, the ablated material velocities inferred from front-view images were calibrated against ablated material velocities measured directly from side-view images [77]. The

results of this so-called *dynamic calibration* are presented at the conclusion of the following section following a discussion of side-view imaging of fs laser ablation.

6.1.2 Side-view shadowgraphic imaging of fs laser ablation of Si(100) with thermally grown oxide films.

Pump-probe side-view shadowgraphic microscopy [41, 65, 71] of fs laser ablation Si(100) with thermally grown oxide films of thickness 20 nm, 54 nm, 147 nm, 300 nm, and 1200 nm, and one Si(100) sample with only the native oxide film (1.5 – 3 nm). The experimental details of this imaging technique are provided in Chapter 3.7.1. Images were collected for normal incident laser ablation produced at incident laser pulse fluences of 1.3 J/cm^2 and 2.6 J/cm^2, over the time delay range from 0 to 10.36 ns following the onset of ablation. An example of a typical image is shown in Figure 6.1.7, where several image features are indicated. The pump laser pulse is incident from the right in all images, while the sample surface is on the left, such that the ablation event proceeds from the sample surface to right into the air in front of the sample. In discussing the images, the propagation of the ablation event is discussed with respect to the sample surface, such that the “vertical shock front” (or “vertical material front”) propagates perpendicular to the sample surface. As with front-view images, each image is obtained at a new location on the sample surface such that a virgin surface is encountered for each image and delay time between the pump and probe pulse.

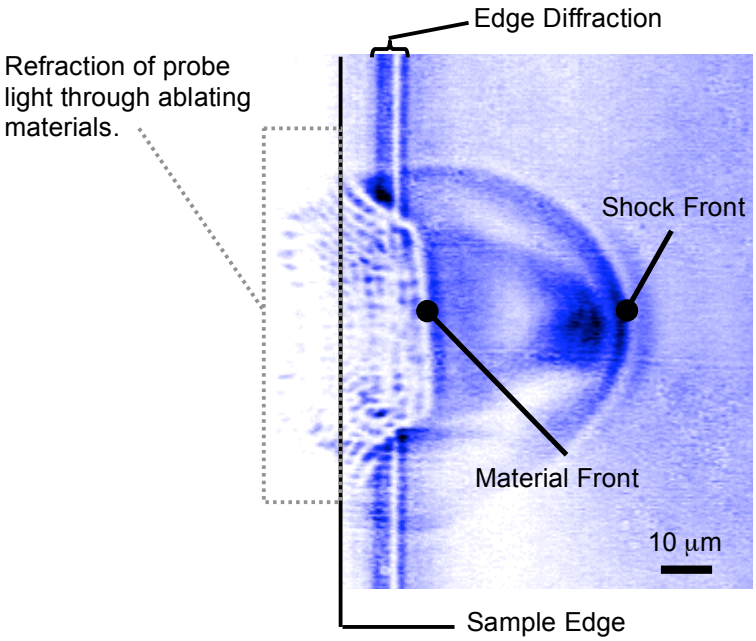

Figure 6.1.7 Side-view image of fs laser ablation of Si(100) with 147 nm thermal oxide film at a laser fluence of 2.8 J/cm^2, collected 7.01 ns following absorption of the pump pulse at the sample surface. The laser was incident from the right in the image. Image features including the air shock front, material front, sample edge, and edge diffraction are indicated. A refraction feature to the left of the sample edge is also apparent in the image, resulting from the probe pulse passing through the ablation event.

In the sample image of Figure 6.1.7, vertical interference fringes at the left of the image are produced by the edge of the sample, with the sample surface located to the left of the first fringe. Two fronts are associated with the ablation event: a shock front or blast wave traveling in the air resulting from the sudden thermal expansion of the surface [167] is the furthest to the right, while the material front is located between the sample surface and the shock front [65].

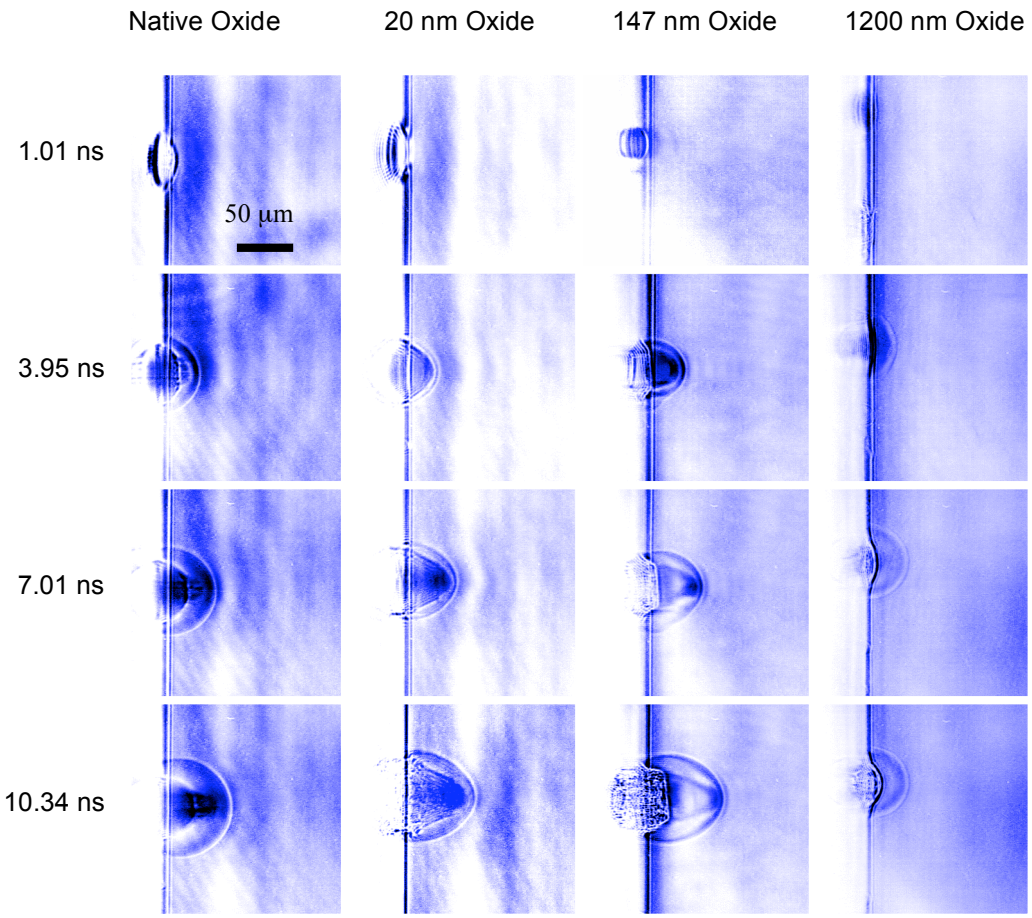

Figure 6.1.8 Pump-probe *side-view* or shadowgraphic images of single fs laser pulse ablation at a laser fluence of 2.6 J/cm^2 on Si(100) with native oxide and thermal oxide thin films of varying thickness. The thickness of the film is indicated at the top, while the time delay at which each row of images was captured is shown at the left of the figure. The scale bar in the top left image applies to all images.

The location of the sample surface was made with respect to the fringe pattern produced due to the diffraction of the probe beam as it passed the edge of the sample. Using the standard Fresnel theory for plane wave diffraction from a semi-infinite plane, the location of the sample edge can be located relative to the first diffraction maximum [263]. Typically, the ablation event was produced 50-200 μm inside the surface (measured ex-situ), such that sample edge was located approximately ~ 2 - 8 μm to the left of the first fringe. It should be noted however that the quantity of interest was the velocity of the ablating materials, such that accurate relative measurements of the shock and material height were more important than absolute measurements of these distances. Furthermore,

the directions of shock and material propagation refer to the sample surface, such that the “vertical” shock travels from the left, to the right in the image of Figure 6.1.7.

Side-view images collected of fs laser ablation at an incident laser fluence of 2.6 J/cm^2 are shown in Figure 6.1.8 for Si(100) with native oxide, and 20 nm, 147 nm, and 1200 nm thermally grown oxide films. These images demonstrate qualitative and quantitative differences as a function of the oxide film thickness. In terms of qualitative differences, it was observed that the nature of the material removal for silicon with a native oxide was different than that of silicon with 20 nm of thermal oxide. At a pump laser fluence of 2.6 J/cm^2, the shock and material fronts are distinctly separated for the sample with only native oxide. However, in the presence of a 20 nm (and 54 nm thermal oxide, not shown) the material front and shock front propagate together for some time, until at around 2 ns when the oxide film appears to shatter and the shock and material fronts become distinct. Similar observations were made for the thicker thermal oxide films, however the separation between the shock and material fronts occurred at much earlier time delays (within the first few hundred ps). This observation is consistent with our assumption that the laser ablation event begins at the substrate film interface, where the ablation shock wave is produced. For the thinner oxide films (20 nm and 54 nm) the shock wave appears capable of dragging the oxide film, perhaps because the oxide has been softened due to the heat associated with the ablation event [61]. For the thicker films, the separation may occur earlier as heat penetration has not softened the film as completely as the thinner films, so that the shock is not able to drag the film with it. Of additional interest is the plateau or mesa nature of the material front for the 147 nm thermal oxide film (see Figure 6.1.7), a phenomenon that at this time is not completely understood.

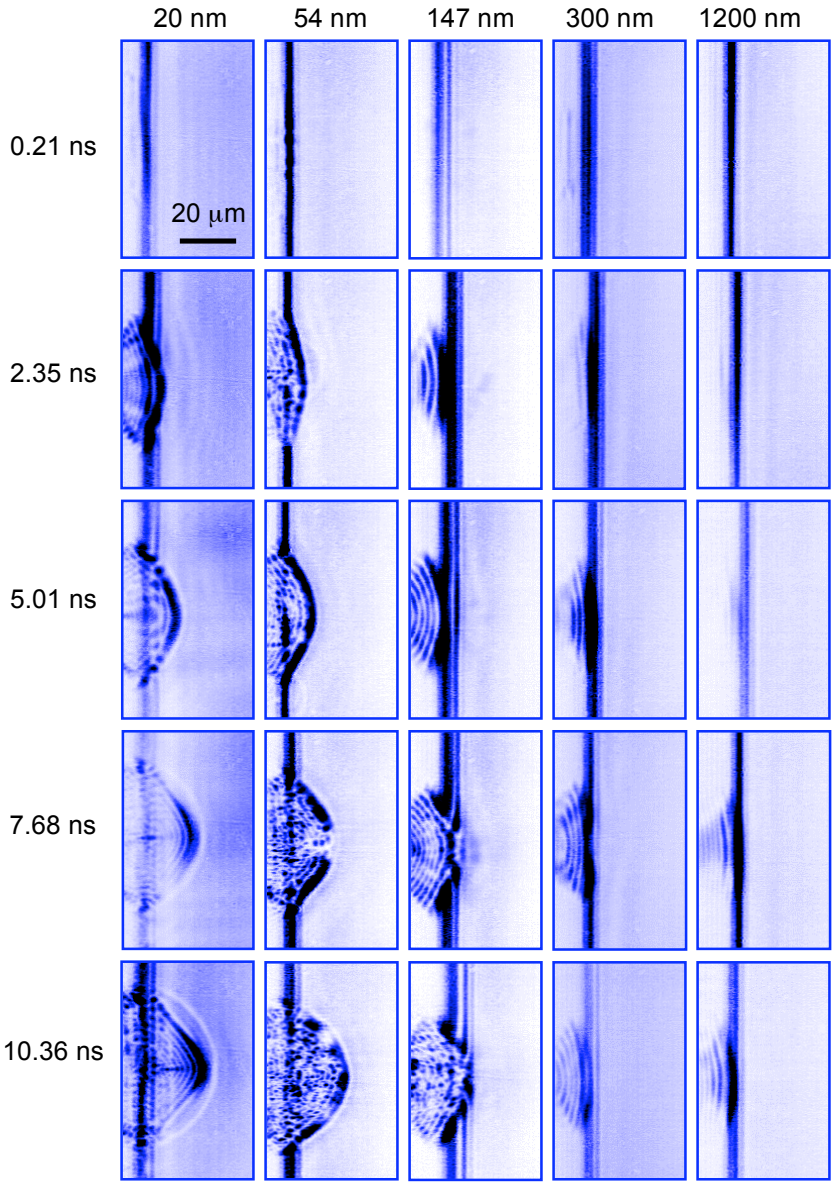

Figure 6.1.9 Pump-probe *side-view* or shadowgraphic images of single fs laser pulse ablation at a laser fluence of 1.3 J/cm^2 on Si(100) with thermal oxide thin films of varying thickness. The thickness of the film is indicated at the top, while the time delay at which each row of images was captured is shown at the left of the figure. The scale bar in the top left image applies to all images.

Side-view images of single pulse fs laser ablation at a laser fluence of 1.3 J/cm^2 of Si(100) with all thermal oxide film thicknesses considered is presented in Figure 6.1.9. Measurements of the material height as a function of time delay at a pump laser fluence of 1.3 J/cm^2 are presented in Figure 6.1.10. In Figure 6.1.11 the material height and shock height are presented for a pump laser fluence of

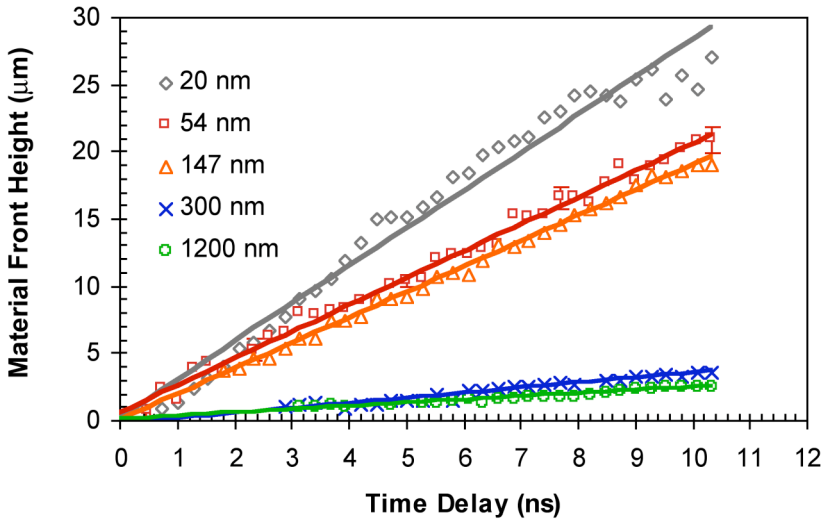

Figure 6.1.10 Measurements of the material front height vs. time delay obtained from side view images for a pump laser fluence of 1.3 J/cm^2. Linear fits of the expanding material fronts are provided in the plot. The error bars on select data points in the 54 nm data set represent the measured standard deviation, and are typical of all data sets. The absolute measurement error is approximately ± 2 μm for all data sets, largely due to limitations in accurately determining the sample edge.

2.6 J/cm^2. The shock height was not measured at a pump laser fluence of 1.3 J/cm^2 as its presence was not obvious or consistent in the side-view images. This may be because the material and shock front moved together (i.e. were connected) for the pump fluence of 1.3 J/cm^2 (as mentioned above), or that the magnitude of the shock was insufficient to produce image contrast due to reflection at the interface between the oxide film and the ambient air [264]. Linear least-squares fits applied to the material front heights yield the velocity of the ablated material, which is presented in Figure 6.1.12 for incident pump-pulse laser fluences of 1.3 J/cm^2 and 2.6 J/cm^2. The standard error for the measurement of velocities from side-view images was determined to be ± 200 m/s. For a laser fluence of 1.3 J/cm^2, the ablated material velocity was found to generally decrease with increasing thermal oxide film thickness, with the sample with native oxide exhibiting a slightly smaller ablation velocity (2130 m/s) than the sample with the 20 nm thermal oxide film (2810 m/s). We will address the relative ablation velocity between front- and side-view imaging at a laser fluence of 1.3 J/cm^2 below when the dynamic calibration is discussed. For a laser fluence of 2.6 J/cm^2, the ablated material velocity was found to vary with increasing thermal

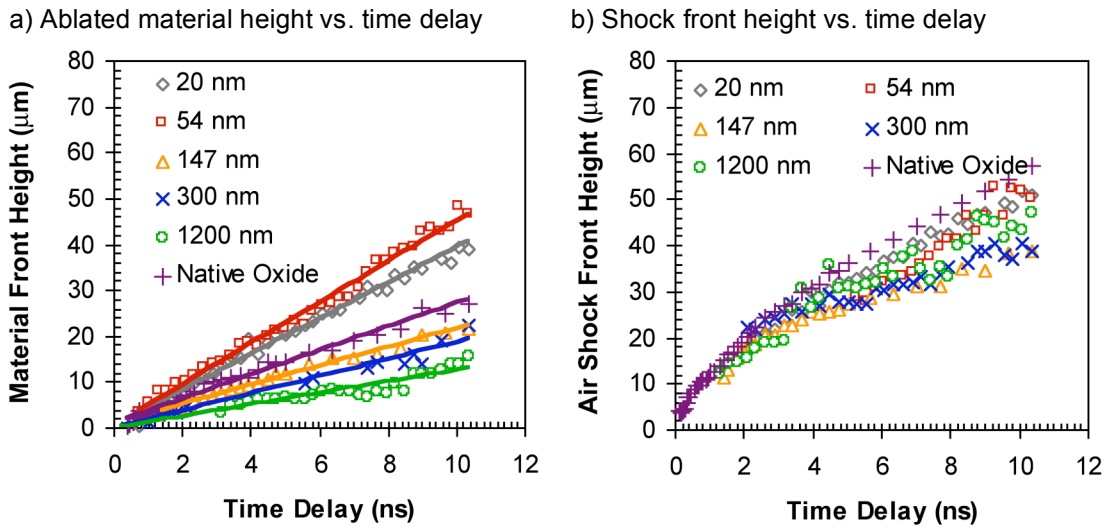

Figure 6.1.11 Measurements from side-view pump-probe images of fs laser ablation of Si (100) with thermally grown oxide films at a laser fluence of 2.6 J/cm^2. a) Ablated material height as a function of delay time. Linear fits to the measurements are provided in the plot, and measurements have been vertically offset to yield a height = 0 at a delay of 0 ns. b) Shock wave height as a function of delay time. Raw measurements are provided with no offset. The absolute measurement error is approximately ± 2 μm for all data sets, largely due to limitations in accurately determining the sample edge.

oxide film thickness, with the ablated material velocity for the sample with native oxide smaller than that measured for samples with 20 nm, and 54 nm of thermal oxide. These velocities ranged from 4460 m/s for the 54 nm thermal oxide to 1260 m/s for the 1200 nm thermal oxide film (with a standard error for side view imaging of ± 200 m/s).

The dynamics of the shock wave induced by the fs laser ablation of silicon with native oxide and thermally grown oxide films were analyzed using Sedov-Taylor blast wave theory [169, 170]. Analysis was performed on ablation shock waves traveling in the air in front of the sample resulting from ablation at an incident laser fluence of 2.6 J/cm^2, the raw data for which is presented in Figure 6.1.1b). Following Sedov's theory [169], the general shock radius as a function of time is given by:

$$r = \lambda \left(\frac{E_o}{\alpha \rho_1} \right)^{1/(2+\nu)} t^{2/(2+\nu)} \qquad (6.1.3)$$

where E_0 is the energy release responsible for the observed shock, ν is the dimensionality of the shock expansion, ρ_1 is the density of the propagating

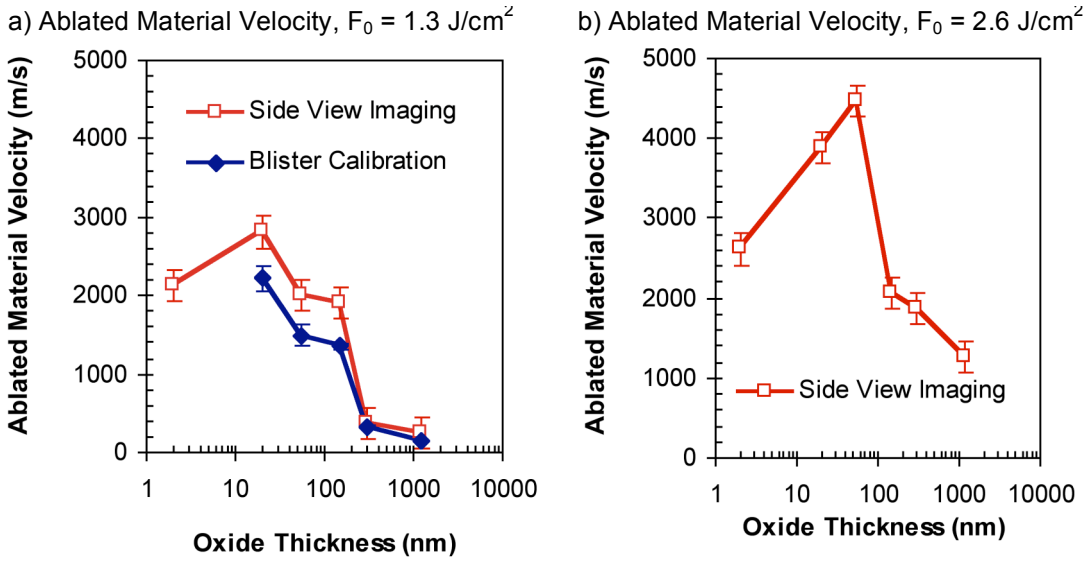

Figure 6.1.12 Ablated material velocity for Si(100) with native oxide and thermal oxide films. a) Ablated material velocity as a function of oxide film thickness at a laser fluence of 1.3 J/cm^2. Velocities directly measured from analysis of time-resolved side-view images are presented along with velocities inferred from time-resolved front view images with the blister calibration. b) Ablated material velocities as a function of oxide film thickness at a laser fluence of 2.6 J/cm^2. Velocities were obtained from analysis of time-resolved side-view images. No front view imaging was performed for this laser fluence.

medium (in this case air), α is an additional proportionality constant dependent on the dimensionality of expansion, λ is a constant (which has been set to 1 for our purposes), and *t* is the delay time. The shock dimensionality can be interpreted in terms of the shape of the energy release which produced the shock wave. For a point release of energy, a spherically expanding shock wave is produced with dimensionality $\nu = 3$. Furthermore, for a line release of energy, a cylindrically expanding shock wave is produced with dimensionality $\nu = 2$. Finally, for a planar release of energy, a linearly expanding shock wave is produced with dimensionality $\nu = 1$. The units of the energy release E_0 are dependent on the shock dimensionality, with $[E_0]$ = energy for $\nu = 3$, with $[E_0]$ = energy/length for $\nu = 2$, and with $[E_0]$ = energy/area (or fluence) for $\nu = 1$.

As can be seen by Equation (6.1.3), the energy release E_0 and the dimensionality of the shock ν can be determined (provided the proportionality constant α is known) by performing a power law fit to the measured shock height as a function of the time delay *t* (presented in Figure 6.1.11b)). Consistent shock

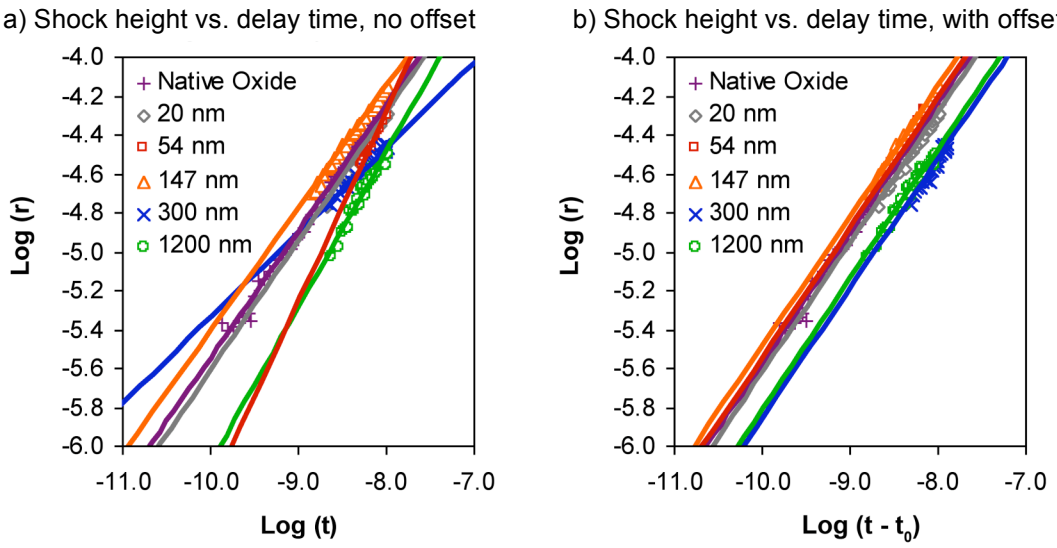

Figure 6.1.13 Effect of applying the time offset t_0 to Equation 6.1.3 to force a common shock expansion dimensionality (ν =1) for all data sets. In the log-log plots presented here, the slope of the linear fits is related to the shock dimensionality. a) Height of shock wave in air from ablation at a laser fluence of 2.6 J/cm^2 as a function of time delay without time offset. b) Height of shock wave in air from ablation at a laser fluence of 2.6 J/cm^2 as a function of time delay time offset. Note that all lines have the same slope.

dimensionality ν was required between data sets in order for appropriate comparisons of the predicted energy release E_0 to be made between different data sets. To this end, a variable time offset t_0 was introduced into Equation (5.1.3) to allow for the dimensionality ν to be fit to values for which predictions of energy release could be made (i.e. ν = 1, 2,or 3), yielding:

$$r = \lambda\left(\frac{E_o}{\alpha\rho_1}\right)^{1/(2+\nu)}\left(t - t_0\right)^{2/(2+\nu)} \qquad (6.1.4)$$

Without this time offset, the dimensionality constants for the vertical shock height ranged from ν = 0.044 – 2.56. Several values were however near ν = 1,

Table 6.1.1: Shock expansion fitting parameters.

Analysis of Vertical Shock Expansion					
Oxide Thickness	Initial Dimensionality	Initial R^2	Assumed Dimensionality	Time Offset (t_0) (sec.)	Final R^2
Native Oxide	1.073	0.9941	1	-1.99×10^{-11}	0.9945
20 nm	1.027	0.9898	1	-4.15×10^{-11}	0.9997
54 nm	0.044	0.9598	1	2.3075×10^{-9}	0.9559
147 nm	1.179	0.9939	1	-2.135×10^{-10}	0.9921
300 nm	2.586	0.9331	1	-2.545×10^{-9}	0.9454
1200 nm	0.509	0.9676	1	8.145×10^{-10}	0.9735

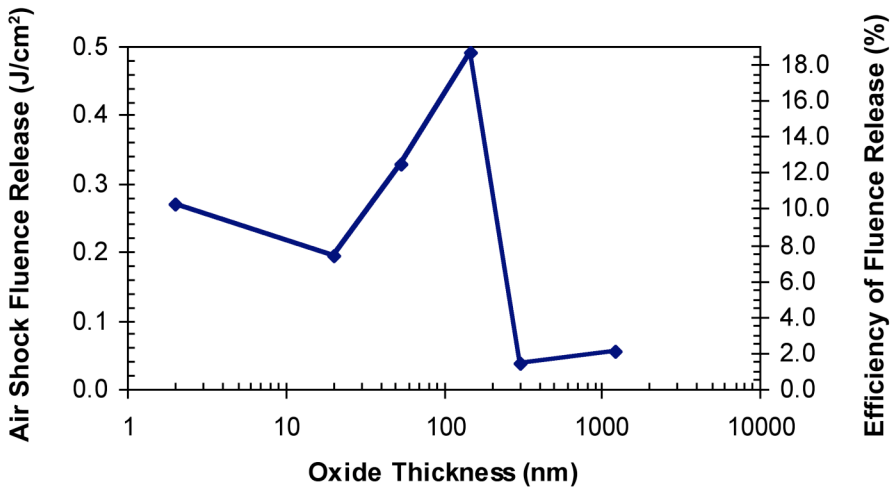

Figure 6.1.14 Calculated fluence release responsible for shock dynamics as a function of oxide film thickness measured from single pulse fs laser ablation of Si(100) with native oxide and thermally grown oxide films at a pump pulse laser fluence of 2.6 J/cm^2. The % yield is indicated on the right axis in terms of the incident pump laser fluence (efficiency = shock fluence release / incident pump laser fluence).

and this dimensionality was obtained for all data sets through application of the time offset t_0 (see Table 6.1.1). Similar pump-probe shadowgraphic imaging studies of fs laser ablation of silicon with native oxide have reported vertical shock expansion with planar dimensionality (ν = 1) [72]. The effect of adding the time offset is demonstrated in the log-log plots of Figure 6.1.13.

Using an expansion dimensionality of ν = 1 for the vertical shock expansion, the energy fluence release responsible for the observed shock dynamics was calculated for single fs laser pulse ablation at a pump laser fluence of 2.6 J/cm^2 (see Figure 6.1.14). In terms of the incident laser fluence 2.6 J/cm^2, the efficiency with which the laser energy is converted into the shock energy is also shown in Figure 6.1.13 (efficiency = laser fluence release, E_0 / incident laser fluence). These results were not normalized with respect to the measured ablation threshold or calculated optical reflectivity as a function of the oxide thickness. Recall from Chapter 4.2.1 that the ablation thresholds for Si(100) with 147 nm and 1200 nm thermal oxide were very similar (see Figure 4.2.2), however the fluence release associated with the ablation shock wave were found to be quite different (see Figure 6.1.13). The efficiency generally varied with oxide film

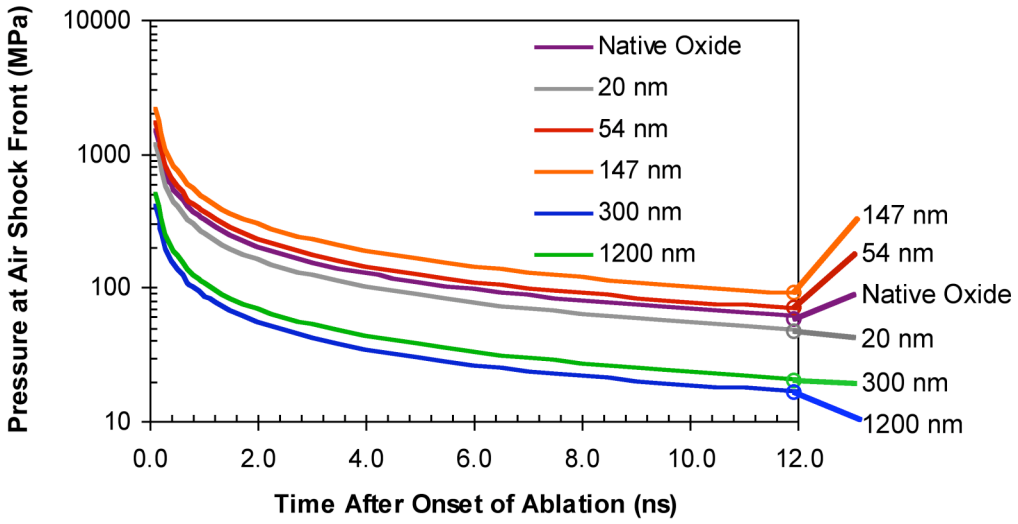

Figure 6.1.15 Calculated pressure at the shock front in air as a function of time following fs laser ablation of Si(100) with thin oxide films at a laser fluence of 2.6 J/cm^2.

thickness, ranging from a minimum of 1.5 % efficiency for the 300 nm thermal oxide film to 18.9 % efficiency for the 147 nm thermal oxide film.

Of significance is the decrease in shock energy release between samples with the native oxide and samples with 300 nm and 1200 nm thermally grown oxide. This decrease in shock energy release may be related to the buckling of 300 nm thermal oxide and 1200 nm thermal and PECVD oxide films discussed in Chapter 5.2.4. Assuming that the trend in energy release is consistent at lower laser fluences, it is proposed that shock wave deposits energy into the oxide film as it passes from the silicon substrate to the film and from the film to the ambient air due to an impedance mismatch at these interfaces [261]. This additional energy may encourage buckling or blistering of the 300 nm thermal oxide and 1200 nm thermal and PECVD oxide films from the Si(100) substrates at smaller delamination widths than would be expected from relaxation of compressive intrinsic film stress alone. A mechanics analysis incorporating the effect of a shockwave on buckling should be considered in future work [146].

Once the energy released was obtained, the pressure at the leading edge of the shock front was calculated as a function of time following the onset of ablation via the following expression (see Figure 6.1.15) [169]:

$$P = \frac{8\rho_1}{(\nu+2)^2(\gamma+1)}\left(\frac{E_o}{\alpha\rho_1}\right)^{2/(2+\nu)}(t-t_0)^{-2\nu/(2+\nu)} \qquad (6.1.5)$$

where γ is the ratio of the specific heat (γ = 1.4). Table 6.1.1 presents the time offsets t_0, and slope of the linear fits (for log-log plots, as in Figure 6.1.13) to the shock expansion in the vertical direction, and the R^2 values corresponding to the power law fits before and after application of the time offset. According to Sedov's theory, the pressure at the shock wave front exceeds 2 GPa for times within the first 10's of picoseconds following fs ablation of Si(100) samples with native oxide, and 20 nm, 54 nm, and 147 nm thermally grown oxide films at a laser fluence of 2.6 J/cm^2.

Returning to the comparison of front- and side-view imaging, the ablated material velocity as a function of oxide film thickness on Si(100) at a laser fluence of 1.3 J/cm^2 is presented in Figure 6.1.12a). The velocity directly obtained from time-resolved side-view images exhibits a similar trend with oxide film thickness as the ablated material velocity inferred from the front-view images using the blister calibration (the blister calibration of the Newton's rings is explained in Chapter 6.1.1). However, the velocity inferred from front-view imaging was typically around 75% of that measured directly from side-view images. This discrepancy may indicate that the blister calibration was only valid for observations made at infinity, once the system had reached a steady state. The following section addresses the *dynamic calibration* of the Newton's rings, in which the ablated material velocity inferred from front-view imaging is made to match with the direct measurements made from side-view images, yielding the properties of the gap material during the ablation event.

6.1.3 Dynamic calibration of fs laser ablated material velocity of Si(100) with thermal oxide films

As described at the end of Chapter 6.1.1, the so called blister calibration was used to connect a physical height to the Newton's rings in front-view images of blister features. The blister calibration was subsequently used to determined the ablated material velocity from the evolution of Newton's rings in front-view

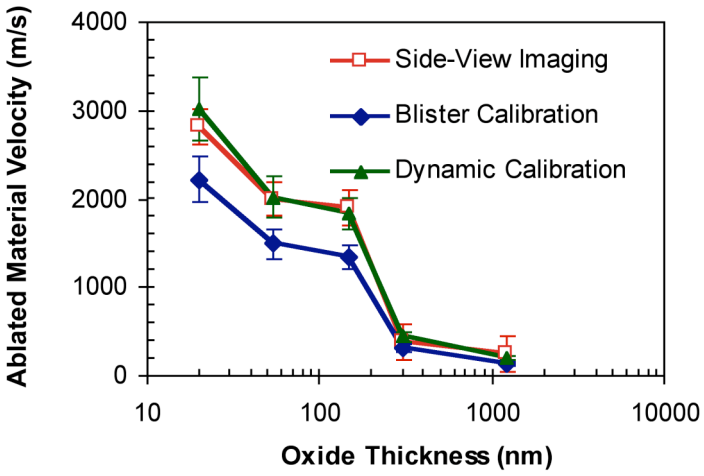

Figure 6.1.16 Ablated material velocity as a function of thermal oxide film thickness on Si(100) at a laser fluence of 1.3 J/cm^2. The velocities directly measured from time-resolved side-view images are presented, along with inferred velocities from front-view images where the blister and dynamic calibrations have been applied to the observed Newton's rings. The results of the dynamic calibration suggest that the gap region between the two interfaces responsible for the Newton's rings is filled with a plasma with a refractive index of 0.9 and an electron density of approximately 10^{21} cm^{-3}.

images of fs laser ablation of Si(100) with thermal oxide at a pump laser fluence of 1.3 J/cm^2. The ablated material velocities determined using the blister calibration were found to be around 75% of those directly measured from time-resolved side-view images at the same pump laser fluence (see Figure 6.1.12a)). It was suggested that the optical properties of the gap material used for the blister calibration, specifically the real refractive index n_2 of the gap, were not appropriate for front-view observations made during the ablation event (i.e. during the first 10.36 ns of ablation). In order to correct the model for the ablated material velocity from front view images, the real refractive index of the gap material, n_2 (see schematic in Figure 6.1.2) was simply adjusted in Equation 6.1.2 so that inferred velocities from front-view images (i.e. during the first 10.36 ns of ablation) matched those directly measured from side-view images.

At a laser fluence of 1.3 J/cm^2, a real refractive index for the gap material of n_2 = 0.9 was found to increase the ablated material velocities inferred from front view images to match those directly measured from side-view images for all oxide film thicknesses. The ablated material velocities from side-view imaging, and from front-view imaging with both the blister and dynamic calibrations in

presented in Figure 6.1.16. Utilizing a real refractive index of n_2 = 0.9 for the gap material during ablation suggests that plasma fills the gap between the molten silicon substrate and the ablated silicon layer on the bottom surface of the expanding glass film during the first several ns of ablation. Following the Drude model, a real refractive index of n_2 = 0.9 corresponds to an electron density of ~ 1.4×10^{21} cm^{-3} [230]. At an electron density of 10^{21} cm^{-3}, the plasma is non-absorbing (i.e. dielectric permittivity, $\varepsilon > 0$) and is thus consistent with a model in which the probe light propagates through the gap material to reflect off the molten substrate.

Other studies in which the Newton's rings have been observed under fs laser irradiation of silicon surfaces have suggested that the gap material must have a refractive index of around 2 in order to produce the measured fringe contrast [34]. Following this, they propose that the gap is approximately half filled with metallic droplets much smaller than the wavelength of light. It should be noted however, that in that work the pump laser fluence of 0.46 J/cm^2 was used to initiate the ablation event, which is less than the fluence required to generate plasma upon fs laser ablation of silicon [15]. In other works employing pump-probe microscopy, higher plasma densities were found (10^{23} cm^{-3} [65]) at a peak laser fluence of 3.0 J/cm^2, which would render the plasma opaque or highly reflective at the probe wavelength of 400 nm. Future work will investigate if at higher fluences the plasma density becomes sufficiently large as to render the gap material opaque, thereby eliminating the presence of the Newton's rings under our model.

In summary, the dynamic calibration of the optical model for the Newton's rings suggests that during ablation at a laser fluence of 1.3 J/cm^2, plasma fills the gap between the two interfaces responsible for the Newton's rings, specifically the liquid silicon layer on the bottom surface of the expanding oxide film an a liquid silicon puddle at the surface of the substrate. At a pump laser fluence of 1.3 J/cm^2 this plasma had a real refractive index of 0.9 and a density of around 10^{21} electrons/cm^3. With a value of n_2 = 0.9 for the refractive index of the gap material, the ablated material velocity predicted from the evolution of the

Newton's rings present in front-view images was found to match the ablated material velocity measured directly from side-view images of the ablation event for all thermal oxide film thicknesses. Future work will investigate the properties of this plasma under a range of pump laser fluences in an effort to further verify the model.

6.1.4 Orthogonal dual pulse LIBS of Si(100) with native oxide

As mentioned in the introductory remarks of this section, dual-pulse laser induced breakdown spectroscopy (DP-LIBS) was investigated as a means for reducing the fs laser induced surface damage resulting from the LIBS technique. The experimental setup for this technique is provided in Figure 3.6.2, where it is shown that the experimental apparatus for the DP-LIBS technique is very similar to that of side-view shadowgraphic imaging, with the difference being that with DP-LIBS the probe pulse is tightly focused to high intensity so that it aggressively ionizes material ablated by the pump pulse. In contrast to earlier studies with DP-LIBS where the focus was simply increasing signal amplitudes [192, 199], we have investigated the threshold for LIBS analysis using the orthogonal, DP-LIBS technique. This work was performed as exploratory study which was later extended to DP-LIBS analysis of the Ni-based superalloy CMSX-4 presented in Chapter 6.2.2.

In order to reduce damage the sample surface (in this case a Si(100) wafer), the intensity of a primary pump laser pulse directed at normal incidence onto a sample surface was decreased until the resulting ablation produced no optical emission above the background in the measured LIBS spectrum at the characteristic wavelength of 390.874 nm (corresponding to singly ionized Si [228]). Although an optically emitting plasma was not observed, ablation and therefore material removal was still produced on the sample surface. A second, high intensity probe laser pulse was then introduced parallel to the sample surface some fixed distance above the sample (25-50 μm), and with a delay (0-23.45 ns) with respect to the primary pulse. This second pulse encountered the ejected material resulting from the ablation of the primary pump pulse,

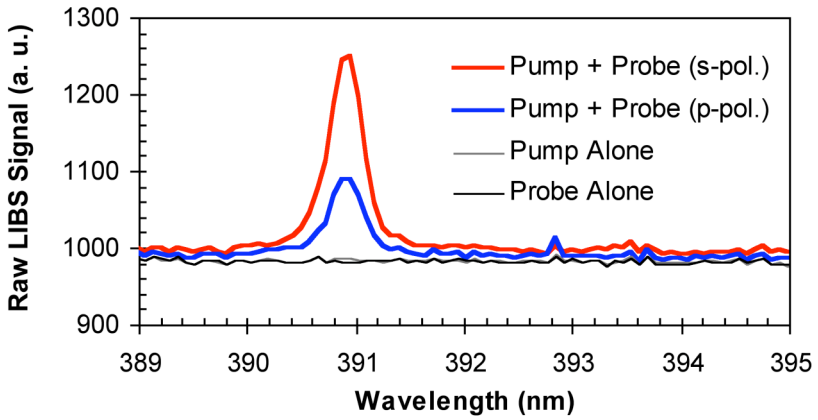

Figure 6.1.17 Dual fs laser pulse raw LIBS signal from Si(100) as a function of wavelength. The cases of no probe (or pump alone) and no pump (probe alone) resulted in no significant signal above the background at the wavelength of 390.874 nm, the characteristic wavelength of silicon. With the pump and probe both present an enhancement in raw LIBS signal was observed. With the probe s-polarized relative to the sample surface, signal exceeding the background by approximately 260 counts was apparent at the characteristic wavelength for silicon, while a lesser enhancement was observed when the probe pulse was p-polarized relative to the sample surface. In all cases the pump pulse laser fluence was 1.7 J/cm^2, while the probe fluence was 46.8 J/cm^2 for the s-polarized case and 42.2 J/cm^2 for the p-polarized case. The probe was focused at a distance of 30 μm above the sample surface and was delayed by 18.1 ns with respect to the pump pulse.

whereupon this material was aggressively ionized, generating significant optical emission and measurable signal at the characteristic wavelength for Si in the measured LIBS spectrum. The energy in the pump pulse was further reduced until signal resulting from the ablating action of the probe pulse was just above the background level, yielding the minimum surface damage.

A plot of the measured LIBS spectra near 390.874 nm for exposure of the pump-pulse alone, probe-pulse alone, pump and probe both present with the probe *s*-polarized, and pump and probe both present with the probe *p*-polarized relative to the sample is shown in Figure 6.1.17. As is apparent from Figure 6.1.17, no signal was observed at the characteristic wavelength above the background when the pump or probe pulse acted alone. With both the pump and probe exposed, a peak was observed in the acquired LIBS spectrum at the characteristic wavelength for Si, with a significant enhancement observed for the case of the probe being *s*-polarized relative to the sample surface. For single-pulse LIBS (pump alone, no probe), the minimum pump laser fluence required to observe Si in the acquired LIBS spectrum was approximately 2.6 J/cm^2 (see

Figure 6.1.18). For dual-pulse LIBS (pump and probe exposed, probe s-polarized at a height of 30 ± 5 μm above the surface), the minimum pump laser fluence required to observe Si in the acquired LIBS spectrum was approximately 1.4 J/cm^2 (see Figure 6.1.19). Furthermore, Figures 6.1.18 and 6.1.19 demonstrate that the pump-fluence of 1.4 J/cm^2 for DP-LIBS produces similar signal amplitude as single-pulse LIBS at a pump laser fluence of 3.4 J/cm^2.

Figure 6.1.20 presents OM and AFM of single shot fs laser induced ablation features associated with single-pulse and dual-pulse LIBS corresponding to the pump laser fluences of the spectra presented in Figures 6.1.18 and 6.1.19. The threshold pump fluence for single pulse LIBS (2.6 J/cm^2) resulted in an ablation crater with a maximum depth of 538 nm (Figure 6.1.20a)). The threshold pump fluence for dual pulse LIBS (1.4 J/cm^2) resulted in an ablation crater with a maximum depth of 123 nm (Figure 6.1.20f)). It was observed that the laser induced damage to the sample surface (depth or diameter of ablation crater) was independent of the presence or absence of the probe pulse probe, indicating that the probe pulse did not cause damage to the sample surface.

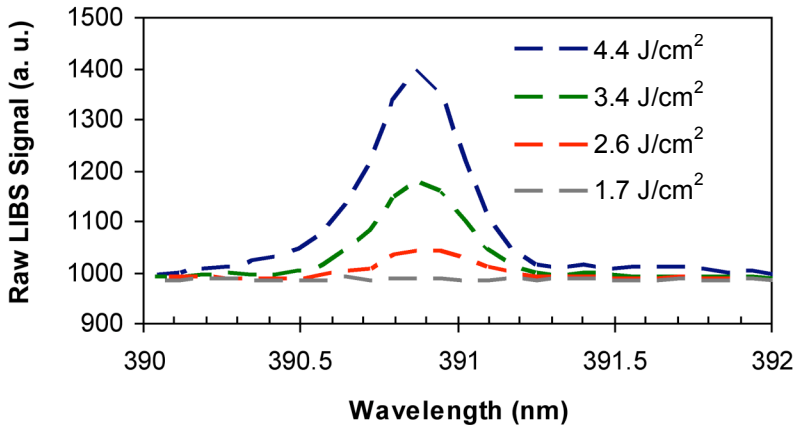

Figure 6.1.18 Single-pulse (pump-pulse alone) LIBS spectra near the characteristic wavelength of Si (390.874 nm) for multiple pump-pulse laser fluences. The laser fluence of the pump-pulse is indicated in the legend, ant the probe pulse was not exposed during collection of these spectra. The plot indicates that the pump laser fluence threshold for single pulse LIBS is approximately 2.6 J/cm^2.

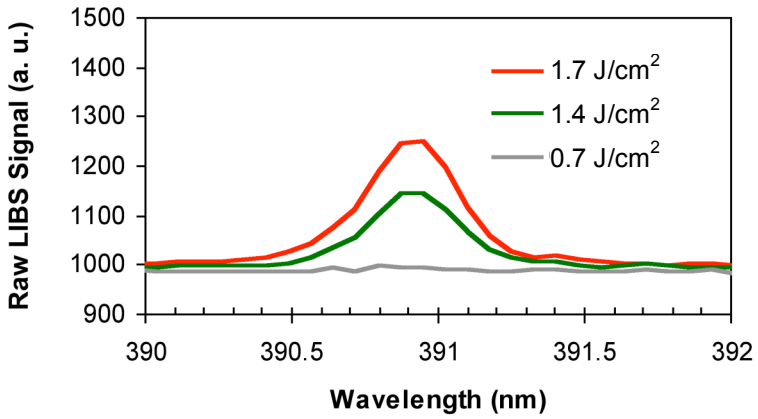

Figure 6.1.19 Dual-pulse (pump and probe pulse exposed) LIBS spectra near the characteristic wavelength of Si (390.874 nm) for multiple pump-pulse laser fluences (pump-pulse fluence shown in the legend). The probe-pulse fluence was held constant at 18.7 J/cm^2 and was s-polarized with respect to the sample surface. Furthermore, The probe was focused at a distance of 30 μm above the sample surface and spectra were collected at pump-probe delays of 18.8 ns for pump fluence = 1.7 J/cm^2, 23.5 ns for pump fluence = 1.4 J/cm^2, and 23.5 ns for pump fluence = 0.7 J/cm^2 . The plot indicates that the pump laser fluence threshold for single pulse LIBS is approximately 1.4 J/cm^2.

The volume of ablated material was obtained from the AFM measurements of ablation craters using a bearing calculation. As the pump pulse energy was decreased the ablated volume and hence mass removed from the sample was similarly decreased. For the dual-pulse case with a pump laser fluence of 1.4 J/cm^2 (Figure 6.1.20f)), an average mass of 2.2 ± 0.79 × 10^{-11} g was removed from the sample, while in the single-pulse case with a laser fluence of 3.4 J/cm^2 (Figure 6.1.20b)) a mass of 5.2 ± 1.34 × 10^{-11} g was ablated from the sample surface. Recall that the signal amplitude (at the characteristic wavelength for Si) for single pulse LIBS at a pump laser fluence of 3.4 J/cm^2 was similar that for dual pulse LIBS at a pump laser fluence of 1.4 J/cm^2. Hence, the dual pulse LIBS technique reduced the depth of ablation craters by approximately 80 % (641 nm for single pulse to 123 nm for dual pulse LIBS) and the mass ablated by approximately 50 % (5.2 ± 1.34 × 10^{-11} g for single pulse to 2.2 ± 0.79 × 10^{-11} g for dual pulse) relative to single pulse LIBS.

The time-resolved dual pulse LIBS measurements provided an estimate of the ablated material velocity. This velocity was obtained by dividing the height of the probe pulse above the sample surface Δz, by the relative time delay between

the arrival of the pump and probe Δt_0 at which signal emerged above the background at the characteristic wavelength for silicon in the acquired DP-LIBS spectrum. For the example presented in Figure 6.1.21 (pump fluence = 1.8 J/cm^2), the LIBS signal at the characteristic wavelength of 390.874 nm emerges at a delay of 17.5 ± 0.5 ns, such that with $\Delta z = 40 \pm 5$ μm, a velocity of 2300 ± 350 m/s is obtained for the ablated material. The ablated material velocity inferred from the DP-LIBS compares favorably with measurements of the ablated material velocity for silicon with native from side-view imaging at similar pump pulse laser fluence. As shown in Figure 6.1.12 the ablated material velocity at a pump laser fluence of 1.3 J/cm^2 was found to be 2130 ± 200 m/s, while at a laser fluence of 2.6 J/cm^2 the ablated material velocity was 2610 ± 200 m/s. This correlation between time-resolved DP-LIBS and side-view pump-probe imaging allowed a distinction to be made between the shock front and material front in the collected side-view images. As the shock front exhibited a far greater velocity (~ 5000 m/s at a pump pulse laser fluence of 2.6 J/cm^2), it would have resulted in signal in the dual pulse LIBS spectrum at a much earlier time delay if it carried significant material.

For the experiments discussed here, the maximum available time delay between the pump and probe, was $\Delta t = 23.45$ ns, which when coupled with a minimum probe height of $\Delta z \approx 25$ μm (to avoid clipping the edge of the sample with the probe pulse), placed a lower limit on the velocity of the ejected material of around 1000 m/s. Hence for lower pump-pulse laser fluence and lower ejected material velocities, it is conceivable that the ablated material may be moving too slow to be accessed by the probe pulse. By using greater temporal delays, it is conceivable that the laser induced surface damage could be further reduced by decreasing the pulse fluence of the pump pulse toward the fs laser induced ablation threshold for Si (100) with native oxide (0.38 ± 0.02 J/cm^2, see Chapter 4.1). The lowest pump laser fluence observed to provide significant signal enhancement with dual pulse LIBS was 1.4 J/cm^2, which is greater than three times the ablation threshold of Si(100). Relative to reported fluence values for the plasma threshold of silicon of ~1.0 J/cm^2 [15], we find that our LIBS signal was

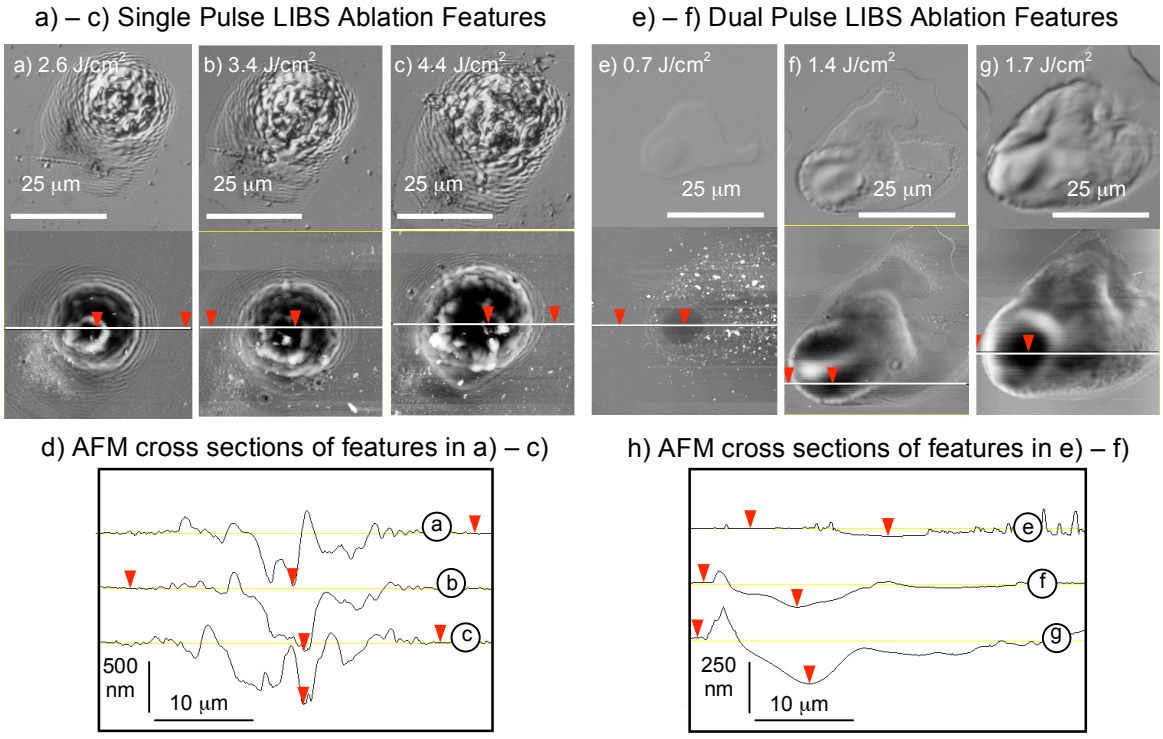

Figure 6.1.20 Nomarski OM and AFM of single pulse ablation features produced during a) – d) single pulse LIBS and e) – h) dual pulse LIBS at pump-pulse laser fluences shown. NOM images are provided on top, and AFM images are provided at the bottom, with the associated AFM cross section scans provided in d) and h). AFM indicates maximum depth of features were: a) 538 nm b) 641 nm c) 639 nm e) 39 nm f) 123 nm g) 231 nm.

lost at much higher fluences for single and dual pulse LIBS (~2.7 J/cm^2 and ~1.4 J/cm^2 respectively). This is attributed to a lack of sensitivity of the CCD array within the spectrometer, which was improved with the acquisition of a new intensified CCD camera in later studies.

In order to understand the mechanism underlying the observed enhancement of LIBS signal using the orthogonal dual-pulse technique, it is necessary to understand the properties of the ejected or ablated material following fs laser ablation (see Chapter 2.4.2 for more discussion). Far above the threshold for fs laser induced damage, the ablated material involves the formation of dense plasma of ions and electrons along with sub-micrometer molten particulates [15, 65, 68, 69, 71, 72]. The relaxation of excited electrons within this plasma serve as the source of photons for spectra collected during LIBS. As the laser pulse energy is decreased toward the threshold for damage, the ablated material is increasingly comprised of denser material, eventually taking the form of a liquid

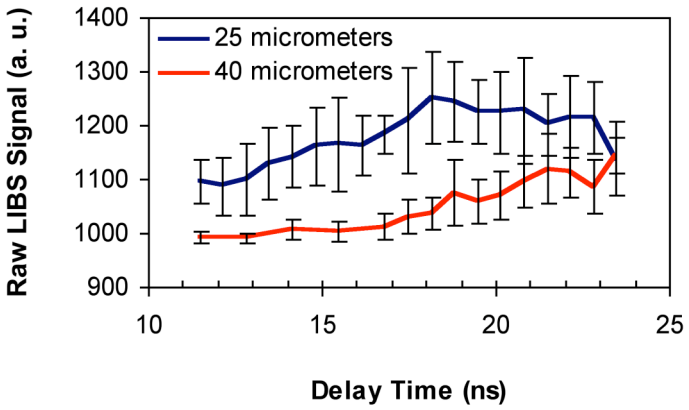

Figure 6.1.21 LIBS raw signal for dual pulse LIBS as a function of time delay between the pump and probe pulse at the sample surface. Data from two probe heights (25 ± 5 μm and 40 ± 5 μm) are presented. For a probe height of 40 μm the LIBS signal emerges above the background (990 counts) at around 17.5 ± 0.5 ns, yielding an ablated material velocity of ~ 2300 m/s.

layer of ablated material that travels outward from the surface due to the force of the ablation event [34-38]. This liquid layer is not expected to be a significant source of characteristic photons, so that near the ablation threshold the LIBS signal resulting from a single laser pulse alone has very little amplitude at the associated characteristic wavelengths.

For the case of orthogonal DP-LIBS, the high intensity probe laser pulse encounters and ionizes the dense liquid layer resulting from the ablation initiated by the low energy pump, creating the dense plasma needed as a source of characteristic photons. Other dual pulse techniques that have been used to enhance LIBS sensitivity to small mass percentage constituents in more complex materials largely operate in the high laser fluence regime in which the ablated material takes the form of energetic plasma [192]. The enhancements observed there may result from “re-pumping” or further ionizing the plasma, resulting in greater emission intensity at the characteristic wavelengths in the LIBS spectrum for a particular material. In these previous studies, damage to the sample was not a concern and therefore lower pump laser fluences were not pursued [192, 199].

In summary, a quasi non-destructive orthogonal dual-pulse LIBS technique was demonstrated on Si(100) using a fs pulsed laser. In contrast to previous

works [192-196], the threshold pump-laser fluence for DP-LIBS detection was determined (1.4 J/cm^2) demonstrating significant decreases in the volume and mass of material removal required for LIBS analysis. The technique may be improved further with more sensitive spectra collection tools, and a larger temporal delay between the arrival times of the probe and pump pulses. This technique was also applied to limit surface damage during LIBS analysis of the CMSX-4 Ni-based superalloy, the results of which are presented in Chapter 6.2.3.

6.2 Fs laser ablation dynamics of the Ni-based superalloy CMSX-4

The dynamics of single pulse fs laser ablation of the Ni-based superalloy were studied in-situ with pump-probe microscopy [41, 65, 71] and dual pulse laser induced breakdown spectroscopy (DP-LIBS) [192-196]. Furthermore, the dynamics were simulated using FLASH hydrodynamic code [220] seeded with initial conditions provided by 1D Hyades code [211]. A connection between the ablation dynamics within the first 10.36 ns and the transition in ablated crater depth as a function of incident pump-pulse fluence (see Chapter 4.3.2) was revealed through analysis of the ablation air-shock dynamics present in time-resolved side-view shadowgraphic images. The orthogonal DP-LIBS technique was explored as a means for quasi non-destructive evaluation of the CMSX-4 superalloy, and provided further insight into the ablation dynamics by elucidating image contrast observed during pump-probe microscopy experiments. Finally, simulation of the single pulse fs laser ablation event, pursued in collaboration with Musoumi Das and Katsuyo Thornton, completed the picture of the ablation event validating the presence of a jetting phenomenon which accompanied removal of material. The results of these studies are presented in the following sections.

6.2.1 Pump-probe side-view shadowgraphic imaging of fs laser ablation of the Ni-based superalloy CMSX-4

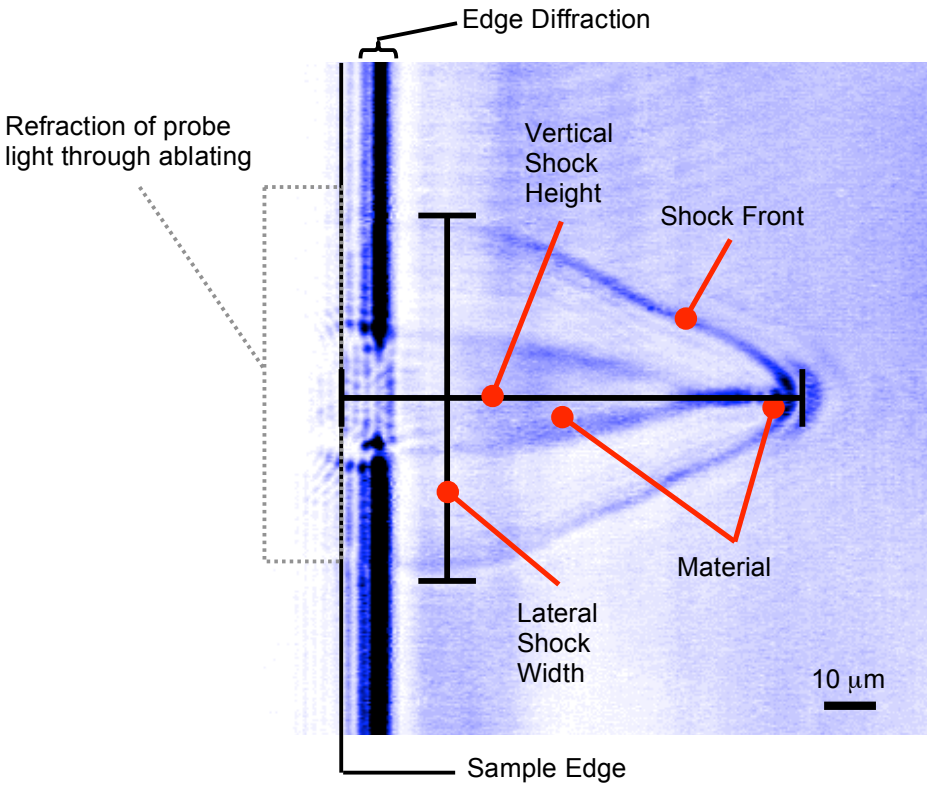

Figure 6.2.1 Side-view image of fs laser ablation of the Ni-based superalloy CMSX-4 at a laser fluence of 10.1 J/cm^2, collected 10.36 ns following absorption of the pump pulse at the sample surface. The laser was incident from the right in the image. Image features including the air shock front, ablating material, sample edge, and edge diffraction are indicated. A refraction feature to the left of the sample edge is also apparent in the image, resulting from the probe pulse passing through the ablation event.

The experimental details for pump-probe side-view shadowgraphic imaging are presented in Chapter 3.3.2. Briefly, the fs pulsed laser beam was split into separate pump and probe beam lines using an 80/20 ultrafast beam splitter. The pump pulse was directed at normal incidence onto the sample surface to initiate the ablation event, while the probe pulse was weakly focused laterally across the sample surface illuminating the ablation event and producing a shadowgraph of the ablation event on a CCD camera located on the other side of the sample [41, 65, 71]. Sub-picosecond (ps) image exposure time was obtained by using the ~200 fs probe laser pulse as the illumination source (the laser pulse was

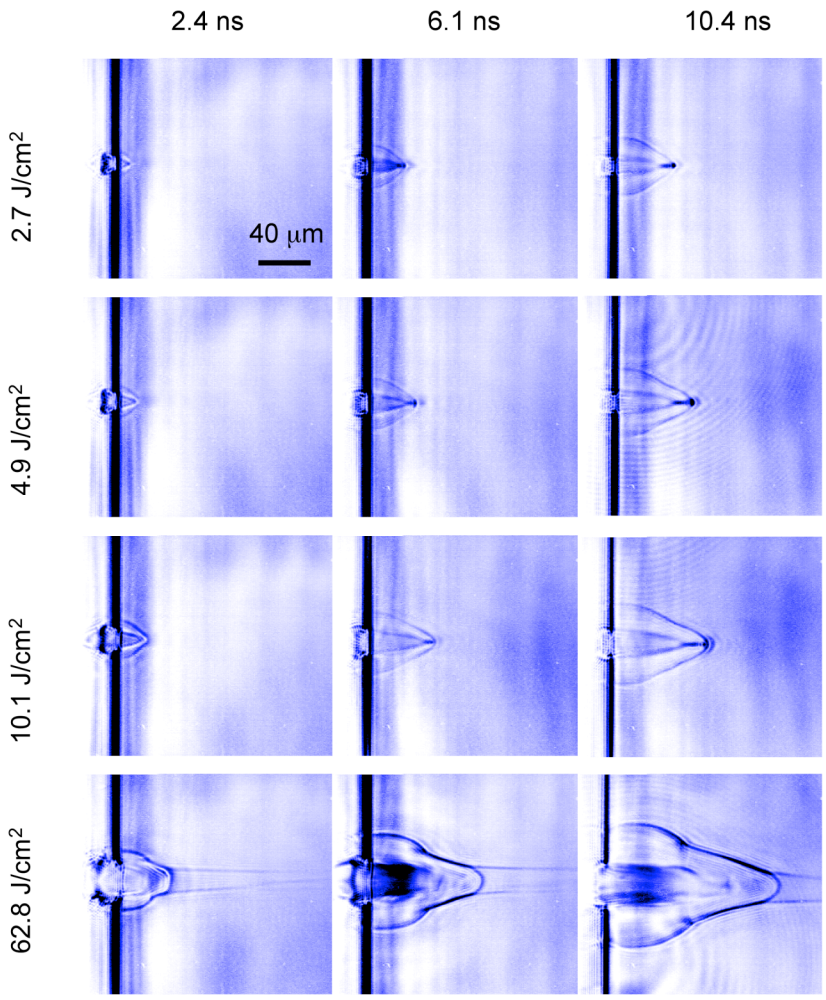

Figure 6.2.2 Shadowgraphic, side-view images of femtosecond laser ablation of the Ni-based superalloy CMSX-4. Images of ablation events produced over a range of laser fluences (at left) are shown at several time delays (at top) relative to the arrival of the pump laser pulse. The scale marker in the upper left image applies to all images, and all images have been inverted with respect to the originals.

anticipated to spread in time from approximately 150 fs to ~ 200 fs due to group velocity dispersion encountered upon transmission through various optical elements [265]). By delaying the arrival time of the probe with respect to the probe, images of the ablation event were captured over the time range from 0 – 10.36 ns following the onset of ablation. The ablation dynamics were studied for a range of pump-pulse laser fluences from F_{inc} = 1.23 – 62.8 J/cm^2. The propagation of the ablation event is discussed with respect to the sample surface, such that the “vertical shock front” propagates perpendicular to the sample surface, while the “lateral shock front” propagates in the direction parallel

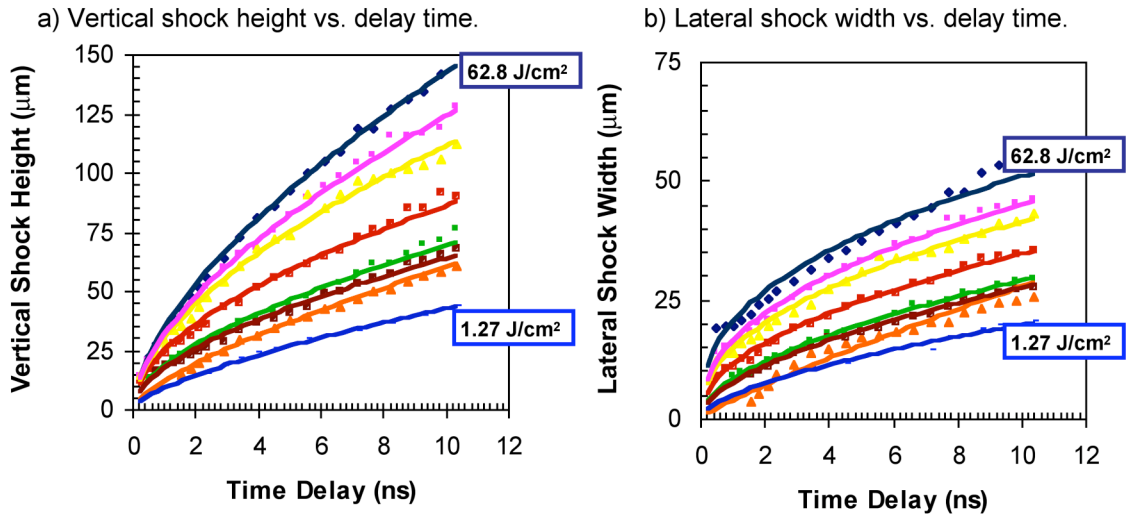

Figure 6.2.3 Dimensions of air shock accompanying femtosecond laser ablation of CMSX-4 superalloy. a) Vertical shock height as a function of time delay. b) Lateral shock width (or radius) as a function of delay time. Measurements for laser fluences 62.8 J/cm^2 and 1.27 J/cm^2 are indicated, while measurements in between in descending order are for laser fluences of 30.4 J/cm^2, 20.4 J/cm^2, 10.1 J/cm^2, 4.9 J/cm^2, 3.92 J/cm^2, and 2.7 J/cm^2. Error in vertical measurements was ± 2 μm, while error for lateral measurements was ± 1 μm. The results of a power law fits to the data are presented in the plots.

to the sample surface. It should also be emphasized that the shock wave observed here propagates in the air in front of the sample, not within bulk sample material.

An example side-view shadowgraphic image is presented in Figure 6.2.1 where various image features are explained. Edge diffraction generated by the sample edge as the probe pulse passes laterally across the sample surface, producing a series of interference fringes parallel to the sample surface [65, 263]. Distinction between the material front and shock front in the side-view images was not as obvious as it was for images of fs laser ablation of Si(100) with thin oxide surface films (see Chapter 6.1.2). The material and shock fronts indicated in Figure 6.2.1 were subsequently verified with time resolved DP-LIBS experiments and FLASH code simulations (see Chapters 6.2.2 and 6.2.3). Side-view shadowgraphic images for several laser fluences over a range of time delays are presented in Figure 6.2.2. In the images at a laser fluence of 62.8 J/cm^2, a shock wave is observed in the air in front of the sample associated with the fs laser induced breakdown of the air [72]. Significant air breakdown was

observed for laser fluences greater than or equal 20.4 J/cm^2, and the presence of the air breakdown was observed to encourage vertical expansion of the shock wave by pulling the shock into the region of rarified gas within the air breakdown shock. Of particular interest was the presence of a jetting phenomenon in which a small amount of ablating material is seen to drive the shock wave in the air in front of the sample. This jetting phenomenon is presumed to yield the v-shape of the shock waves in air for images of ablation at laser fluences of 2.7 J/cm^2, 4.9 J/cm^2, and 10.1 J/cm^2 shown in Figure 6.2.2. This phenomenon may be related to observation of nanojet fs laser ablation morphology features observed on gold films [142]. At the center of the ablation event where the laser fluence is the highest, the material may reach sufficiently high temperatures which cause a dramatic decrease in the local viscosity, allowing a low density volume of material to jet away from the surface. The defined v-shape is modified in the images of ablation at 62.8 J/cm^2 due to the previously mentioned laser induced air breakdown.

The measured vertical shock height and lateral shock width as a function of time delay following the onset of ablation are presented in Figure 6.2.3. The vertical shock height was measured with respect to the first sample surface, which was located to the left of the first edge diffraction maximum [263]. The lateral shock width (or radius) was measured at a height of approximately 4 μm above the sample surface as the edge diffraction obscured the presence of the shock wave closer to the sample. Power law least square fits have been applied to the data in Figure 6.2.3. Following Sedov's theory for shock wave propagation, the radius of the ablation shock or blast wave as a function of time is given by:

$$r = \lambda \left(\frac{E_o}{\alpha \rho_1} \right)^{1/(2+\nu)} t^{2/(2+\nu)} \qquad (6.2.1)$$

where E_0 is the energy release responsible for the observed shock, ν is the dimensionality of the shock expansion, ρ_1 is the density of the propagating medium (in this case air, ρ_1 = 1.25 kg/m^3), α is an additional proportionality constant dependent on the dimensionality of expansion (α = 1.2 and 0.851 for ν = 1 and 3 respectively [169]), λ is a constant (which has been set to 1 for our

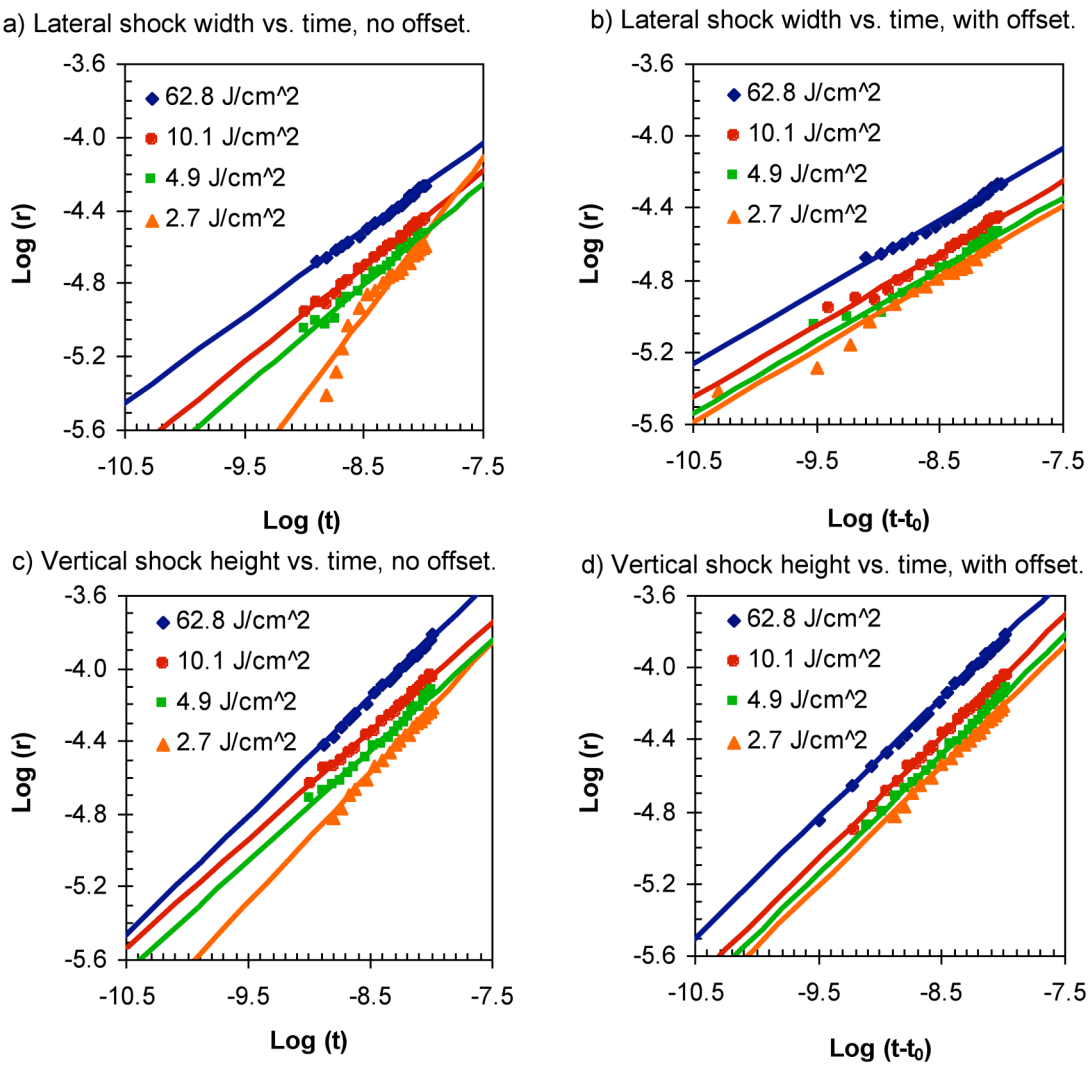

Figure 6.2.4 Log-Log plots of shock dimensions vs. delay time demonstrating the effect of introducing the time offset t_o. a) Lateral shock full width vs. delay time before offset. b) Lateral shock full width vs. delay time with time offset. Common slope indicates common shock expansion dimensionality. c) Vertical shock height vs. delay time before offset. d) Vertical shock height vs. delay time with time offset.

purposes [65]), and *t* is the delay time. As discussed in Chapter 6.1.2, a fitting routine can be applied to the measured shock dimensions as a function of time to yield the energy release E_0, and dimensionality ν, associated with the observed shock dynamics. As also discussed in section 6.1.2, application of Sedov's theory requires that the dimensionality of the shock expansion to be an integer value (i.e. ν = 1, 2, or 3). Furthermore, different data sets must have a common expansion dimensionality in order for comparisons of the energy release to be made.

Table 6.2.1 Shock expansion fitting parameters for fs laser ablation of the Ni-based superalloy CMSX-4.

Lateral Shock					
Laser Fluence (J/cm^2)	**Initial Dimensionality (ν_0)**	**Initial R^2**	**Assumed Dimensionality (ν)**	**Time Offset (t_0) (ns)**	**Final R^2**
62.8	3.0	0.96	3.0	0.50	0.99
30.4	2.5	0.98	"	0.49	0.99
21.0	2.4	0.99	"	0.52	0.99
10.1	2.1	0.99	"	0.63	0.98
4.9	1.6	0.99	"	0.71	0.96
3.92	1.5	0.99	"	1.02	0.99
2.7	0.3	0.93	"	1.51	0.97
1.23	1.3	0.98	"	1.72	0.95
Vertical Shock					
Laser Fluence (J/cm^2)	**Initial Dimensionality (ν_0)**	**Initial R^2**	**Assumed Dimensionality (ν)**	**Time Offset (t_0) (ns)**	**Final R^2**
62.8	1.2	1.00	1	-0.092	1.00
30.4	1.3	1.00	"	-0.17	1.00
21.0	1.5	0.99	"	-0.28	0.99
10.1	1.7	0.99	"	-0.38	1.00
4.9	1.4	0.99	"	-0.31	1.00
3.92	1.5	0.99	"	-0.44	1.00
2.7	0.8	1.00	"	0.26	1.00
1.23	0.9	0.99	"	0.12	0.99

The vertical shock dimensionality from power law fits to the raw data ranged from $\nu_{0,vertical}$ = 0.8 – 1.7, while the lateral shock dimensionality ranged from $\nu_{0,lateal}$ = 0.3 – 3.0 (see Table 6.2.1). To facilitate analysis and interpretation, shock dimensionalities of $\nu_{vertical}$ = 1 and $\nu_{lateral}$ = 3 were imposed on the data sets [72]. This was done by introducing a time offset t_0 into Equation 6.2.1 above (as discussed in Chapter 6.1.2), yielding an expression for the air shock radius of the form:

$$r = \lambda\left(\frac{E_o}{\alpha\rho_1}\right)^{1/(2+\nu)}\left(t - t_0\right)^{2/(2+\nu)} \qquad (6.2.2)$$

The time offset t_0 was then adjusted for each data set to produce the desired expansion dimensionality from a least-square power law fit. The effect of the time offset is best shown by considering the log-log plots of the raw and time offset

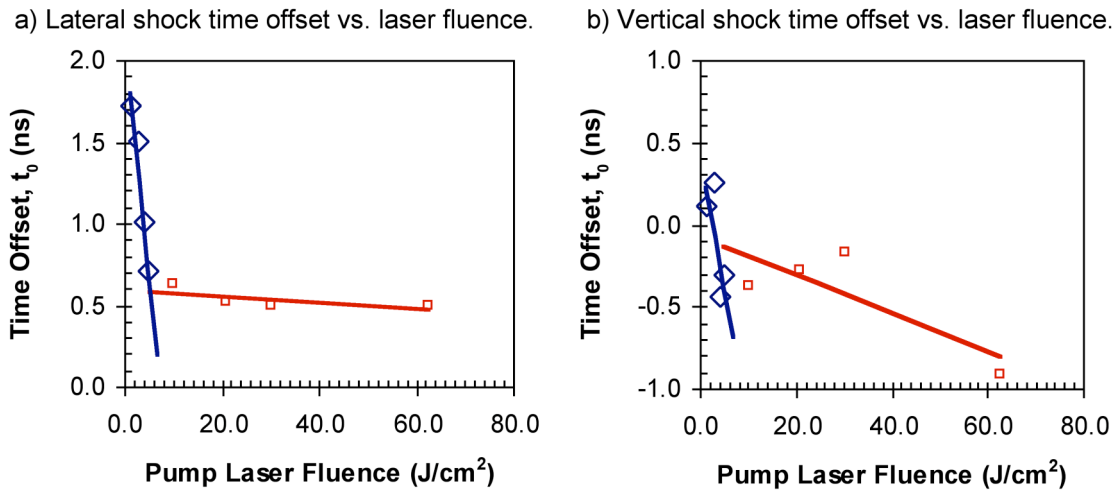

Figure 6.2.5 a) Time offset t_0 applied to Equation 5.2.2 to obtain common shock expansion dimensionality (ν = 3) for lateral shock wave as a function of pump-pulse laser fluence. b) Time offset t_0 applied to Equation 5.2.2 to obtain common shock expansion dimensionality (ν = 1) for vertical shock wave as a function of pump-pulse laser fluence.

adjusted lateral shock dimension data presented in Figure 6.2.4. Taking the logarithm of both sides of Equation 6.2.2 above yields:

$$Log(r) = \left(\frac{1}{2+\nu}\right) Log\left(\frac{E_0}{\alpha \rho_1}\right) + \left(\frac{2}{2+\nu}\right) Log(t - t_0) \qquad (6.2.3)$$

Placed in this format, the slope of linear fits applied to the data in Figure 6.2.4 yield the dimensionality of the shock expansion, while the y-axis intercept yields the energy release E_0 (assuming that the constant α, and the density of air ρ_1 are known). It is clear that the slope of lines are not the same between data sets in Figure 6.2.4 a) and c), while the application of the time offset t_0 results in a common slope and thus expansion dimensionality a shown in Figure 6.2.4 b) and d).

The time offset applied to the vertical and lateral shock dimensions as a function of the incident pump-pulse laser fluence is presented in Figure 6.2.5. Two regimes are observed for the time offset applied to the lateral shock radius as a function of incident laser fluence. The physical significance of the time offset is dependent on the expansion direction under consideration. For measurements of vertical shock height, the time offset reflects the accuracy with which the edge of the sample was located as a reference for measurements (± 2 μm), and the

accuracy with which time zero was determined (time zero is the delay time at which the pump and probe arrive simultaneously at the sample surface, determined with a stated accuracy of ± 50 ps). Under the assumption that the vertical shock wave exhibits a planar expansion (which has been reported by other studies [41, 72]), it is proposed that for the vertical shock measurements the time offset simply adjusts for experimental error.

The time offset applied to the lateral shock measurements may hold more physical significance. As shown in Figure 6.2.5 a), the time offset was observed to increase with decreasing laser fluence. This suggests that for low fluence ($F_0 \leq$ 4.9 J/cm^2) the initial shock expansion is largely vertical to the sample surface and is followed by a delayed lateral expansion (1-2 ns). For high laser fluence ($F_0 >$ 4.9 J/cm^2) the shock wave begins to expand laterally much sooner (~ 500 ps). Other research groups have reported one-dimensional vertical shock expansion and delayed three-dimensional lateral shock expansion accompanying fs laser ablation of silicon [72]. This group also studied ns laser ablation of silicon at the same incident laser fluence, where analysis of the shock wave revealed that the shock wave immediately exhibits three-dimensional expansions for *both* lateral and vertical shock [72]. The qualitative evolution of the fs laser induced ablation morphology as a function of incident laser fluence was observed to show a transition to a more melt-like morphology at around 2 /cm^2, the emergence of a more explosive ablation morphology at laser fluences exceeding approximately 5.3 J/cm^2 (see Chapter 5.3). Furthermore the depth of ablation craters as a function of laser fluence was found to exhibit a sudden increase at around 6.0 J/cm^2 (see Figure 4.3.2). The combined results from both ablation morphology investigations and analysis of shock dynamics may suggest that fs laser ablation of CMSX-4 superalloy takes on strong thermal ablation characteristics of ns laser ablation at high laser fluence [20, 22, 113, 134, 135, 262]. The physical mechanism underlying the generation of the three-dimensional shock expansion is not yet fully understood, but may be related to the onset of the proposed mechanism of explosive boiling [44, 69, 218] and will be the topic of future research.

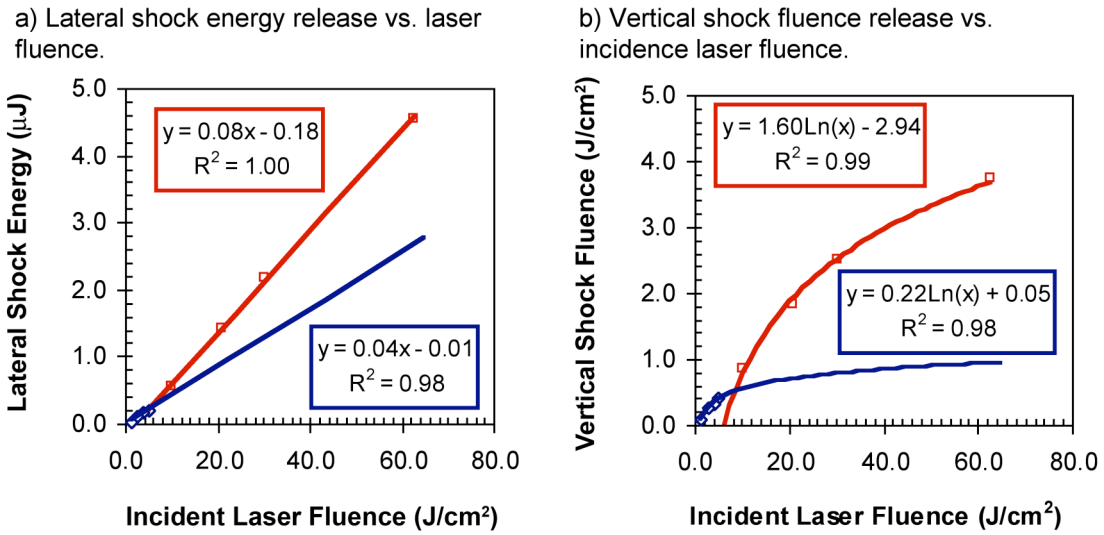

Figure 6.2.6 a) Energy release E_0 underlying lateral shock dynamics as a function of incident pump-pulse laser fluence. b) Fluence release E_0 underlying vertical shock dynamics as a function of incident pump-pulse laser fluence.

The energy release E_0 underlying the observed shock dynamics (presented in Figure 6.2.6) was determined once the appropriate dimensionality was obtained for all data sets through application of the time offset t_0. Recall from section 6.1.2 that the units of the energy release E_0 are dependent on the dimensionality of the shock, such that $[E_0]$ = energy per unit area for $\nu = 1$ (planar release of energy), $[E_0]$ = energy per unit length for $\nu = 2$ (line release of energy), and $[E_0]$ = energy for $\nu = 3$ (point release of energy) [169]. As with the time offset t_0, two regimes of energy release were observed for the lateral shock wave as a function of incident pump-pulse laser fluence, with the transition between the regimes occurring between 4.9 J/cm^2 and 10.1 J/cm^2. This correlation between the shock energy release and the ablated crater depth is further evidence that the early shock dynamics are connected with the ablation morphology long after arrival at the steady state. The efficiency of energy conversion from the incident laser pulse into the lateral shock wave (E_0/incident pump pulse energy E_{inc}) was found to generally increase with laser fluence, with a calculated efficiency of 2.3 % for F_{inc} = 1.23 J/cm^2 and 5.2 % for F_{inc} = 62.8 J/cm^2. The efficiency of energy conversion for the vertical shock was found to be independent of laser fluence, ranging from a minimum of 7.2 % for F_{inc} = 62.8 J/cm^2 to a maximum of 12.3 % for F_{inc} = 2.7

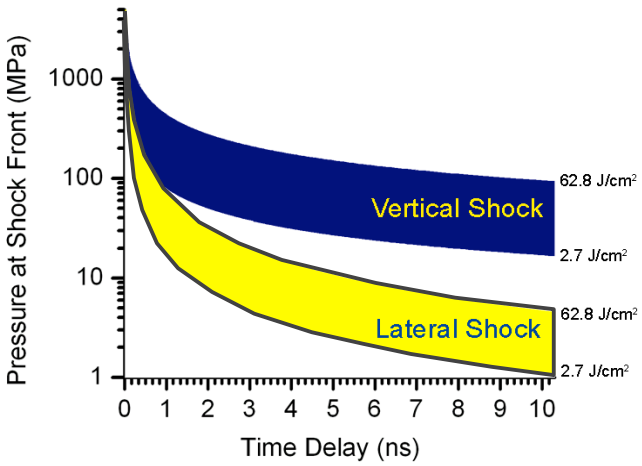

Figure 6.2.7 Pressure at vertical and lateral shock fronts in air as a function of time following the onset of fs laser ablation of the Ni-based superalloy CMSX-4.

J/cm^2. These are comparable with efficiencies observed in other studies [41, 65, 71].

Once the shock dimensionality ν and energy release E_0 were determined, the pressure at the propagating ablation shock front in air was calculated as a function of the reduced time $t' = t - t_0$ by the following equation [169]:

$$P = \frac{8\rho_1}{(\nu+2)^2(\gamma+1)}\left(\frac{E_o}{\alpha\rho_1}\right)^{2/(2+\nu)}(t')^{-2\nu/(2+\nu)} \qquad (6.2.4)$$

where γ = 1.4 is the ratio of the specific heat (the heat capacity of a gas in a constant pressure process to the heat capacity of a gas in a constant volume process). The pressure at the vertical and lateral shock fronts as a function of time is provided in Figure 6.2.7. According to Equation 6.2.4, the pressure at the shock front in the air in front of the sample exceeds 1 GPa for the first several hundred picoseconds following the onset of ablation. Assuming Newton's third law applies [266], an equal and opposite shock wave is sent into the material underlying the ablation event at the sample surface. The heavy dislocation density observed (via cross section TEM) to accompany high fluence fs laser ablation (F_0 = 40.3 J/cm^2) may result from shock waves of this magnitude [267]. It should be noted however, that Equation 6.2.4 has a singularity at t' = 0, bringing into question whether Sedov's prediction of the pressure is applicable for such

early times following the onset of ablation. Simulations of fs laser ablation similar to those presented in Chapter 6.2.3 may provide further insight into the propagation of shock waves into the material resulting from high fluence fs laser ablation.

In summary, the dynamics of fs laser ablation of the Ni-based superalloy CMSX-4 were studied in-situ with pump-probe side-view microscopy. The collected images reveal that a jetting phenomenon accompanies fs laser induced material removal, in which a small amount of material leads a the shock wave produced in the air in front of the sample as a result of the sudden thermal expansion of the surface accompanying absorption of the incident laser energy. Analysis of the dynamics of the shock wave demonstrate correlation between shock dynamics and the resulting ablation morphology, as transitions in the calculated energy release from the measured shock dynamics were found to occur at similar laser fluences as the transition from smooth to explosive damage morphology discussed in Chapter 5.3, and the transition to greater ablated crater depths as a function of laser fluence (around 6 J/cm^2) discussed in Chapter 4.3.2. Future work may include front-view microscopy of fs laser ablation of the CMSX-4 superalloy, but with laser fluences closer to the measured ablation threshold of 0.38 ± 0.02 J/cm^2 (see Chapter 4.3.1).

6.2.2 Orthogonal, dual-pulse femtosecond laser induced breakdown spectroscopy of the Ni-based superalloy CMSX-4.

Surface chemistry characterization of the Ni-based superalloy was performed using fs laser based laser induced breakdown spectroscopy (LIBS). In order to reduce the surface damage resulting from this technique, an orthogonal dual-pulse LIBS (DP-LIBS) method was employed and compared with results from single-pulse LIBS [192-196, 199]. The experimental details of this technique are presented in Chapter 3.3.2, and the results DP-LIBS applied to Si(100) with native oxide are presented in Chapter 6.1.4. Briefly, LIBS in general is performed by collecting the light emitted by the plasma produced during a laser ablation event. As the incident laser fluence is decreased, the damage to the sample

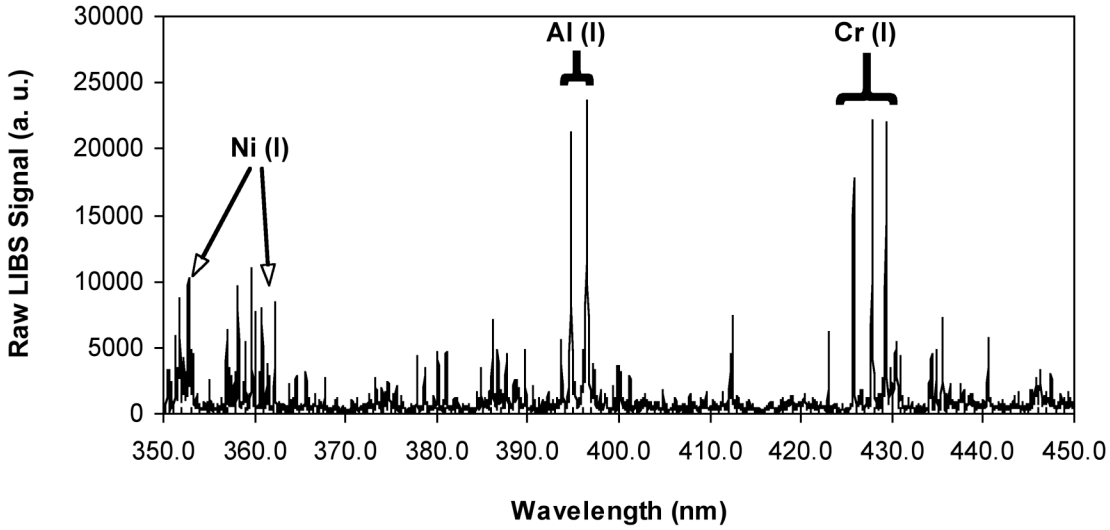

Figure 6.2.8 Typical LIBS spectra of the CMSX-4 superalloy, with peaks corresponding to the first ionized states of major constituents indicated for Ni at 352.454 nm and 361.939 nm, Al at 394.4006 nm and 396.152 nm, and Cr at 425.435 nm, 427.48 nm, and 428.972 nm.

surface also decreases, along with the intensity of the optical emission. Eventually the plasma emission ceases, however material removal is still observed. For example, the fs laser ablation threshold of silicon is around 0.37 J/cm^2 (see section 4.1.2), however the laser fluence at which the plasma diminishes, the so-called plasma threshold, is around 1.0 J/cm^2 [15].

In an effort to minimize the surface ablation associated with LIBS, the technique of orthogonal DP-LIBS explored here uses pump laser fluences below the plasma threshold (for the given LIBS setup), but above the ablation threshold of the CMSX-4 superalloy. In this fluence regime there is not adequate optical emission accompanying the ablation event for single pulse LIBS analysis, however material is still ablated from the sample surface. The goal of DP-LIBS is to ionize this material once it has moved far enough away from the sample surface. To this end, a high fluence probe pulse is directed parallel to the sample surface where it encounters and aggressively ionizes the material ablated by a low fluence pump pulse, producing the plasma and optical emission necessary for LIBS analysis (often referred to as re-heating the plasma [192, 199]). In this fashion, pump-pulse laser fluences can be used near the ablation threshold where damage to the sample is minimized, while LIBS analysis can still be performed yielding the desired information on surface chemistry. Furthermore,

the time-resolved pump-probe nature of the DP-LIBS technique yields relevant information such as the ablated material velocity, facilitating interpretation of the shadowgraphic images presented in Chapter 6.2.1. The results of this study, including comparisons of single- and dual-pulse LIBS signal strengths and associated surface damage, are presented in the following section.

The general approach of the experiments performed here was to compare the laser fluence threshold and associated ablation morphology for DP-LIBS with that of single-pulse LIBS. Initially, single-pulse LIBS spectra were collected at normal laser incidence (only the pump pulse exposed) with a range of gradually decreasing pump pulse laser fluence. Spectra were also intermittently collected with the pump and probe both exposed (DP-LIBS), at a fixed probe pulse laser fluence of 270 J/cm^2, with the edge of the probe pulse a fixed height above the sample of $\Delta h = 30 \pm 2.5$ µm, arriving with a delay of 10.36 ns with respect to the pump pulse. A series of time-resolved DP-LIBS was then performed (fixed probe height, variable pump/probe delay) once the threshold pump-pulse fluence for DP-LIBS was determined. Following spectra collection, the ablation morphology was investigated ex-situ using AFM and OM.

For reference, the composition of the CMSX-4 superalloy in weight percent is: 61.42% Ni, 9.6% Co, 6.6% Ta, 6.4% Cr, 6.4% W, 5.64% Al, 2.9% Re, 1.03% Ti, and 0.1% Hf [55]. Elements which produced the brightest optical emission in the collected LIBS spectra of the CMSX-4 superalloy were Ni, AL, and Cr. The characteristic wavelengths in the LIBS spectra for these elements were: 352.454 nm for Ni, 425.435 nm for Cr, and 394.4006 nm and 396.152 nm for Al. Optical emission was observed for the minor constituents in the collected LIBS spectra as well, with the exception of Hf which was not identified possibly due to the close location of Hf peaks with other stronger emission lines [228]. A typical LIBS spectrum of the CMSX-4 superalloy is shown in Figure 6.2.8 where peaks corresponding to Ni, Cr, and Al have been identified.

Signal amplitude in arbitrary units at the characteristic wavelengths of Ni, Al, and Cr as a function of the pump-pulse laser fluence for both single-pulse and DP-LIBS is presented in Figure 6.2.9. The laser fluence of the probe pulse was

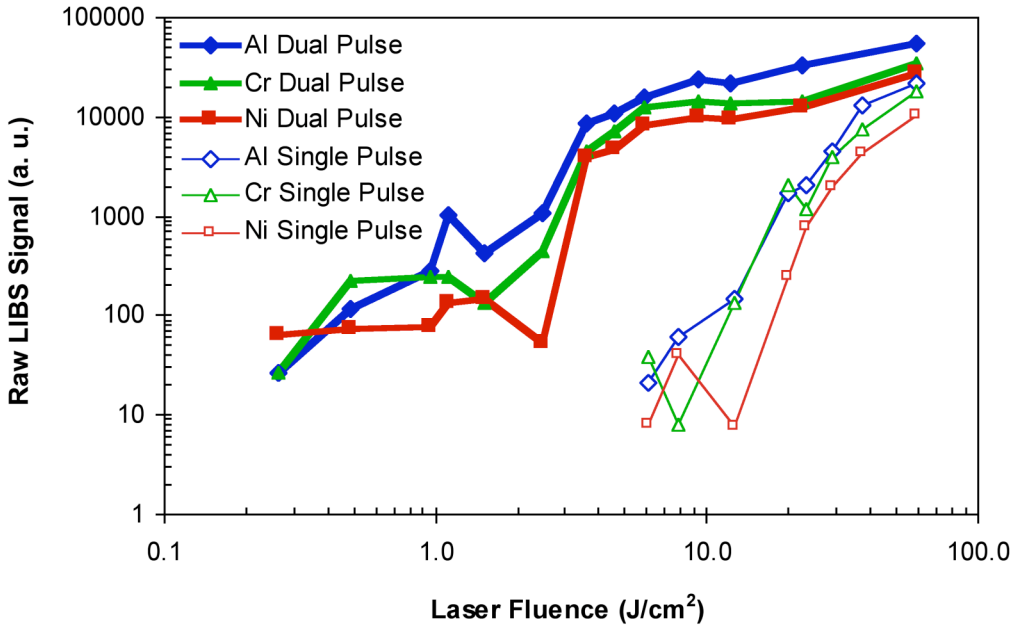

Figure 6.2.9 Raw LIBS signal vs. pump (P1) laser fluence for both single pulse LIBS (thin lines, hollow markers) and dual pulse LIBS (thick lines, solid markers). Using a S/N ratio of 10 as a criteria for detection, the raw LIBS signal detection limit was around 100 counts, such that for single pulse LIBS, detection of the major constituents was possible down to a laser fluence of 10.1 J/cm^2, while with dual pulse LIBS, the major constituents were detectable down to a laser fluence of 1.12 J/cm^2 with Al and Cr apparent down to 0.49 J/cm^2. The probe pulse was focused above and parallel to the sample surface at a height of 30 μm.

fixed at 270 J/cm^2 for all data collected for DP-LIBS. A signal-to-noise ratio exceeding 10 was used a criterion for detection of a particular element. Provided a typical background level of around 10 counts in the collected LIBS spectra (at pump laser fluences near the ablation threshold), signal amplitude exceeding 100 counts was generally sufficient for positive identification of a particular element within the acquired LIBS spectrum. Note that the background signal level was found to depend on the degree of CCD cooling (typically cooled to -10°C), and the incident laser fluence, with the noise increasing for increasing pump-pulse laser fluence.

With our criterion for detection, Figure 6.2.9 demonstrates that for single-pulse LIBS, Ni, Al, and Cr were no longer identified when the pump laser fluence was decreased below ~ 10 J/cm^2. For DP-LIBS, Ni was identified in the obtained spectra for pump laser fluences down to 1.12 J/cm^2, while Al and Cr were apparent down to pump laser fluences of 0.49 J/cm^2. The ablation threshold of

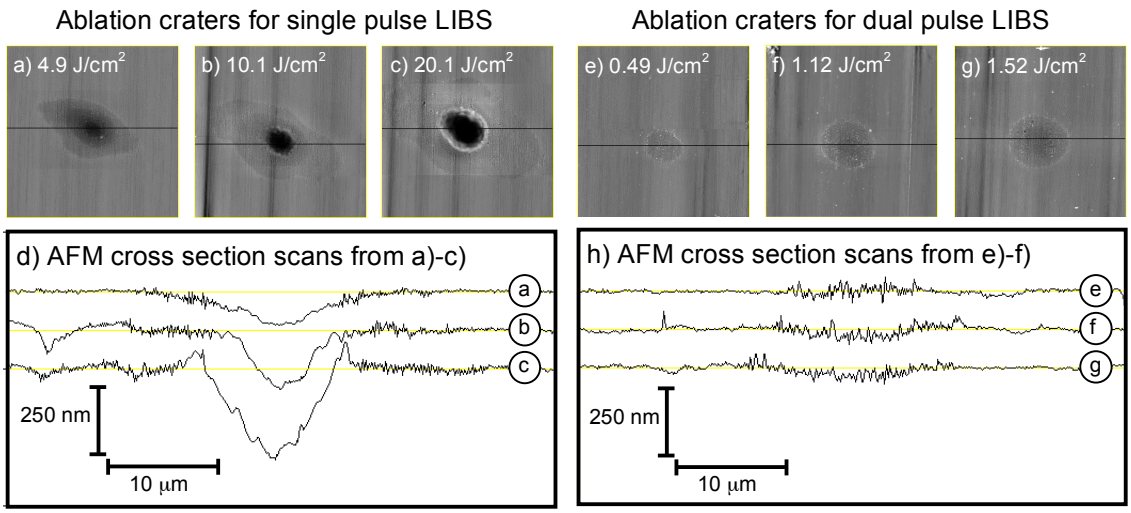

Figure 6.2.10 Atomic force microscopy (AFM) of single shot fs laser damage features on the CMSX-4 superalloy produced during single-pulse (at left) and dual-pulse (at right) LIBS analysis. Each image is 50 μm by 50 μm. a) 4.9 J/cm^2, max. depth = 144 nm b) 10.1 J/cm^2, max. depth = 212 nm c) 20.1 J/cm^2, max. depth = 324 nm. d) AFM cross sections of features in a) – c). e) 0.49 J/cm^2, max. depth = 33 nm f) 1.12 J/cm^2, max. depth = 54 nm g) 1.52 J/cm^2, max. depth = 62 nm. h) AFM cross sections of features in e) – g). The threshold pump laser fluence for single-pulse LIBS was 10.1 J/cm^2, while the threshold for dual-pulse LIBS was 1.12 J/cm^2. The measured fs laser ablation threshold of the CMSX-4 superalloy is 0.38 ± J/cm^2.

the CMSX-4 superalloy was measured to be 0.38 ± 0.02 J/cm^2 (see Chapter 4.3.1), such that the threshold laser fluence for single pulse LIBS detection was approximately 30 times the ablation threshold, while the threshold for detection for dual-pulse LIBS was 2-3 times the ablation threshold.

AFM of the fs laser induced surface damage associated with single-pulse LIBS spectra collection is shown in Figure 6.2.10. For single pulse LIBS, ablation at pump laser fluences of 20.1 J/cm^2 and 10.1 J/cm^2 produced sufficient optical emission for identification of Al, Ni, and Cr, while signal amplitudes at the characteristic wavelengths for a pump laser fluence of 4.9 J/cm^2 did not exceed the s/n of 10 chosen as the criterion for detection. At a pump laser fluence of 10.1 J/cm^2, a damage crater was produced on the sample surface with depth of around 200 nm. We conclude that under the conditions of the LIBS setup used here, the minimum surface damage for single-pulse LIBS results in a crater ~ 20 μm in diameter with a depth exceeding 200 nm.

Recall that for DP-LIBS, the threshold pump laser fluence for detection of Ni, Al and Cr was 1.12 J/cm^2, while Al and Cr were detected down to a laser fluence

of 0.49 J/cm^2. Figure 6.2.10 shows that ablation craters produced at a laser fluence of 1.12 J/cm^2 had a width of around 15 μm and a depth of 54 nm, while the depth of the of a damage crater produced at a laser fluence of 0.49 J/cm^2 had a width of around 10 μm and a maximum depth of 33 nm. This suggests that with DP-LIBS, the minimum surface damage for detection of Ni, Al, and Cr in the acquired LIBS spectrum resulted in a damage crater of width 10 – 15 μm and depth between 33 – 54 nm. Thus the DP-LIBS technique minimizes the surface damage by allowing LIBS analysis at lower pump laser fluences, reducing the diameter and depth of damage craters by 25 – 50 % and 75 – 80 % respectively, such that overall material removal was reduced substantially.

For the results discussed above, the edge of the probe pulse was located at a fixed height of $\Delta h = 30 \pm 2.5$ μm above the sample surface and it arrived at the sample surface with a fixed time delay of $\Delta t = 10.36$ ns after the ablation event was initiated by the pump pulse. In order for the probe pulse to ionize the ablated material, it had to first traverse the distance between the sample surface and the probe pulse Δh. By varying the pump-probe delay Δt over the range from 0 – 10.36 ns while keeping the probe height fixed at $\Delta h = 30 \pm 2.5$ μm, the velocity v, of the ablated material was ascertained by determining the time delay Δt_0 at which the signal enhancement was initially observed, with $v = \Delta h/\Delta t_0$. The raw LIBS signal at the characteristic wavelength for Al (396.152 nm) is plotted as a function of the time delay Δt in Figure 6.2.11 a) for three pump laser fluences, 3.1, 5.2, and 10.1 J/cm^2, while Figure 6.2.11 b) shows a semi-log plot of the LIBS signal as a function of time delay for the pump-laser fluence of 5.2 J/cm^2.

The time delay Δt_0 at which significant signal enhancement was first observed was found to depend on the pump laser fluence, ranging from Δt_0(3.1 J/cm^2) = 6.35 ± 0.67 ns, to t_0(10.1 J/cm^2) = 3.68 ± 0.67 ns, yielding average material velocities of 4720 ± 560 m/s to 9970 ± 1820 m/s respectively. The average material velocity is presented in Figure 5.2.12, along with the average velocity of the shock front measured directly from side view images. The average shock velocity is shown to have a similar trend but greater magnitude than velocity predicted by dual-pulse LIBS (1.6 – 2.4 times as great with increasing fluence).

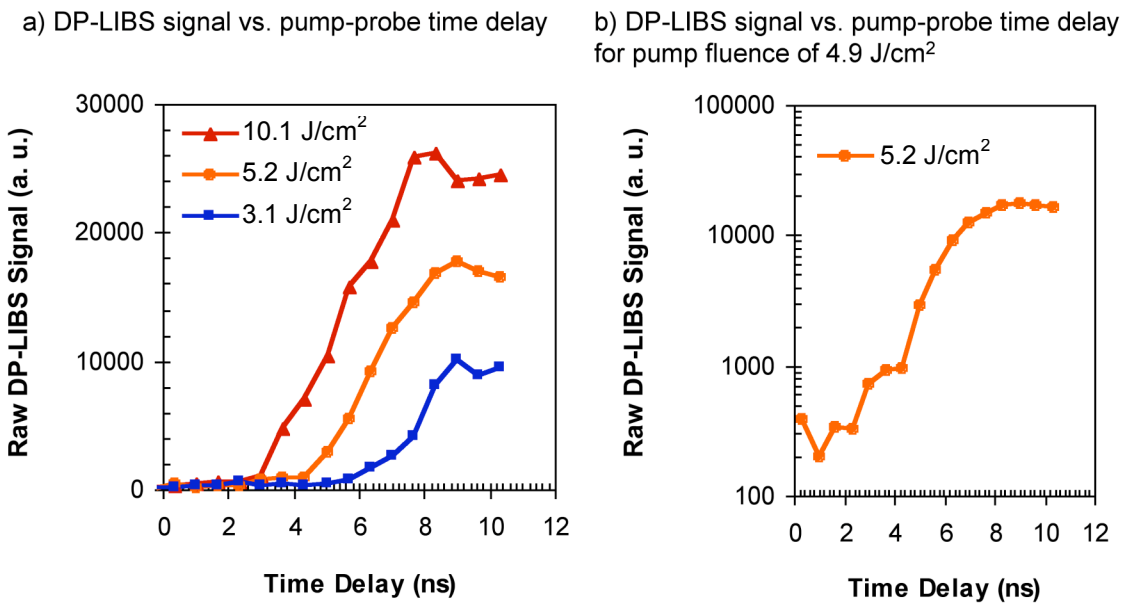

Figure 6.2.11 a) DP-LIBS signal integrated for 10 laser shots at characteristic of Al (396.42425 nm) for three laser fluences shown. Probe pulse was delivered orthogonally to the pump pulse at a height of 30.0 ± 2.5 μm with respect to the sample surface. Major signal increase was observed at time delays of Δt_0(3.1 J/cm^2) = 6.35 ± 0.67 ns, Δt_0(5.2 J/cm^2) = 5.01 ± 0.67 ns, and Δt_0(10.1 J/cm^2) = 3.68 ± 0.67 ns. b) Semi-log plot of time-resolved DP-LIBS signal for a pump-pulse laser fluence of 5.2 J/cm^2 showing presence of two phases of signal increase, the first begins at Δt_1(5.2 J/cm^2) = 3.01 ± 0.67 ns and Δt_2(5.2 J/cm^2) = 5.01 ± 0.67 ns.

The ablated material velocity clearly decreases with decreasing laser fluence. This indicates that longer pump-probe time delays may have increased the sensitivity of DP-LIBS by allowing the probe pulse to ionize the slower moving material that accompanies fs laser ablation at pump-pulse laser fluences near the ablation threshold.

A closer examination of the dual pulse LIBS signal (see Figure 6.2.11 b)) for a pump laser fluence of 5.2 J/cm^2 revealed that dual-pulse LIBS signal enhancement occurred in two stages as a function of time delay, with a subtle increase in signal (~ 100 % increase at Δt_1(5.2 J/cm^2) = 3.01 ± 0.67 ns) followed by a much larger increase in signal (~ 1000 % Δt_1(5.2 J/cm^2) = 5.01 ± 0.67 ns). This two stage signal enhancement as a function of time delay was consistent with a jetting phenomenon that was observed to accompany fs laser ablation of the CMSX-4 superalloy in side-view shadowgraphic imaging experiments discussed in Chapter 6.2.1. The first stage of signal enhancement occurs when the small amount of material leading the shock front enters into the focal volume

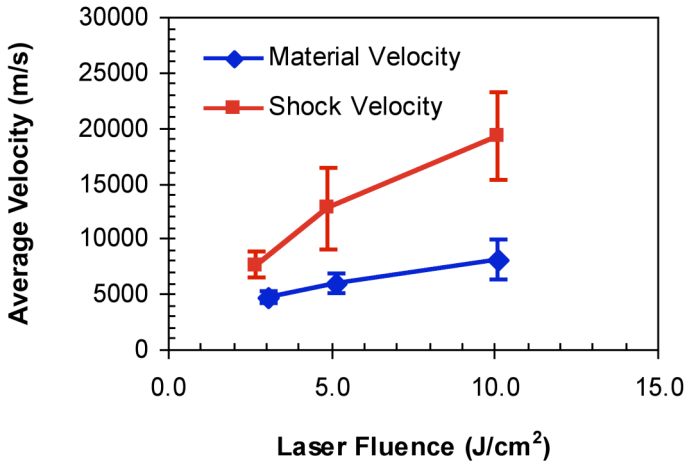

Figure 6.2.12 Average velocity of ablated material (from time-resolved DP-LIBS) and shock front (from time-resolved side-view images) as a function of pump-pulse laser fluence.

of the probe pulse, the leading edge of which is located at $\Delta h = 30 \pm 2.5$ μm above the sample surface. The second stage of signal enhancement occurs when the bulk of the ablated material arrives at the focal volume of the probe pulse. A schematic illustrating the jetting phenomenon and how it relates to DP-LIBS is presented in Figure 6.2.13.

Measurements of the shock height from side-view images of fs laser ablation at a laser fluence of 4.9 J/cm^2 indicate that the shock front (which is presumed to be lead by jetting material) arrived at a height of 30 μm above the sample surface at a time-offset corrected time delay of 2.66 – 3.19 ns (see Figure 6.2.3 a)), which compares favorably with Δt_1(5.2 J/cm^2) = 3.01 ± 0.67 ns inferred from time-resolved dual-pulse LIBS. Similarly, for a laser fluence of 10.1 J/cm^2, time resolved DP-LIBS measurements indicated that the first stage of signal enhancement began at 1.01 ± 0.67 ns (not shown in Figure 6.2.11), while the second stage began at 3.68 ± 0.67 ns. From time resolved side-view images at a laser fluence of 10.1 J/cm^2, the shock front arrived at a height of 30 μm at a time delay of 1.96 – 2.41 ns after the onset of ablation, again similar with dual pulse LIBS measurements. Two stages of signal enhancement were not clearly identified in the dual-pulse LIBS data collected at a pump laser fluence of 3.1 J/cm^2, which may be because the jetting material and bulk ablated material did not have time to sufficiently separate by the time they reached the height of the

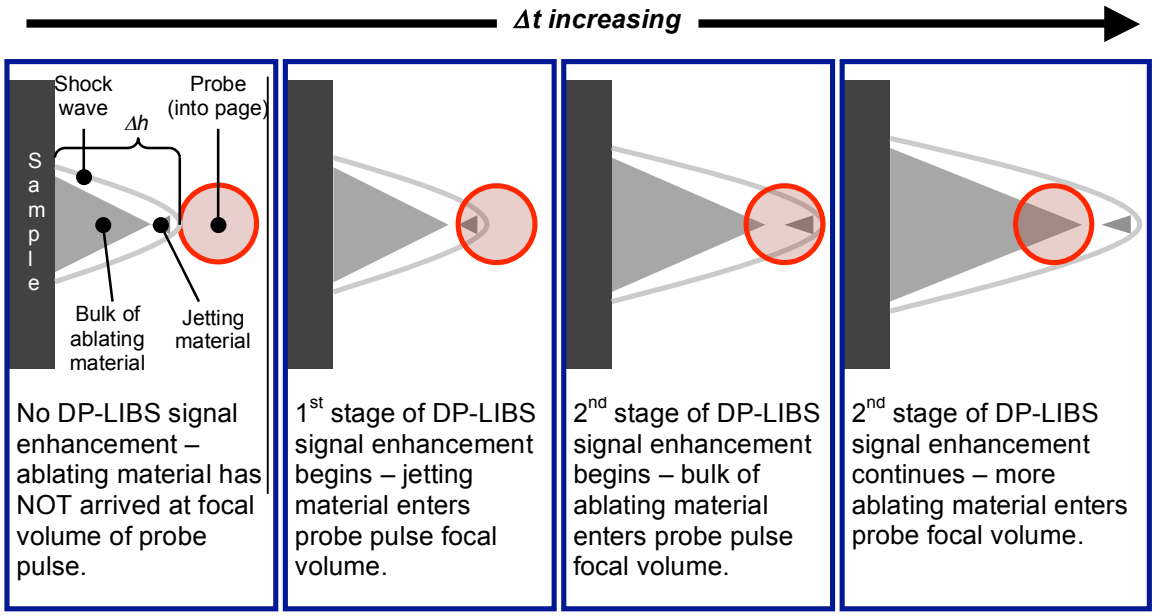

Figure 6.2.13 Schematic showing proposed mechanism of two-stage signal enhancement of time-resolved DP-LIBS measurements. The time delay Δt between the pump and probe increases to the right. The pump pulse (not shown) is incident from the right, while the probe pulse is directed into the page. The probe height Δh is indicated in the left most figure and is static for all

probe pulse. Furthermore, the evidence for the two phase DP-LIBS signal enhancement is admittedly limited, and should be followed by more detailed studies employing shorter time intervals between measurements and more pump-pulse laser fluences. The jetting phenomenon will be addressed further in the next section where FLASH code hydrodynamics simulations of the fs laser ablation of the CMSX-4 superalloy are presented.

In summary, fs laser based, orthogonal, DP-LIBS was used to reduce the surface damage associated with the LIBS spectroscopy technique performed on the Ni-based superalloy CMSX-4. Using the experimental setup presented here (see Chapter 3.3) the threshold for single-pulse LIBS was found to be 10.1 J/cm^2, while the threshold for dual-pulse LIBS was determined to be 1.12 J/cm^2 for detection of Ni, Al, and Cr in the acquired LIBS spectra. By decreasing the pump-laser fluence required for LIBS analysis, the corresponding surface damage decreased as well, with crater depths at the threshold for detection decreasing from 212 nm for single-pulse LIBS to 54 nm at the threshold for dual-pulse LIBS. Experiments using time-resolved dual-pulse LIBS provided a measure of the

average ablated material velocity, ranging from 4720 ± 560 m/s to 9970 ± 1820 m/s for pump laser fluences ranging from 3.1 – 10.1 J/cm^2. Further analysis of the time-resolved data verified the presence of the jetting phenomenon that was proposed to accompany fs laser induced ablation and material removal in Chapter 6.2.1. Future work may include finer resolution for time-resolved DP-LIBS in order to more accurately address the jetting phenomenon, and pursuit of DP-LIBS on superalloy substrates coated with thermal barrier coatings [268-270] in order to address the difficulties with application of the DP-LIBS technique on rougher and potentially non-flat surfaces.

6.2.3 Two-dimensional FLASH simulation of femtosecond laser ablation of the Ni-based superalloy CMSX-4.

As presented in Chapter 6.2.1, the dynamics of single pulse fs laser ablation of the CMSX-4 superalloy were studied with side-view shadowgraphic pump-probe imaging. In this section, the ablation event is simulated with a combination of 1D HYADES [211] and 2D FLASH hydrodynamic codes [219]. For background information on HYADES and FLASH, please see Chapters 2.4.3 and 3.7.3. This work was performed in collaboration with Musumi Das and Katsuyo S. Thornton, who provided the simulations and background information on the FLASH and HYADES codes. The 1D HYADES simulation was performed to determine the density and temperature as a function of material depth in the CMSX-4 superalloy at a time of 1 picosecond (ps) following absorption of the incident laser energy. The results from the HYADES simulation were then used as the initial conditions for the 2D-FLASH simulations. The simulated results were found to correspond very well with the direct observations made with the side-view, pump-probe imaging technique, verifying the presence of the jetting phenomenon which was observed to accompany fs laser induced material removal in side-view shadowgraphic images.

The experimental details and results from pump-probe side-view imaging of the CMSX-4 Ni-based superalloy are presented in Chapters 3.7.2 and 6.2.1 above. The simulated results assumed an incident pump pulse laser fluence of

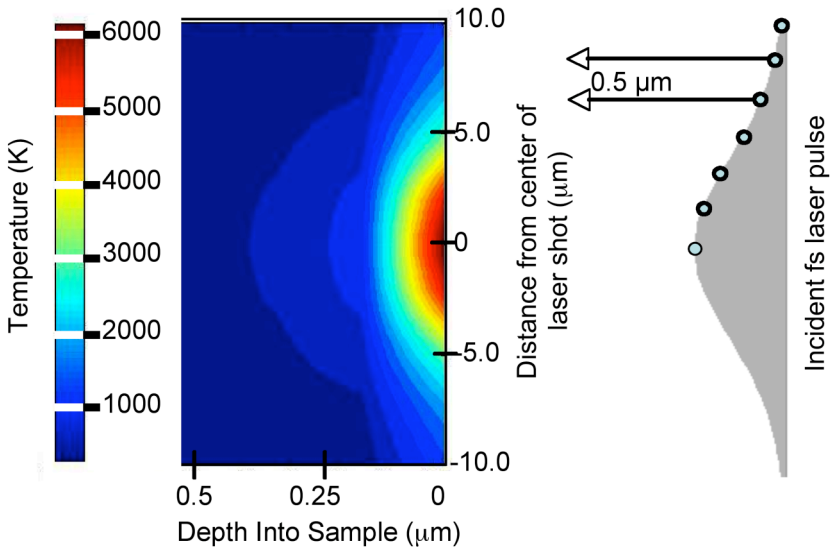

Figure 6.2.14 Laser beam of Gaussian spatial profile is incident on CMSX-4 (right) and temperature contour plot as a function of material depth after 1 picosecond from HYADES simulation (left).

10.1 J/cm^2 was directed at normal incidence onto the sample surface. The simulations further assumed that the sample consisted of a 2D slab of material 3.5 μm in depth by 20 μm in width. This sample geometry and size were chosen to reduce unphysical expansion of material located far away from the region initially excited by the laser, a non-physical feature observed in 2D-FLASH simulations when a semi-infinite slab of material was considered. This extraneous material expansion is addressed later in more detail.

In addition to the reduction in laser fluence imposed by the 2D geometry (i.e. the simulation takes a strip of energy absorption across the center of the focused laser spot), the optical reflectivity of the CMSX-4 superalloy was taken to be 95 %, such that only 5 % of the incident laser fluence (or a peak laser fluence of 0.5 J/cm^2) was input into the 1D HYADES simulation with a Gaussian beam profile. At the laser wavelength of 780 nm, the Fresnel intensity reflection coefficients of Ni and Al are 0.679 and 0.8794 respectively [233]. Furthermore, a rapid rise in reflectivity during the laser-pulse interaction with the material surface due to the generation of a dense electron-hole plasma was expected to further increase the overall reflectivity [4, 271]. The local energy deposition into the slab of material

was then determined by calculating the local laser fluence *F(r)* on the incident Gaussian beam profile given by:

$$F(r) = F_{0,abs} e^{\left(-2r^2/w_0^2\right)} \quad (6.2.5)$$

where $F_{0,abs}$ = 0.5 J/cm^2 is the peak *absorbed* laser fluence, and w_0 is the incident beam radius, $2w_0 = 19 \pm 0.5$ μm (for comparison with pump-probe imaging). Figure 6.2.14 shows the contour plot of the temperature within the material slab at a time of 1 ps following arrival of the incident fs laser pulse obtained from the 1D-HYADES simulation. This temperature profile (and corresponding density profile, not shown) was input as initial conditions into the 2D-FLASH simulation.

The 2D-FLASH simulation placed the 3.5 μm by 20 μm slab into a 150 μm square cell that was otherwise filled with air. Snapshot images from the 2D FLASH simulations of the single pulse fs laser ablation of the CMSX-4 superalloy at an incident laser fluence of 10.1 J/cm^2 are presented in Figure 6.2.15 alongside corresponding side-view shadowgraphic images. The simulations indicate that a shock or blast wave propagates in the air in front of the sample, surrounding a higher density core of the ablation plume. The shape and time evolution of the simulated ablation plume are very similar the direct observations made with pump-probe imaging. The jetting phenomenon discussed in Chapters 6.2.1 and 6.2.2 is very apparent in the simulated results. A small amount of material appears to separate from the rest of the ablation plume, leading the shock wave front as it moves away from the sample. In the simulated and collected images taken at around 7.1 ns, and 10.3 ns, the jetted material has separated into an isolated feature (see Figure 6.2.15). This jetting phenomenon is consistent with the time-resolved dual-pulse LIBS results discussed in Chapter 6.2.2, in which two stages of LIBS signal enhancement were observed as a function of the time delay between the pump and probe pulse. Note that the jetted material has a relatively smaller density then the bulk of the ablating material behind it, consistent with the modest increase in signal during the first stage of time-resolved DP-LIBS signal enhancement. High intensity nanosecond laser ablation of thin Ti foils was found to produce similar jetting phenomenon

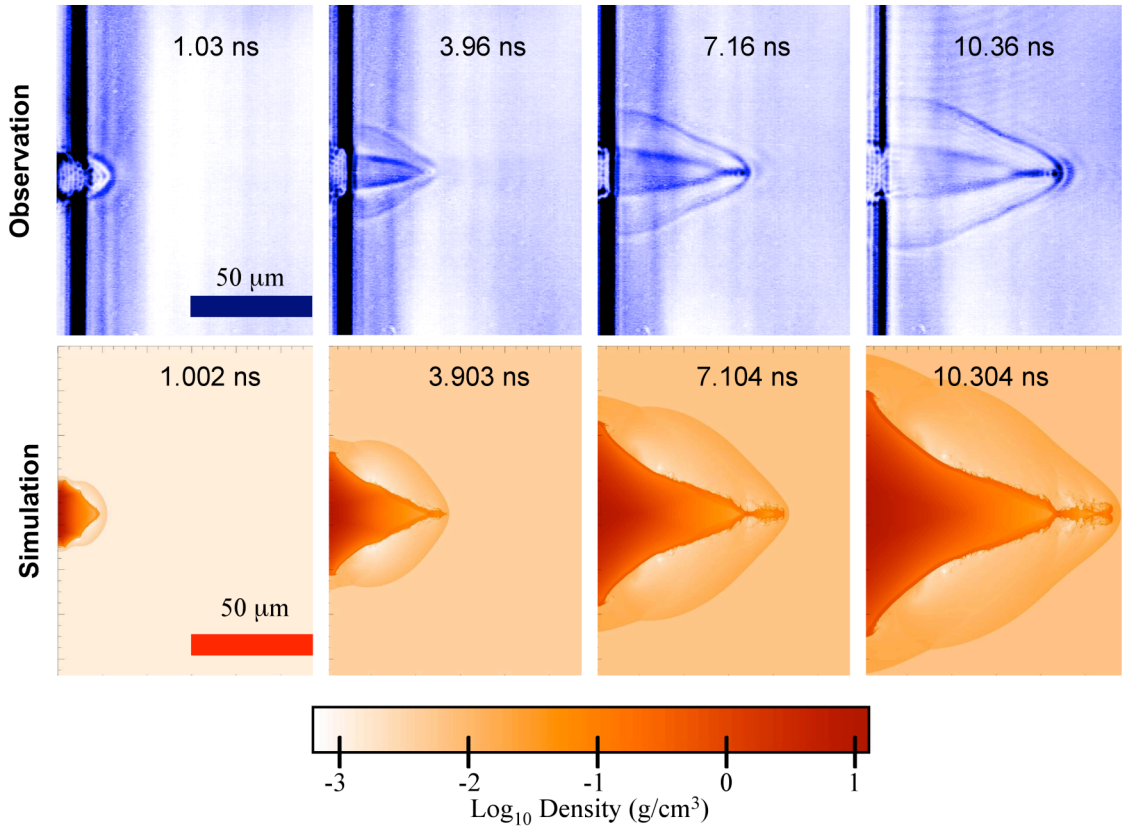

Figure 6.2.15 Observation (top row) and 2D FLASH simulation (bottom row) of fs laser ablation of CMSX-4 superalloy at a laser fluence of 10.1 J/cm^2. Time delays of observation and simulation with respect to arrival of laser pulse at sample surface are shown in each image. The scale is the same for observation and simulation, and scale bars at in the left-most images apply to all

[15], and the phenomenon may be related to so-called “nano-jet” formation in thin Au films [142, 272, 273].

Two particular differences were identified between the direct observations made with pump-probe imaging, and the simulated results made with the combination of HYADES and FLASH codes. First, the material expanded in the lateral direction much more dramatically in the 2D-FLASH simulations than in the direct observations made with pump-probe imaging. Furthermore, if a semi-infinite slab 150 μm in width was used for the material in the simulation as opposed to a slab 3.5 μm in depth by 20 μm in width, significant vertical expansion of material far outside the initial sample region energized by the laser pulse was observed. This exaggerated expansion was attributed to a lack of a model for material strength within the FLASH code. For a “real” sample, the

material outside the region excited by the laser pulse is constrained by the bonds present in the relatively cool bulk material, and no such bonding is included in the FLASH simulation. We partially defeated this shortcoming in the FLASH code by restricting the material within the 2D-FLASH simulation cell to only that which showed significant temperature variations after 1 ps in the 1D-HYADES simulation (a slab 3.5 μm in depth by 20 μm in width). Additionally, the FLASH code assumes an ideal gas equation of state module for the material evolution with a specific heat ratio of $\gamma = 5/3$. Recall that for the analysis applied to the ablation shock wave dynamics in Chapter 6.2.1, a specific heat ratio of $\gamma = 1.4$ was used. The value of γ should be reduced from 5/3 under the assumption that the ablating material in the fluid state can be represented by a polytropic gas [229]. It was found that the qualitative nature of the ablation plume in the 2D-FLASH simulation was consistent and comparable with experimental observation down to $\gamma = 1.4$, however deviations were observed for $\gamma < 1.4$.

The second difference between the simulated and observed ablation event was a greater overall expansion of the simulated ablation plume relative to the expansion observed in the side-view shadowgraphic images as a function of time. It is proposed that constraining the FLASH simulation to only two dimensions contributed to the exaggerated expansion with respect to the observations in which the expansion was allowed to proceed in three dimensions. The absorbed laser fluence which was approximated at 0.5 J/cm^2 (assuming a net surface reflectivity of 95 %) may have also been too large, resulting in higher initial temperatures from the HYADES simulation and thus greater energy for the ablating material. A full 3D-FLASH simulation of the fs laser ablation event may provide a better quantitative match with the expansion observed in the time-resolved side-view shadowgraphic images. Future work may also employ time resolved pump-probe reflectivity measurements of the surface of the Ni-based superalloy CMSX-4 [108-110] to better determine the reflectivity under the conditions of intense fs laser irradiation.

There is also considerable interest in understanding what happens inside the bulk material beneath the ablation crater, specifically in identifying sources of

collateral damage and heat affected zones [25, 28, 29, 115]. While providing an excellent picture of what happens during fs laser ablation event in the air in front of the sample surface, 2D-FLASH is not suited for analysis within the bulk. However the 1D HYADES simulations used to provide initial conditions could easily be extended to later times to address these issues and should be the topic of future work.

In summary, the dynamics of single-pulse fs laser ablation of the Ni-based superalloy CMSX-4 were simulated using 2D-FLASH code with initial conditions provided by a 1D-HYADES simulation. The simulations were performed using an incident laser fluence of 10.1 J/cm^2 and an absorbed fluence of 0.5 J/cm^2, implying a surface reflectivity of approximately 95 % for the Ni-based superalloy CMSX-4 under fs laser irradiation. The simulated results were very similar to in-situ observations of the fs laser ablation made with time-resolved pump-probe imaging. The 2D-FLASH simulation clarified the sources of contrast in the side-view pump-probe images, revealing the presence of a jetting phenomenon in which a small amount of ablating material separates from the rest of the ablation plume and leads the blast wave away the sample surface. This jetting may be the result of a local decrease in the viscosity of the molten metal which produces a low density region of material that is free to jet away from the surface. Similar pump-probe imaging experiments and simulations of fs laser ablation of glass may provide an interesting contrast to the experiments performed here due to the difference in the temperature dependence of the viscosity of glasses and metals [ref]. The 2D FLASH simulation was found to produce some unphysical results due to the lack of a material strength model, resulting in the artificial expansion of all CMSX-4 superalloy material within the simulation cell. Future work will include simulation efforts to investigate the dynamic effects of fs laser ablation within the material being ablated.

Chapter 7

Future Work

7.0 Future work

The experiments and results discussed in this dissertation provide insight into the fundamental physics near threshold fs laser ablation of single crystal silicon with oxide films and the Ni-based superalloy CMSX-4. Furthermore, practical applications were demonstrated including a novel technique for producing fluidic channels, and a quasi-nondestructive dual-pulse laser induced breakdown spectroscopy technique for minimally invasive surface evaluation of materials. Interpretation of these fundamental and practical results suggested several opportunities for future work, which are discussed in the following section.

7.1 Future work concerning the fs laser ablation threshold

In this thesis, fs laser ablation studies were performed to determine the role of oxide films on the ablation threshold of silicon (see Chapter 4.1). Some of these experiments were performed under UHV conditions, where the presence or absence of the native oxide was controlled with conventional semiconductor processing techniques (see Chapter 3.4). Due to the available beam delivery options into the UHV chamber, only grazing incidence ablation thresholds were determined with p-polarized laser pulses. This initial work could be extended by considering the effect of other laser conditions on the ablation threshold of silicon with and without the native oxide. Other angles of laser incidence and laser polarizations for studies in UHV should be considered, including normal incidence where the current understanding put forth in this dissertation predicts that the presence of the native oxide should decrease the ablation threshold of silicon relative to atomically clean silicon (see Chapters 4.1 and 4.2). Along these

lines, ablation threshold experiments could be repeated for silicon with thermally grown oxide films at a different fs laser wavelength (such as 388 nm or 1053 nm) than used in this study (780 nm), which would change the reflective properties of the silicon substrate by changing the degree of multiple beam interference in the thermal oxide film (see Appendix 2). Experiments such as these would demonstrate considerable support for the hypothesis that oxide films influence ablation threshold by simply changing the reflectivity of the silicon surface.

In order to further address the influence of the optical properties on the fs laser ablation threshold, the ablation threshold of Si(100) should be determined in the presence of different thin films including transparent polymers or other transparent oxides. Ideally these materials would have real refractive indices or thicknesses' different than the oxide films presented here, so that the ablation threshold dependence on such properties could be properly established. Investigation of the fs laser ablation morphology could be incorporated into these threshold studies, where the role of thin film mechanics on the ablation morphology could be addressed. Of particular interest is the production of blister or buckling features in other materials (including opaque films), and identifying if blisters could be produced in transparent films exhibiting tensile stress.

Finally, the fs laser ablation threshold should be studied as a function of surface roughness on the Ni-based superalloy CMSX-4. A rather straightforward study would involve polishing several samples to different final states of roughness, performing ablation threshold experiments, and then characterizing the surface of each sample via AFM. Reports in the literature suggest that laser induced periodic surface structures can dramatically increase the optical absorption of a metal surface [274, 275], however the role of the initial surface roughness on the ablation threshold have not been reported. Of similar interest would be the fs laser ablation threshold as a function of crystal grain size on polycrystalline Cu or Fe, for which some preliminary data has been collected by Brad Thomas, an undergraduate researcher in the Yalisove Lab in 2005.

7.2 Future work related to fs laser ablation morphologies

A range of additional experiments should be performed to investigate the fundamental physics and associated applications of fs laser induced blistering of thermally grown and PECVD oxide films on silicon. Regarding the fundamental, a careful study of the mechanics of thin film buckling in 1200 nm thermal oxide films under multiple-pulse irradiation on the same blister feature should be performed in order to identify if buckling is influenced by dose dependent, thermally induced mechanical changes to the oxide film. Furthermore, the theory addressing buckling under the presence of outward pressure should be extended to include time-dependent pressures on the ns time scale that accompany fs laser ablation [146](see Chapter 6.1.2). Analysis of fs laser induced buckling mechanics should explore the connection between the energy release associated with ablation shock waves and film buckling, particularly the observation of buckling at smaller delamination widths than would be expected from the relaxation of intrinsic film stress alone (see Chapters 5.2.5 and 6.1.2).

Applications of fs laser induced blistering of oxide films from silicon (and other films yet to be exploted) present many opportunities for future work (see Chapter 5.2.4). The simple fluidic device demonstrated in this thesis could be enhanced by adding the metal electrodes required for electrophoresis to the surface of the chip. Methods for defeating the cavitation and local boiling that limit electrophoretic flow should also be investigated. Such methods might include partially filling the channels with a polymer to provide a barrier between the silicon and the fluid. The incorporation of sensors or other fluid control mechanisms to such a chip could be explored in collaboration with several research groups at the University of Michigan [257, 276, 277], and would be a significant step toward commercializing the technique.

7.3 Future work related to fs laser ablation dynamics and laser induced breakdown spectroscopy

The dynamics of fs laser ablation were studied in-situ with fs laser based pump-probe microscopy techniques (see Chapters 6.1.1 – 6.1.3, and Chapter 6.2.1) and with dual-pulse laser induced breakdown spectroscopy (DP-LIBS, see

Chapters 6.1.4 and 6.2.2). Understanding of the mechanisms of fs laser ablation would be enhanced by considering a larger range of pump-laser fluences in front-view imaging experiments. As shown and discussed in Chapter 6.1.1, front-view images of fs laser ablation of silicon with thermal oxide films displayed a phenomenon known as Newton's rings, the presence of which has been attributed to a near threshold ablation mechanism in which a well-defined, thin layer of molten material is ejected from the surface. According to the model developed in Chapter 6.1.3, the gap material between the ejected layer of molten material and the underlying molten substrate can be treated as a semi-dense plasma (10^{21} cm^{-3}). At higher laser fluences, it is expected that the density of this plasma would increase to the point that it was no longer transparent to the incident probe laser pulse [230], such that the Newton's rings would no longer appear in front-view pump-probe images. Therefore, pursuit of higher pump-pulse laser fluences (> 5 J/cm^2) in front-view imaging experiments, along with corresponding side-view images at the same laser fluence, would be useful in verifying the model presented in Chapter 6.1.3. Furthermore, front view images of ablation of silicon with 1200 nm thermal oxide may provide insight into the formation mechanism high fluence morphologies presented in Figure 5.2.13, where laser induced modifications to the oxide film may significantly alter the observed dynamics. Such efforts would benefit understanding of the role of interfaces on fs laser ablation.

Side-view shadowgraphic imaging should also be performed on very thin ($\leq$ 100 μm) metallic samples such as the Ni-based superalloy CMSX-4 or similar materials such as thin Al or Ni. Recall that we assumed Newton's third law applies, such that the shock wave in air that is produced during the ablation event must be accompanied by an equal and opposite shock wave that propagates into the material (see Chapter 6.2.1). By performing fs laser ablation on a thin sample, side-view shadowgraphic images obtained at sufficiently long delays may show the emergence of a shock wave on the back side of the sample associated with the ablation event. Careful analysis of the dynamics of the backside shock wave in comparison to the air shock wave propagating in front of

the sample may provide insight into the shock induced defects observed to accompany high fluence fs laser ablation [267]. An interferometric technique known as VISAR may also be of interest, as it could provide quantitative information on the shock wave reaching the back surface of a thin sample [278]. 1D HYADES Simulations of the fs laser induced shock within a bulk material as a function of laser fluence should also be pursued to compliment any backside pump-probe imaging techniques.

Finally, the DP-LIBS experiments performed on the CMSX-4 superalloy presented in this dissertation should be extended to samples which include thermal barrier coatings (TBC). The practicality of the DP-LIBS technique should be addressed on materials with rough or rounded surfaces, as “real world” applications of DP-LIBS will inevitably involve more complicated beam delivery and spectra collection. Longer pump-probe time delays (exceeding the maximum of 10.36 ns used here) should be used. Longer delays may provide for DP-LIBS signal enhancement at lower pump laser fluences by giving the slower moving ablating material enough time to reach the height of the probe. Future work should further address the role of interfaces fs laser ablation dynamics using DP-LIBS techniques. Samples with buried interfaces or dissimilar layers of materials at different depths could be prepared via sputtering, and time-resolved DP-LIBS experiments could be performed on these samples to identify if the ablation event couples to interface allowing the buried material to be removed.

While revealing many fundamental and practical issues of the fs laser/material interaction, the work presented here has also introduced new questions related to ablation thresholds, morphologies, and dynamics. It is the hope of the author that the experimental techniques and preliminary results presented in this dissertation will serve as a guide to future students, providing them with a fruitful and rewarding research experience.

Chapter 8

Summary and Conclusions

8.0 Summary and Conclusions

This dissertation explores near threshold fs laser ablation of materials by examining the ablation thresholds, ablation morphologies, and ablation dynamics of single crystal silicon with oxide films, and the Ni-based superalloy CMSX-4. Fundamental physical mechanisms of fs laser ablation were developed, revealing several potentially useful results. The following sections summarize these results and present conclusions in the context of the goals of this dissertation presented in Chapter 1.1.

8.1 Femtosecond laser ablation thresholds

The influence of oxide films on fs laser ablation of silicon were studied by the measurement of ablation thresholds. Experiments performed in UHV conditions at grazing laser incidence revealed that the presence of a native oxide (~ 1.5 – 3 nm) increased the ablation threshold of silicon by ~ 39 % relative to atomically silicon (Chapter 4.1.1). The ablation threshold determined for Si(100) with a native oxide at grazing incidence in air revealed that the ablation threshold for s-polarized light was ~ 115 ± 30 % greater than the ablation threshold for p-polarized light (see Chapter 4.1.2). These changes in the ablation threshold were attributed to changes in the reflectivity of the silicon surface with the presence or absence of the native oxide, and were found to be correlated with relative thresholds calculated from the Fresnel intensity transmission coefficients. These results were extended by considering the ablation threshold of Si(100) with thicker, thermally grown oxide films. Once again the trend in the measured ablation threshold as a function of the oxide film thickness was dictated by the

optical properties of the silicon substrate, in this case due to changes in the reflectivity of the crystalline silicon from multiple reflections within the oxide films (see Chapter 4.2.1 and 4.2.2). These results suggested that the role of oxide films on fs laser ablation of silicon was largely optical in origin, changing the optical reflectively of the silicon surface. Furthermore, these results reveal that in spite of the extreme intensities and ultra short timescales of fs laser ablation, the linear optical characteristics of a surface can be used to predict relative fs laser ablation thresholds.

Fs laser ablation studies performed on the Ni-based superalloy CMSX-4 provided an example of the variation in measured ablation thresholds that can occur, even under similar experimental conditions. In this work, a single shot fs laser ablation threshold of 0.38 ± 0.02 J/cm^2 is found, while in other works values of 0.3 ± 0.03 J/cm^2 [116] and 0.332 ± 0.014 J/cm^2 [115] are reported (see Chapter 4.3.1). This indicates that in addition to the error provided by fitting routines, a certain systematic error is involved with any ablation threshold experiment. As such, a more accurate statement of the fs laser ablation threshold of the Ni-based superalloy CMSX-4 is 0.35 ± 0.05 J/cm^2. These examples of ablation threshold variation, including those presented for silicon [52], demonstrate that while fs laser ablation thresholds are sharp and deterministic [33], reproducibility of these thresholds from day to day, or from lab to lab is difficult to attain, emphasizing the need for accurate statements of measurement error.

8.2 Fs laser ablation morphologies

The role of interfaces between dissimilar materials was highlighted through detailed fs laser ablation morphology investigations on silicon with thin oxide films. First the presence of the native oxide of silicon was observed to influence the multiple pulse ablation morphology by introducing laser fluence dependent modification mechanisms which removed energy from the incident laser pulse inhibiting ablation of the silicon substrate (see Chapter 5.1). At appropriate laser fluences, ablation features produced under UHV conditions on Si(100) substrates

with a native oxide exhibited a region of pitted ablation features which surrounded a relatively undamaged region, which in turn surrounded a central ablation region (see Figure 5.1.1). This pitted ablation region was never observed on atomically clean Si(100) samples machined under similar conditions. The presence of the undamaged region was attributed to a fs laser induced modification within the native oxide which effectively reduced the local laser fluence arriving at the silicon substrate thereby impeding ablation (see Chapter 5.1.2). This modification to the native oxide was proposed to have a sharp fluence threshold, such that where the local laser fluence dropped below this threshold the modification did not occur. As a result, the incident laser light passed through the oxide unperturbed, arriving at the interface with the silicon substrate where ablation occurred producing the pitted region of ablation. These results revealed that under appropriate laser fluence conditions, ablation proceeds at the interface between native oxide film and the silicon substrate without direct ablation of the oxide. Although limited in extent, the pitted region of ablation reduced the quality of ablation features produced with multiple laser pulses at grazing laser incidence.

The fs laser ablation morphology produced on Si(100) with thermally grown and PECVD oxides (20 nm – 1200 nm) exposed new phenomena not observed with the native oxide (see Chapter 5.2) further demonstrating the role of the substrate/film interface on fs laser ablation. For laser fluences exceeding 0.6 – 0.7 J/cm^2, the oxide film was ablated away from the substrate, producing a crater with depth approximately equal to the thickness of the oxide film. The cleanest oxide removal (i.e. least amount of laser induced damage to the silicon substrate) was observed for non-normal laser incidence. These observations indicated that the incident fs laser pulse largely interacted with the material at the substrate film interface, where the incident laser energy was absorbed initiating ablation of material (Chapter 5.2.1). For laser fluences between 0.3 – 0.7 J/cm^2, an ablation morphology was produced in which the oxide film was delaminated from the silicon substrate but remained intact with the surrounding film, producing a void or blister between the film and the substrate (Chapter 5.2.2). The dimensions of

these blisters were analyzed with thin-film buckling mechanics, which indicated that the fs laser ablation event at the substrate/film interface contributed to blister formation by allowing for buckling of the oxide film at smaller delamination widths than would be expected from the relaxation of intrinsic compressive film stress alone (see Chapter 5.2.5).

It was also discovered that isolated blisters could be overlapped to form linear blister channels in 1200 nm thermal oxide and PECVD oxide films. Blister channels ranging in width from 17 – 300 μm were produced, ranging in height from 170 nm to greater than 15 μm (see Chapter 5.2.4). Linear blister channels with highly uniform cross sections were written with the laser at speeds of up to 1 cm/s. Channels produced with the fs laser direct write technique were used to produce a simple electrophorectic device, through which the propagation of charged nanospheres was observed with application of modest electric fields. Thin film buckling mechanics were used to characterize linear blister channels produced in 1200 nm thermally grown and PECVD oxides. These studies showed that the intrinsic compressive stress inferred from channel dimensions rapidly asymptotes to measured and reported values in the literature. Furthermore, upper bounds were placed on the interface toughness of the films through analysis of the energy release rate at the blister tip for the smallest blister channels [150], yielding interface toughness values of 0.15 J/m^2 and 0.58 J/m^2 for the 1200 nm thermally grown and PECVD oxide films respectively. These results provide a novel method of probing thin film and interfacial properties, and also demonstrate a near threshold fs laser ablation morphology that may have application in the fluidics community.

The fs laser ablation morphology produced on the Ni-based superalloy was observed to evolve as a function of the laser fluence [19, 20, 22, 80, 133-136]. Within the low fluence regime ($0.38\ J/cm^2 \leq F_0 \leq 6.3\ J/cm^2$), ablation morphologies were highly reproducible, with submicrometer roughness resembling the polished condition of the virgin surface (Chapter 5.3). In the high fluence ablation regime ($F_0 \geq 6.3\ J/cm^2$), the ablation morphology showed more variation from feature to feature, with considerable redeposition of ablation debris

surrounding a highly perturbed crater surface. The high fluence regime was also associated with a sudden increase in the ablated crater depth as a function of laser fluence, suggesting the onset of different ablation mechanism that both increases material removal and leaves a rougher ablation morphology on the micrometer scale [40-42]. Finally, distinction was made between the presence of apparently re-solidified molten material or melt-like morphology and the high fluence ablation regime. The melt-like morphology emerged at ~2.3 J/cm^2 and was not associated with a pronounced increase in the ablated crater roughness on the micrometer scale.

8.3 The dynamics of fs laser ablation

Fs laser ablation of silicon with oxide thin films was observed in-situ using pump-probe imaging techniques. The results of these studies verified and extended previously developed models for fs laser ablation, while revealing qualitative and quantitative differences in the ablation dynamics as a function of the oxide film thickness. Side-view images of fs laser ablation indicated that the ablated material velocity generally decreased with increasing oxide film thickness. One significant exception to this observation was the fact that at a pump-laser fluence of 4.6 J/cm^2, the velocity of the ablating material was found to be greater for silicon with 20 nm and 54 nm of thermal oxide when compared with silicon with only the native oxide. Furthermore, the shock wave front propagating in the air in front of the sample was distinctly separated from the material front for ablation of silicon with a native oxide, however the shock front and material front were observed to propagate together for several ns for silicon with 20 nm and 54 nm of thermal oxide. This suggests that the laser ablation proceeds at the substrate film interface where the ablation shock wave is generated due to the sudden thermal expansion of the surface. Additional analysis of the shock wave dynamics indicated that the shock wave lost energy upon traversing 300 nm and 1200 nm thermal oxide films, which was likely related to the manner in which the fs laser ablation event at the silicon/oxide interface participates in the ablation event (see Chapter 5.2.5)

Images of the ablation event obtained with the front-view imaging geometry showed the presence of a Newton's ring phenomenon observed by other groups [34-38] (Chapter 6.1). The presence of these Newton's rings was attributed to a near threshold fs laser ablation mechanism in which a thin liquid like layer is ejected from the surface of the material [34-38]. The rings were formed from interference between probe light reflected off the ejected liquid-like layer, and probe light reflected from the underlying molten substrate. In this work, an expression was developed to determine the ablated material height and ablated material velocity as a function of the Newton's rings which was dependent on the optical properties of the material undergoing ablation. Of particular interest was the real refractive index of the gap material separating the liquid-like layer from the underlying molten substrate. The novel approach employed in this dissertation was to calibrate the expression for the ablated material velocity obtained from the Newton's rings with a direct measure of the ablated material velocity obtained from side-view shadowgraphic images. Furthermore, by studying the dynamics as a function of oxide film thickness, a range of ablated material velocities were observed allowing the expression for the ablated material velocity from the Newton's rings to be calibrated across an order of magnitude range in ablated material velocities. This calibration indicated that the material separating the two interfaces responsible for the Newton's rings could be modeled as a semi-dense plasma (~10^{21} cm^{-3}) with a real refractive index of 0.9. Previous studies examining front-view pump-probe imaging of silicon at a laser fluence of 0.46 J/cm^2 suggest that the refractive index of the gap material must be greater than 2, proposing that the gap is filled with a mixture of plasma and liquid droplets [34, 35].

Side-view shadowgraphic imaging of fs laser ablation of the Ni-based superalloy CMSX-4 revealed a connection between observed ablation dynamics and the resulting ablation morphology. Similar experiments performed by other groups have explored a very limited range of laser fluence, and have not made mention of a connection between the ablation dynamics and morphology [41, 65, 72, 166]. By analyzing the energy release associated with the measured lateral

shock dynamics, two regimes of laser ablation were observed with the transition between the two regimes occurring for laser fluences between 4.9 J/cm^2 and 10.1 J/cm^2. This transition occurs at similar laser fluence as the sudden increase in the ablation rate as a function of laser fluence and the onset of the explosive high fluence ablation morphology, suggesting a connection between the early dynamics of fs laser ablation and the final condition of the surface. The side-view pump-probe images also showed that material removal was accompanied by a jetting phenomenon in which a small amount of ejected material is observed to drive the shock wave away from the sample surface. This presence of this jetting phenomenon was verified in 2D FLASH simulations of the ablation event, and may be related to a dramatic decrease in the viscosity of the material at the center of the ablation event where the local laser fluence and therefore surface temperature is the greatest.

Finally, an orthogonal dual-pulse laser induced breakdown spectroscopy technique (DP-LIBS) was employed to reduce the surface damage associated with this versatile spectroscopy technique. The DP-LIBS technique used here was specifically designed to exploit the near threshold fs laser ablation phenomenon. A plasma threshold exists for materials, such that for laser fluences below this threshold energetic plasma is not produced during the ablation event, however removal of material still occurs [15]. This effectively limits single-pulse LIBS to laser fluences exceeding this plasma threshold. As discussed with respect to pump-probe imaging [34, 35], near the threshold a thin liquid like layer is ejected from the surface. The goal of the DP-LIBS technique used here is to ablate this material after it has left the sample with a high intensity beam directed parallel to the sample surface, thereby producing the necessary plasma for LIBS analysis while limiting the surface damage by using near threshold laser fluences. The threshold laser fluence for single-pulse LIBS detection of Al, Ni, and Cr within the acquired spectra was determined to be 10.1 J/cm^2, while the threshold for DP-LIBS was determined to be 1.12 J/cm^2. This decrease in the threshold fluence for LIBS analysis correspondingly reduced the depth of ablation craters from around 200 nm for single pulse LIBS at 10.1 J/cm^2,

down to a depth of 54 nm for DP-LIBS at 1.12 J/cm^2. Furthermore, time-resolved DP-LIBS measurements revealed the presence of a two-stage signal enhancement that was correlated with the jetting phenomenon observed in simulations and in-situ pump-probe imaging.

In conclusion, the research presented in this dissertation employs a range of methods to study fs laser ablation of single crystal silicon and single-crystal Ni-based superalloy CMSX-4. The influence the naturally occurring native oxide of silicon on fs laser ablation thresholds and morphologies was determined, demonstrating the role that the oxide has on modifying the optical properties of the silicon surface. Careful study of fs laser ablation morphologies produced on silicon with thermally grown oxide films (20-1200 nm) revealed the importance of interfaces, while exposing a potentially useful near threshold ablation morphology with application to fluidics. The ablation dynamics of silicon with oxide films were characterized in-situ, where novel techniques were used to verify and improve models for near threshold fs laser ablation. Study of the dynamics of fs laser ablation of the Ni-based superalloy CMSX-4 indicated that the ablation dynamics within the first few nanoseconds are connected to the final ablation morphology. Finally, DP-LIBS experiments have extended this surface sensitive spectroscopy tool to laser fluences near the ablation threshold, significantly reducing the associated surface damage.

Appendices

Appendix 1

Placing the sample at the focus of the laser beam

Placing the sample surface at the focus of the laser beam is of critical importance in ablation threshold experiments and for optimized laser machining. The technique presented here utilizes the bright spark in air that is produced at the location focus due to laser induced ionization of the ambient air. Figure A1.1 presents a schematic of the technique for finding focus, which was developed for use with the CPA-2001 laser from Clark-MXR. This technique works best when the laser is operating at 1 kHz, which produces a brighter spark in the air than if the laser is operating at 125 Hz. If the experiment demands 125 Hz operation of the laser, perform the beam alignment and focusing first with the laser at 1 kHz, then reduce the repetition rate of the laser and proceed with your experiment. The focal position and beam alignment will not change when the repetition rate is changed.

The laser beam is typically brought to a focus using a plano-convex or achromatic lens of focal length less than or equal to 40 cm. Although exact conditions to produce the air spark were not determined, intensities sufficient to produce air breakdown were produced with full beam power (i.e. no filtering) for all lenses of focal length less than 40 cm at a repetition rate of 1 kHz. When initially observing the spark, make sure that the sample is not in the beam path to avoid unintentional damage to the surface. An audible sound will also be produced (high pitched, at a frequency of 1 kHz) if the breakdown is sufficiently strong. If you have trouble locating the spark, simply translate a card along the beam path after the focusing lens. The card will be aggressively ablated near the location of the beam focus. For long focal length lenses (> 20 cm) the spark will appear elongated, like a sliver or needle of white light. For shorter focal length

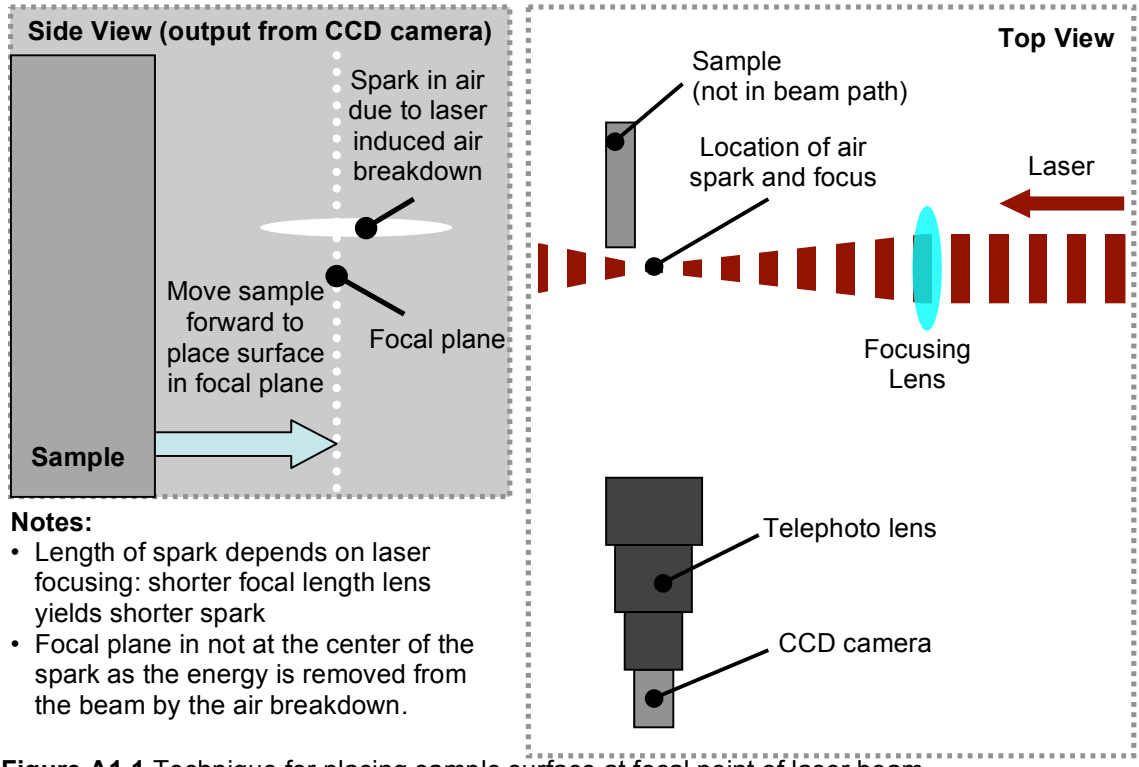

Figure A1.1 Technique for placing sample surface at focal point of laser beam.

lenses (< 10 cm) the spark will appear shorter, and more confined. Once the air ionization spark has been located, proceed with the rest of the focusing procedure.

A CCD camera with an attached telephoto zoom lens is placed such that it views the sample with maximum zoom in a direction parallel to the sample surface, perpendicular to the path of the beam (for normal incidence irradiation). The CCD camera is in turn connected to a television monitor so that the relative locations of the sample surface and the air spark are apparent to the researcher at all times. The sample is placed such that the focused beam (and corresponding air spark) is located between the sample and the CCD camera. If sufficient laser intensity conditions are met, a bright spark is produced in the air at the location of focus where the beam intensity exceeds the breakdown threshold of the air. As mentioned earlier, the physical length of the air spark was found to depend on the focal length of the lens, with longer air sparks produced with longer focal length lenses. The length of the air spark was roughly related to the confocal parameter (twice the Rayleigh range, z_R), given by [265]:

$$2z_R \approx \frac{\pi d_0^2}{2\lambda} \quad \text{(A1.1)}$$

where $d_0 = 2w_0$ is the Gaussian beam diameter and λ is the wavelength of the incident laser beam. Recall that the Gaussian beam radius w_0 is defined as the radius at which the local laser fluence has decreased to $(1/e^2)*F_0$ where F_0 is the peak laser fluence. The beam diameter d_0 can be related to the incident beam diameter D, and the focal length of the lens f, by the following [265]:

$$d_0 \approx \left(\frac{2f\lambda}{D}\right) \quad \text{(A1.2)}$$

This equation serves as a good approximation however, we have used alternative method (discussed in Chapter 3.3) to determine the beam waist from ablation threshold experiments [221].

The location of focus is thought to occur slightly *after* the center of the air spark with respect to the incident beam (away from the focusing lens). This is because the air breakdown event removes energy from the beam, such that the spark is not symmetric about the location of focus. Furthermore, the spark was found to shift down the beam path (away from the focusing lens) as the pulse energy was decreased via filtering, providing further evidence of this asymmetry. As such, the lowest laser intensity capable of producing the air spark was used to find focus. Due to the asymmetry of the air spark about the laser focus, the front surface of the sample is placed at a location approximately 2/3 the length down the spark from its start with respect to focusing lens (see Side View in Figure A1.1). At this point the sample is at focus, and the experiment can proceed.

When the focal length of the lens was less than 5 cm, it was difficult to determine this (somewhat arbitrary) distance of 2/3 down the length of the spark, as the spark had a very short length (less than 100 μm). This difficulty encouraged the use of long focal length lenses (focal length = 20 – 40 cm) for threshold studies as the location of focus was easier to determine. Longer focal length lenses also facilitate threshold measurements by producing larger features which are easier to measure accurately from OM images.

Appendix 2

Reflectivity of crystalline silicon with oxide films

This appendix presents the optical properties of a crystalline silicon surface with and without the presence of a surface oxide film of varying thickness. Furthermore, the expression for the ablating material height as a function of the number of Newton's rings present in front-view pump-probe microscopy images is developed.

In Section A2.1, the refractive indices of crystalline silicon and SiO_2 are presented for the relevant wavelengths and material conditions used in this study. In Section A2.2, the Fresnel intensity reflection and transmission coefficients for s- and p-polarized radiation directed at an angle of θ onto silicon with an oxide surface film will be discussed with applicability to Chapter 4.1 and 4.2. The intensity reflection coefficient incorporating the effect of multiple reflections is also addressed. For surface reflectivity under multiple reflections, the specific case of a thermal oxide film (20 nm – 1200 nm SiO_2) on a crystalline silicon substrate will be presented with applicability to Chapter 4.2. Finally in Section A2.3, the model used to connect the physical height of ablating materials with the Newton's Rings phenomenon is developed.

A2.1 Refractive indices of crystalline silicon and SiO_2

In general, the refractive index of a glass as a function of the wavelength of light, λ can be determined from the Sellmeier equation [279]:

$$n^2(\lambda) = 1 + \frac{B_1\lambda^2}{\lambda^2 - C_1} + \frac{B_2\lambda^2}{\lambda^2 - C_2} + \frac{B_3\lambda^2}{\lambda^2 - C_3} \qquad \text{(A2.1)}$$

where B_i and C_i are the Sellmeier coefficients, and λ is in μm. The Sellmeier coefficients are provided for fused silica (the material most similar to the oxide films used here) and BK7 glass in Table A2.1 below [279].

Glass	B_1	B_2	B_3	C_1	C_2	C_3
Fused Silica	6.962E-01	4.079E-01	8.975E-01	4.679E-03	1.351E-02	9.793E+01
BK7	1.040E+00	2.318E-01	1.010E+00	6.001E-03	2.002E-02	1.036E+02

Table A2.1 Sellemeier coefficients for fused silica and BK7 glass.

The first order Sellmeier coefficients as a function of oxide film thickness on silicon under various conditions have been determined by other groups, indicating that the refractive index of thin oxide films is typically greater than fused silica by a few percent [280]. Using the coefficients for fused silica provided in Table A2.1 above, the refractive index of the oxide films was calculated to be $n_{glass}(780\text{ nm}) = 1.4537$, and $n_{glass}(390\text{ nm}) = 1.4714$.

For crystalline silicon, it is appropriate to use the complex refractive index ($N(\lambda) = n(\lambda) + ik(\lambda)$) where $n(\lambda)$ is the real refractive index and $k(\lambda)$ is the extinction coefficient. Table A2.2 provides the room temperature real refractive index $n(\lambda)$, and the extinction coefficient $k(\lambda)$ for silicon at the wavelengths used in this study [233]. Note that only the real refractive index is considered for the analysis performed in this dissertation as it alone contributes to the phase of light passing through the material.

Wavelength (energy)	n	k
390 nm (3.2 eV)	6.062	0.630
780 nm (1.60 eV)	3.714	0.008

Table A2.2 Real refractive index and extinction coefficient for silicon at room temperature.

The temperature dependence of the optical properties of silicon has been studied with pump probe techniques [281], as well as ellipsometry [282]. Additional studies have examined the optical properties of liquid silicon [283]. It was shown that the real refractive index n decreased and the imaginary index k increased for the liquid silicon relative to the room temperature values. Approximate values for the real refractive index and absorption coefficient of liquid silicon are provided in Table A2.3.

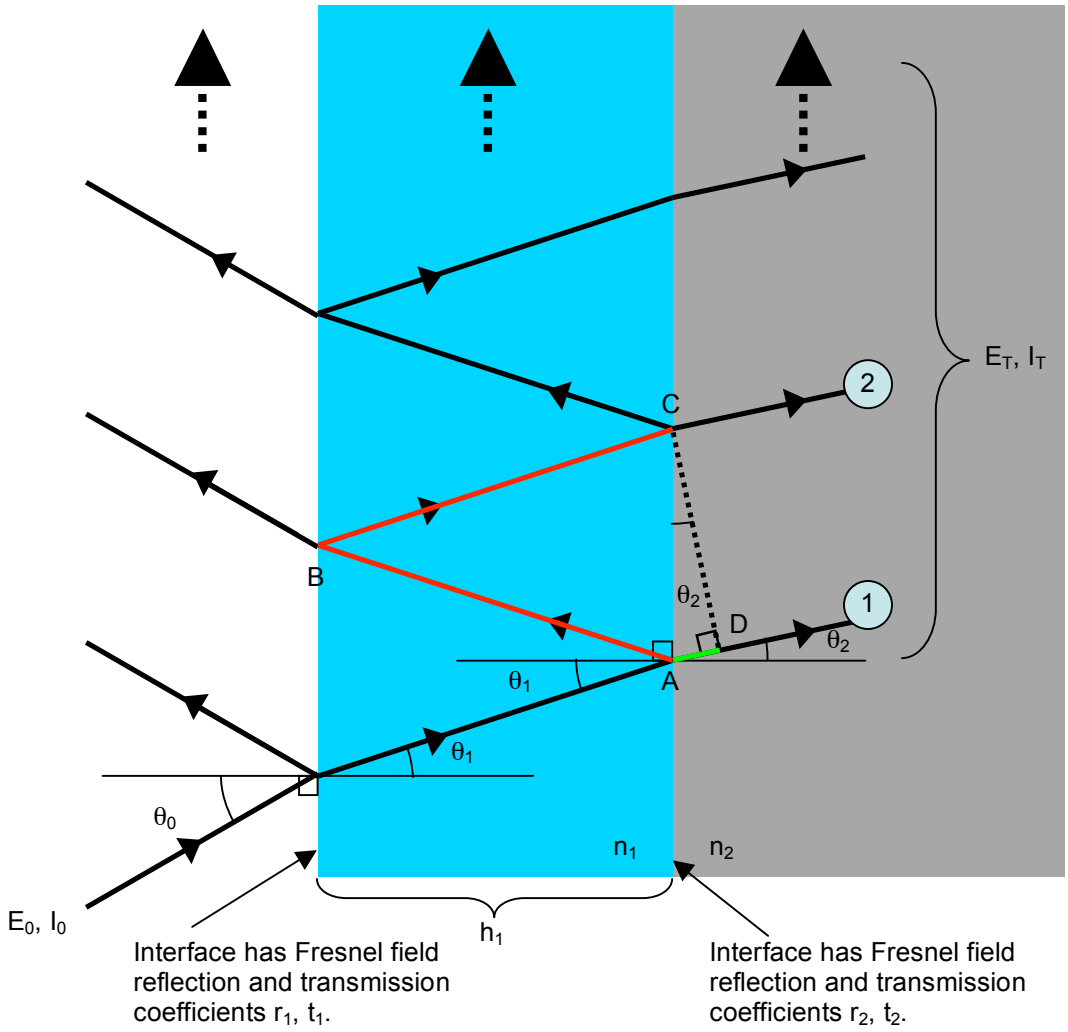

Figure A2.1 Schematic illustrating the interaction of a light with intensity I_0, electric field E_0, and wavelength λ_0 incident on a silicon substrate with real refractive index n_2 and semi-infinite thickness with an SiO_2 thin film of thickness h_1 and real refractive index n_1.

Wavelength (energy)	*n*	*k*
390 nm (3.2 eV)	2.1	4.6
780 nm (1.60 eV)	4.1	5.6

Table A2.3: Approximate real refractive index and extinction coefficient for liquid silicon [283].

A2.2 Reflectivity of Si(100) with oxide films as a function of film thickness.

In this section the Fresnel intensity transmission and reflection coefficients for a substrate with a thin surface film will be discussed. We will assume the exhibits

little absorption at the wavelength under consideration (i.e. $k << n$), such that the absorption coefficient k need not be used in the development of the reflectivity. This is valid for the case of the 780 nm light incident onto a crystalline silicon surface, but not appropriate for 390 nm light (see Table A2.1). The specific case of Si(100) with thin thermally grown SiO_2 films will be considered at the relevant wavelength (780 nm) used for the experiments discussed in this dissertation.

We wish to determine the Fresnel intensity transmission coefficient $\Im$ for transmission of light into the substrate with consideration given to the interference between multiple transmitted beams (illustrated in Figure A2.1). In Figure A2.1, a physical path length difference between subsequently transmitted rays 1 and 2 produces a phase difference between the rays that can lead the rays to interfere constructively or destructively. This interference due to multiple reflections can significantly modify the reflectivity of an interface depending largely on the optical properties of the thin film.

Consider a thin film of thickness h_1 and real refractive index n_1 on top of a substrate of semi-infinite thickness, and real refractive index n_2 (see schematic in Figure A2.1). Assume that a laser beam of wavelength λ_0 is incident in air (n_0 = 1) onto the top of the film with angle θ_0 with respect to the sample normal. The air/film interface has Fresnel field reflection and transmission coefficients r_1 and t_1 respectively, and the film/substrate interface has Fresnel field reflection and transmission coefficients r_2 and t_2 respectively. Furthermore, the air/film interface has Fresnel intensity reflection and transmission coefficients R_1 and T_1 respectively, and the film/substrate interface has Fresnel intensity reflection and transmission coefficients R_2 and T_2 respectively.

The transmission coefficient $\Im$ for the thin film is given by [231]:

$$\Im = \frac{I_T}{I_0} = \frac{T^2}{(1-R)^2} \frac{1}{1 + F \sin^2 \frac{\delta_{difference}}{2}} \qquad \text{(A2.2)}$$

Where $T = \sqrt{T_1 T_2}$ and $R = \sqrt{R_1 R_2}$, $\delta_{difference}$ is the phase difference between rays 1 and 2 (in Figure A2.1), and F is the Airy Function given in terms of R and T:

$$F = \frac{4R}{(1-R)^2} \tag{A2.3}$$

In order to determine phase difference $\delta_{difference}$, we first calculate the geometric path lengths *AB* = *BC*, and *AD* in Figure A2.1. Note that for normal incidence irradiation, the geometric path length *AD* need not be considered, and should evaluate to zero in the following. First we use Snell's law to determine the angles of transmission into the various layers θ_1 and θ_2 with respect to the incident angle θ_0.

$$n_0 \sin\theta_0 = n_1 \sin\theta_1 \Rightarrow \sin\theta_1 = \frac{n_0}{n_1}\sin\theta_0 \tag{A2.4}$$

$$n_1 \sin\theta_1 = n_2 \sin\theta_2 \Rightarrow \sin\theta_2 = \frac{n_1}{n_2}\sin\theta_1 \Rightarrow \sin\theta_2 = \frac{n_0}{n_2}\sin\theta_0 \tag{A2.5}$$

Given the film thickness h_1, the geometric length *AB* (and *BC*) is given by:

$$AB = BC = \frac{h_1}{\cos\theta_1} = \frac{h_1}{\sqrt{1-\sin^2\theta_1}} = \frac{n_1 h_1}{\sqrt{n_1^2 - n_0^2\sin^2\theta_0}} \tag{A2.6}$$

where we have used the results of Equation (A2.4) above. Next we determine the geometric length *AD* in terms of the film thickness h_1 and the incident angle θ_0. Given that:

$$\tan\theta_1 = \frac{AC}{2h_1} \tag{A2.7}$$

We obtain for the length *AC*:

$$AC = 2h_a \frac{\sin\theta_1}{\cos\theta_1} = 2h_a \frac{n_0 \sin\theta_0}{\sqrt{n_1^2 - n_0^2\sin^2\theta_0}} \tag{A2.8}$$

Next we recognize that:

$$\sin\theta_2 = \frac{AD}{AC} \tag{A2.9}$$

Such that the geometric distance *AD* is given by:

$$AD = AC\sin\theta_2 = AC\frac{n_0}{n_2}\sin\theta_0 = 2h_a \frac{n_0^2\sin^2\theta_0}{n_2\sqrt{n_1^2 - n_0^2\sin^2\theta_0}} \tag{A2.10}$$

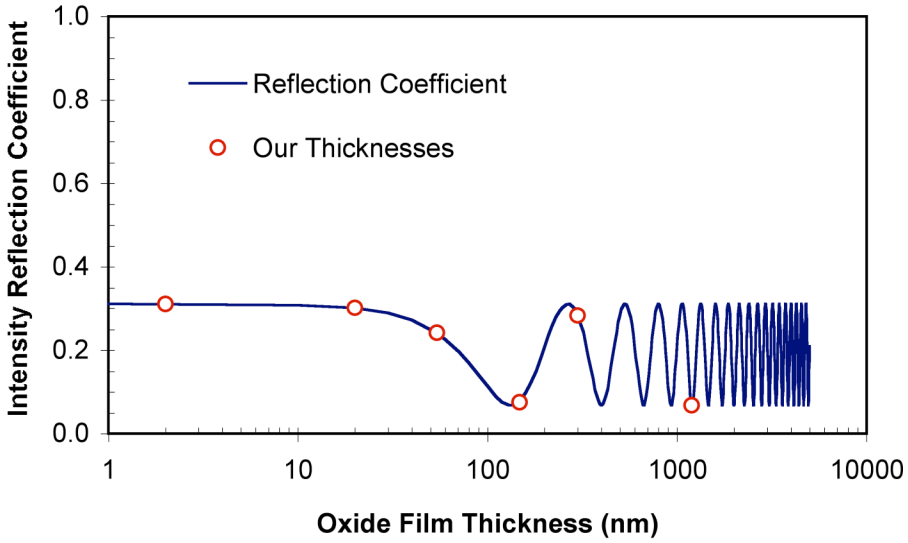

Figure A2.2 Fresnel intensity transmission coefficient for a crystalline silicon surface with a surface oxide (SiO_2) film as a function of oxide thickness for normal incidence irradiation. The coefficient was calculated using a wavelength of 780 nm, and a respective refractive index of of 3.714 for crystalline silicon and 1.4533 for SiO_2.

The phase acquired by an oscillating electric field due to propagation in a medium is given by [230]:

$$\delta = \vec{k} \cdot \vec{r} = |k||r|\cos\theta \qquad \text{(A2.11)}$$

Where $r\cos\theta$ is the distance traveled in the medium $\boldsymbol{k}$ is the wave vector:

$$|k| = \frac{2\pi}{\lambda} = \frac{2\pi n}{\lambda_0} \qquad \text{(A2.12)}$$

where λ_0 is the wavelength of the radiation in vacuum, and n is the refractive index of the medium in which the light propagates. An additional phase shift of 180° or π radians is acquired by the light that travels within the film whenever the light reflects from the substrate/film interface (assuming $n_2 > n_1 > n_0$) [231]. For one round trip in the film, we have for the phase difference between rays 1 and 2:

$$\delta_{difference} = \delta_{ABC} + \pi - \delta_{AD} = \left(\frac{2\pi}{\lambda_0}\right)\left[2n_1 AB - n_2 AD\right] + \pi \qquad \text{(A2.11)}$$

where we have used the fact that the geometric lengths *AB* and *BC* are equal. Using Equation (A2.6) for *AB* and Equation (A2.10) for *AD* we have:

$$\delta_{difference} = \delta_{ABC} + \pi - \delta_{AD} = \left(\frac{4\pi h_1}{\lambda_0}\right)\left[\sqrt{n_1^2 - n_0^2 \sin^2\theta_0}\right] + \pi \qquad \text{(A2.12)}$$

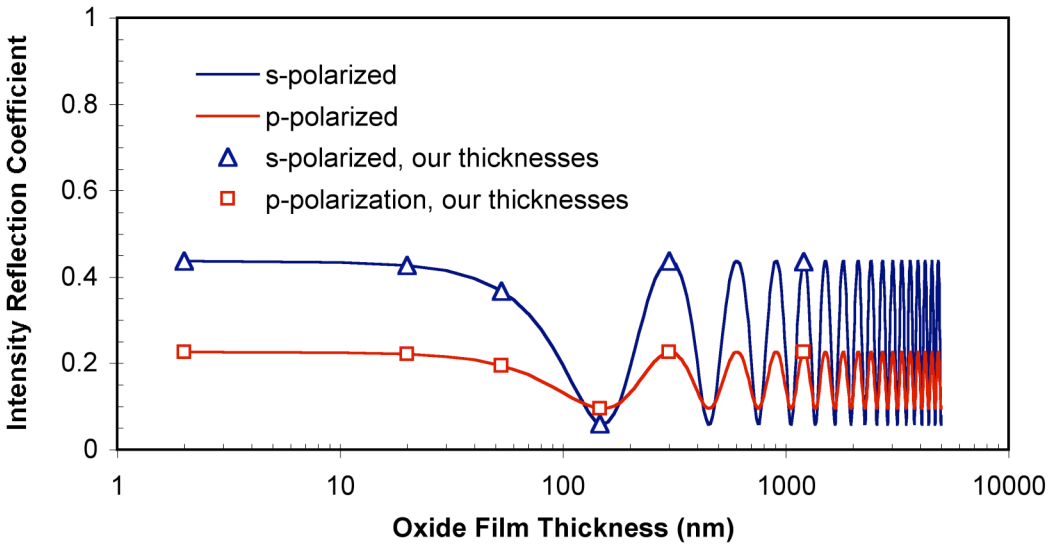

Figure A2.3 Fresnel intensity transmission coefficient for a crystalline silicon surface with a surface oxide (SiO_2) film as a function of oxide thickness for light incident at 41.8° with respect to the sample normal. The coefficient for s- and p-polarized radiation with respect to the sample surface is shown. The coefficient was calculated using a wavelength of 780 nm, and a respective refractive index of of 3.714 for crystalline silicon and 1.4533 for SiO_2.

where several algebraic steps in the derivation have been skipped.

Next we provide expressions for the Fresnel field reflection and transmission coefficients for the air/film interface and the film/substrate interface [231] for both s- and p-polarized radiation. Under the assumption that the magnetic permeability is the same for all materials, for the air/film interface we have [284]:

$$r_{s1} = \frac{-\sin(\theta_0 - \theta_1)}{\sin(\theta_0 + \theta_1)} \tag{A2.13}$$

$$t_{s1} = \frac{2\cos(\theta_0)\sin(\theta_1)}{\sin(\theta_0 + \theta_1)} \tag{A2.14}$$

$$r_{p1} = \frac{\tan(\theta_0 - \theta_1)}{\tan(\theta_0 + \theta_1)} \tag{A2.15}$$

$$t_{p1} = \frac{2\cos(\theta_0)\sin(\theta_1)}{\sin(\theta_0 + \theta_1)\cos(\theta_0 - \theta_1)} \tag{A2.16}$$

Similarly, for the film/substrate interface, we have:

$$r_{s2} = \frac{-\sin(\theta_1 - \theta_2)}{\sin(\theta_1 + \theta_2)} \tag{A2.17}$$

$$t_{s2} = \frac{2\cos(\theta_1)\sin(\theta_2)}{\sin(\theta_1 + \theta_2)} \tag{A2.18}$$

$$r_{p2} = \frac{\tan(\theta_1 - \theta_2)}{\tan(\theta_1 + \theta_2)} \tag{A2.19}$$

$$t_{p2} = \frac{2\cos(\theta_1)\sin(\theta_2)}{\sin(\theta_1 + \theta_2)\cos(\theta_1 - \theta_2)} \tag{A2.20}$$

The power (or intensity) reflection and transmission coefficients for the interfaces are obtained from the coefficients for the electric field as follows:

$$R_{s1} = |r_{s1}|^2 \qquad R_{p1} = |r_{p1}|^2 \qquad R_{s2} = |r_{s2}|^2 \qquad R_{p2} = |r_{p2}|^2 \tag{A2.21}$$

$$\left.\begin{aligned} T_{s1} &= \frac{n_1\cos\theta_1}{n_0\cos\theta_0}|t_{s1}|^2 \qquad T_{p1} = \frac{n_1\cos\theta_1}{n_0\cos\theta_0}|t_{p1}|^2 \\ T_{s2} &= \frac{n_2\cos\theta_2}{n_1\cos\theta_1}|t_{s2}|^2 \qquad T_{p2} = \frac{n_2\cos\theta_2}{n_1\cos\theta_1}|t_{p2}|^2 \end{aligned}\right\} \tag{A2.22}$$

Using the above expressions for the Fresnel intensity transmission and reflection coefficients, and provided $T = \sqrt{T_1 T_2}$ and $R = \sqrt{R_1 R_2}$ we have for *R* and *T* in Equations (A2.2) and (A2.3):

$$R_s = |r_{s1}||r_{s2}| \qquad R_p = |r_{p1}||r_{p2}| \tag{A2.23}$$

$$T_s = \sqrt{\frac{n_2\cos\theta_2}{n_0\cos\theta_0}}|t_{s1}||t_{s2}| \qquad T_p = \sqrt{\frac{n_2\cos\theta_2}{n_0\cos\theta_0}}|t_{p1}||t_{p2}| \tag{A2.24}$$

The reflectivity of a crystalline silicon surface with a surface silicon dioxide film at normal laser incidence is presented in Figure A2.2 (with application to Chapter 3.2.1), while the reflectivity for s- and p-polarized radiation at 41.8° with respect to the sample normal is presented in Figure A2.3 (with application to Chapter 3.2.2).

The reflectivity of a crystalline silicon surface with and without the native oxide (~ 2 nm in thickness) as a function of the angle of laser incidence for both s- and p-polarized radiation is presented in Figure A2.4. A simplified approach was taken to calculate the Fresnel intensity reflection coefficient for the case of the native oxide. Multiple reflections were not included in the calculations of the reflectivity in this case as the film was much thinner than the wavelength of the

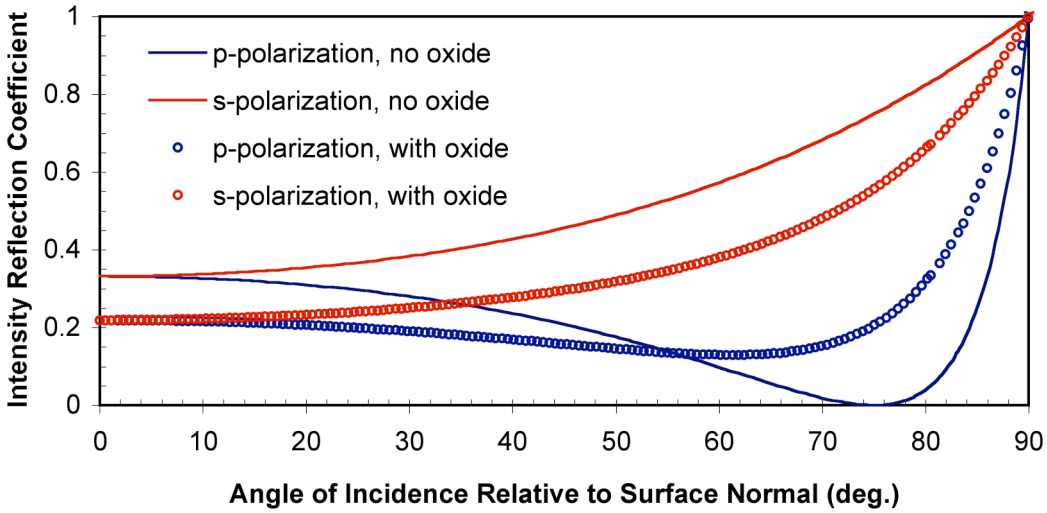

Figure A2.4 Fresnel intensity reflection coefficient for light transmitting into a silicon surface with and without a surface oxide (SiO_2) film. The coefficient were calculated using a wavelength of 780 nm, and refractive indices of 3.714 for crystalline silicon and 1.4533 for SiO_2. For this plot, the role of multiple reflections on the reflectivity were not considered. Recall 0° = normal incidence.

incident light. Equations (A2.13)-(A2.22) were used to calculate the field and intensity transmission coefficients for the air/oxide interface and oxide/silicon interface with $n_0 = 1$, $n_2 = 1.4537$, $n_3 = 3.714$. Once the coefficients for each interface were determined, the reflectivity of the sample with the oxide was calculated via:

$$R_{s,pTotal} = R_{s,p1}R_{s,p2} \qquad T_{s,pTotal} = T_{s,p1}T_{s,p2} \qquad \text{(A2.25)}$$

A2.3 Optical model and expression for material height as a function of Newton's rings

Time-resolved, front-view images of single pulse fs laser ablation of Si(100) with thermally grown oxide films exhibited an interference phenomenon known as Newton's rings (see Chapter 6.1.1). A schematic showing the origin of this interference phenomenon along with critical angles and material properties is presented in Figure A2.5. The Newton's rings result from interference between probe light reflected from the top surface of the molten Si layer attached to the bottom surface of the oxide film, and probe light reflected from the pool of molten silicon left at the surface of the substrate. We have already measured the times at which an interference minimum is produced in the center of the ablation

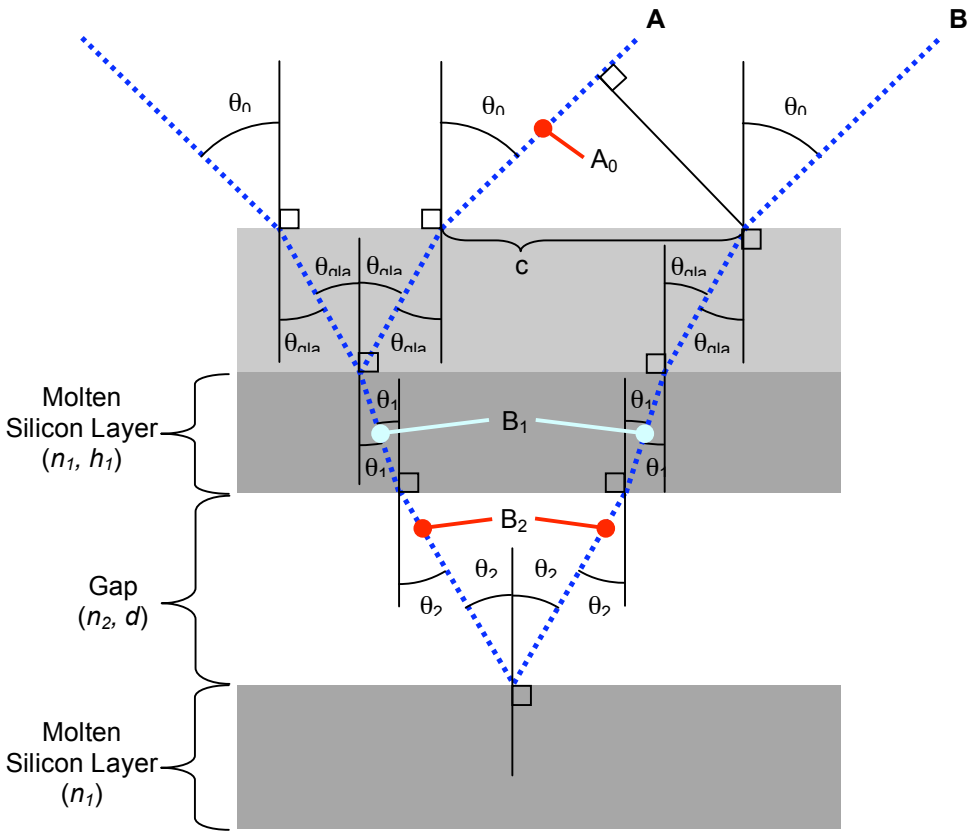

Figure A2.5 Schematic showing critical angles and material parameters used in theoretical development of Newton's rings phenomenon. The Newton's rings result from interference of probe light reflected from the top surface of the ejected liquid silicon layer (reflection A) and probe light reflected from the liquid silicon remaining on the substrate surface (reflection B).

feature (see Figure 6.1.3). To determine the velocity of the ablating material, the gap height *d* which yields destructive interference at the center of the ablation feature was determined.

To begin, the following optical properties are assumed known: the refractive index of air, $n_0 = 1$, the angle of incidence of the probe pulse $\theta_0 = 49 \pm 1°$, the wavelength of the probe light, $\lambda_0 = 388$ nm, and the real refractive index of liquid silicon (at $\lambda_0 = 388$ nm) $n_1 \approx 2.1$(see Section A2.1, and [283]). Note that a refractive index of $n_1 = 6.062$ (at $\lambda_0 = 388$ nm) was used for solid silicon at room temperature where applicable. The imaginary component (or extinction coefficient) of the refractive index *k*, was not used as the following theoretical discussion will focus on the phase acquired by the probe light alone [230]. The imaginary component would be necessary for more detailed analysis of the

magnitude of the reflectivity changes [35] (as opposed to simply constructive or destructive interference). As shown in Figure A2.5, the reflections **A** and **B** acquire a common phase through the oxide film, such that the optical properties of the film were not necessary for the analysis that follows. Furthermore, the molten pool of silicon at the substrate surface is assumed to have a thickness far greater than the molten layer of silicon at the bottom surface of the glass, such that the probe light transmitted into the substrate is absorbed and no reflection from the liquid/solid silicon interface is observed. The unknown quantities include the refractive index of the gap material, n_2, and the thickness of the liquid silicon layer on the bottom surface of the oxide film, h_1.

First we consider the probe light that will form reflection **B** in Figure A2.5. We will apply Snell's law to determine the angle of refraction for each interface that reflection **B** encounters along its path. First, prior to separation into reflections **A** and **B**, the probe light passes into the oxide film:

$$n_{glass} \sin\theta_{glass} = n_0 \sin\theta_0 \tag{A2.26}$$

where the n_{glass} = 1.4714 is the refractive index of the oxide film. At the interface between the oxide film and the molten silicon layer:

$$n_1 \sin\theta_1 = n_{glass} \sin\theta_{glass} = n_0 \sin\theta_0 \tag{A2.27}$$

where we have used Equation (A2.26). Finally, at the interface between the molten silicon layer and the gap:

$$n_2 \sin\theta_2 = n_1 \sin\theta_1 = n_{glass} \sin\theta_{glass} = n_0 \sin\theta_0 \tag{A2.28}$$

where we have used Equation (A2.26) and (A2.27). In this fashion, we find that the angles are given by:

$$\sin\theta_{glass} = \left(\frac{n_0}{n_{glass}} \sin\theta_0 \right) \tag{A2.29}$$

$$\sin\theta_1 = \left(\frac{n_0}{n1} \sin\theta_0 \right) \tag{A2.30}$$

$$\sin\theta_2 = \left(\frac{n_0}{n_2} \sin\theta_0 \right) \tag{A2.31}$$

Next the physical path lengths are determined for reflection **B** through the liquid silicon layer on the bottom surface of the oxide (B_1), and through the gap material (B_2). Assuming the liquid silicon has a thickness h_1, and the light traverses the layer with angle θ_1 with respect to the normal, we have:

$$\cos\theta_1 = \sqrt{1-\sin^2\theta_1} = \frac{h_1}{B_1} \tag{A2.32}$$

Rearranging equation A3.32, we obtain an expression for the physical length B_1.

$$B_1 = \frac{h_1 n_1}{\sqrt{n_1^2 - n_0^2\sin^2\theta_0}} \tag{A2.33}$$

where we have used Equation (A2.30) for sin θ_1. Similarly, the physical path length B_2 through the gap material is given by:

$$B_2 = \frac{dn_2}{\sqrt{n_2^2 - n_0^2\sin^2\theta_0}} \tag{A2.34}$$

To determine the optical phase acquired by reflection **B** as it traverses its path through the film, we consider the general phase ϕ_i of an oscillating electric field due to propagation through space (i.e. we neglect the phase component that is oscillatory in time) [230]:

$$\phi_i = \vec{k}_i \cdot \vec{r} = |k_i||r|\cos\theta_i \tag{A2.35}$$

where $\boldsymbol{k_i}$ is the wavevector in the region of interest:

$$|k_i| = \frac{2\pi}{\lambda_i} = \frac{2\pi n_i}{\lambda_0} \tag{A2.36}$$

where n_i is the real refractive index in the region of interest, and λ_0 is the wavelength of the light in vacuum. As we have determined the physical path lengths along the direction of propagation, the dot product in Equation (A2.35) is not necessary, and $\cos\theta_i = 1$.

Thus we have for the phase acquired by **B** through the liquid silicon layer on the bottom surface of the oxide film, ϕ_1:

$$\phi_1 = |k_1|B_1 = \frac{2\pi}{\lambda_0}\frac{h_1 n_1^2}{\sqrt{n_1^2 - n_0^2\sin^2\theta_0}} \tag{A2.37}$$

The phase acquired by **B** through the gap material, ϕ_2 is given by:

$$\phi_2 = |k_2| B_2 = \frac{2\pi}{\lambda_0} \frac{dn_2^2}{\sqrt{n_2^2 - n_0^2 \sin^2 \theta_0}} \tag{A2.38}$$

We note that reflection **B** traverses physical lengths B_1 and B_2 twice during its trip. Furthermore, reflection **B** acquires a phase shift of 180° (or π radians) upon reflection from the liquid silicon puddle on the surface of the substrate (as $n_2 > n_{glass}$). However reflection **A** acquires the same additional phase by reflecting off the layer of liquid silicon on the bottom surface of the oxide film, so we neglect the contribution of phase due to reflection. As such, the total phase acquired by reflection **B** is given by:

$$\phi_B = 2|k_1| B_1 + 2|k_2| B_2 = \frac{4\pi}{\lambda_0} \left(\frac{h_1 n_1^2}{\sqrt{n_1^2 - n_0^2 \sin^2 \theta_0}} + \frac{dn_2^2}{\sqrt{n_2^2 - n_0^2 \sin^2 \theta_0}} \right) \tag{A2.39}$$

Next we calculate the phase acquired by reflection **A** as it traverses the distance A_0 in the air. This is done because we must consider the respective phases of reflections A and B along a common phase front perpendicular to the propagation of both rays in order to properly determine the degree of interference between them [230, 231]. The physical length of *c* can be determined in terms of B_1 and B_2:

$$c = 2(B_1 \sin \theta_1) + 2(B_2 \sin \theta_2) = 2 n_0 \sin \theta_0 \left[\frac{B_1}{n_1} + \frac{B_2}{n_2} \right] \tag{A2.40}$$

where we have used Equations (A2.30) and (A2.31). A_0 can then be determined in terms of the length *c*:

$$A_0 = c \sin \theta_0 = 2 n_0 \sin^2 \theta_0 \left[\frac{B_1}{n_1} + \frac{B_2}{n_2} \right] \tag{A2.41}$$

Using the expressions for B_1 and B_2 above, we have for the phase acquired by reflection **A** along path A_0:

$$\phi_A = |k_0| A_0 = \frac{4\pi n_0^2}{\lambda_0} \sin^2 \theta_0 \left(\frac{h_1}{\sqrt{n_1^2 - n_0^2 \sin^2 \theta_0}} + \frac{d}{\sqrt{n_2^2 - n_0^2 \sin^2 \theta_0}} \right) \tag{A2.42}$$

Destructive interference occurs when the phase difference between the reflections **A** and **B** is equal to an odd integer multiple of π:

$$\Delta\phi = \phi_B - \phi_A = (2m+1)\pi \tag{A2.43}$$

Where m is an integer (m = 0, 1, 2…). We note that under the analysis presented in Chapter 5.1.3, m is time dependent, as more Newton's rings (and therefore more interference minima) emerge as the ablation event proceeds. Furthermore, we are interested in the degree of interference at the center of the ablation feature, which due to the Gaussian spatial fluence profile of the incident beam, ablates with the greatest velocity. The plot in Figure 6.1.3 shows the time delay at which an interference minimum is present at the center of the ablation feature. Thus in order to determine the velocity of the ablated material, we need to determine the gap height d at when destructive interference occurs. Solving for d in Equation (A2.43) yields, with the appropriate phases from Equations (A2.39) and (A2.42):

$$d = \frac{\frac{\lambda_0}{4}(2m(t)+1) - \frac{h_1}{\sqrt{n_1^2 - n_0^2\sin^2\theta_0}}\left(n_1^2 - n_0^2\sin^2\theta_0\right)}{\frac{1}{\sqrt{n_2^2 - n_0^2\sin^2\theta_0}}\left(n_2^2 - n_0^2\sin^2\theta_0\right)} \tag{A2.44}$$

Equation (A2.44) is used in Chapter 6.1.1 and 6.1.3 to determine the velocity of the ablated material from time-resolved front-view images. In those sections, it is assumed that the minima order m is the *only* time dependent quantity in Equation (A2.44) on the timescale in which the observation of the ablation event was made with the front-view imaging technique.

Appendix 3

Macro-micro interfacing mold for electrophoresis device

The macro to micro mold described here was developed to accommodate inverted observation with a confocal, fluorescent microscope. This geometry demanded a mold with a depression to hold a downward facing section of wafer with linear blister channels (see Chapter 5.2.3). The mold is comprised solely of this depression, which should be the size of a typical device. Refer to Figure A3.1 for a schematic of the technique that follows.

First, a piece of silicon wafer (typically scrap) was diced to the size of samples upon which linear blister channels were to be produced (typical sample size was 12 mm tall by 5 – 10 mm wide). This piece of silicon was then fixed to the bottom of a 2" diameter plastic Petri dish with double-sided stick tape. Liquid PDMS was poured into the Petri dish (after the curing agent had been added and mixed into the PDMS in a separate plastic Petri dish), such that the level of the PDMS was approximately 2-3 mm above the piece of silicon at the bottom of the dish. The PDMS was then allowed to cure, typically for 48 hrs. at room temperature.

Following curing, the firm PDMS was cut into a large square using an Exacto™ knife, 3 cm by 3 cm in area, with the silicon piece centered in the square. The rim of the plastic Petri dish was typically cut away with wire snips to facilitate the careful removal of the PDMS from the bottom of the Petri dish. If cured properly, the PDMS should easily pull away from the plastic. Once the PDMS was free from the plastic Petri dish, the piece of silicon was also carefully removed forming the desired depression to accommodate the downward facing fluidic chip.

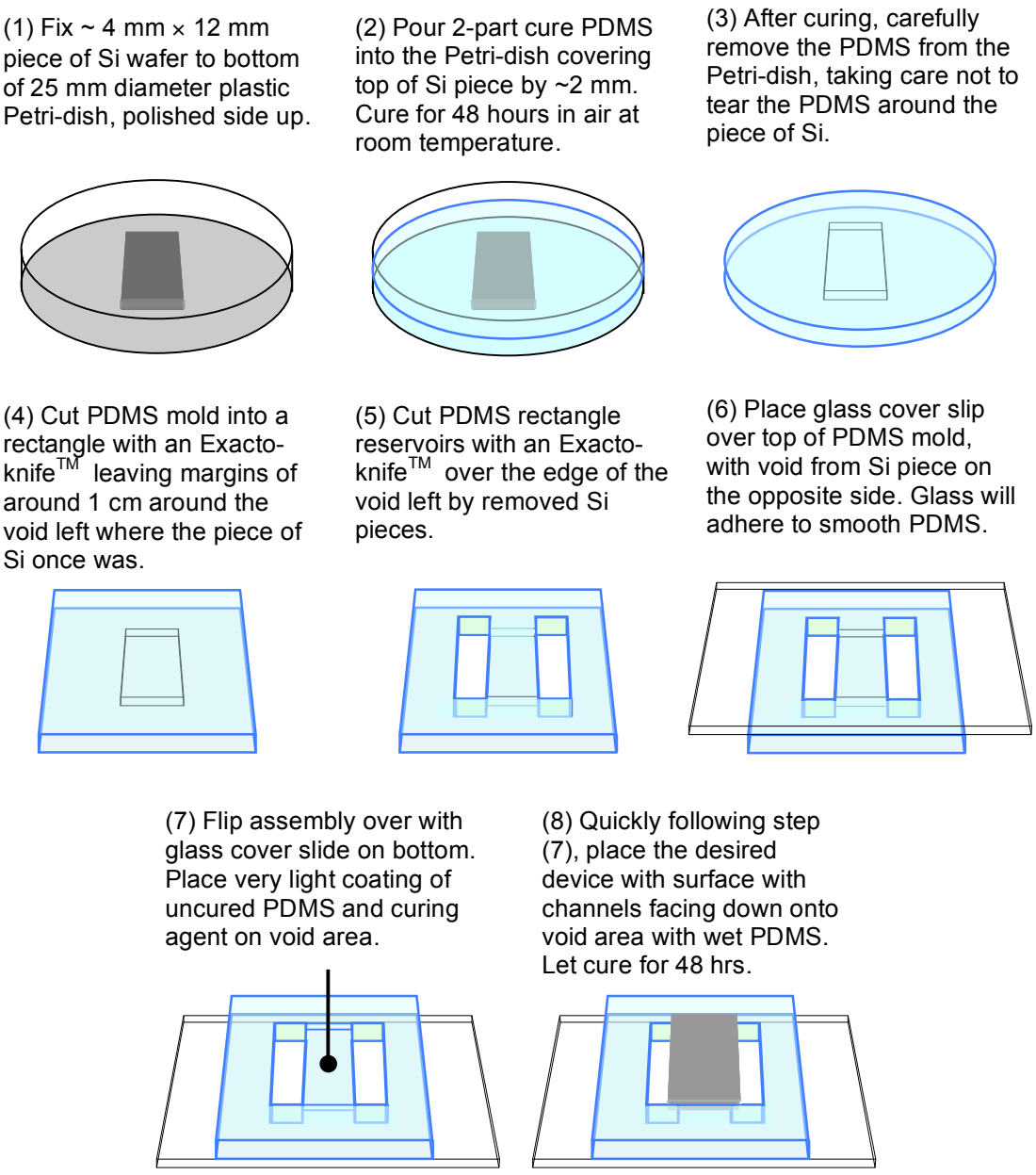

Figure A3.1 Schematic showing technique for producing PDMS mold and reservoirs for fluid delivery to the end of a linear blister channels device.

Next, reservoirs were then cut into the PDMS along the long edge of the depression left by the now absent piece of silicon. These reservoirs were separated by 2-4 mm, depending on the width of the sample intended for the mold. The “reservoirs” are simply two rectangular holes through the PDMS mold, the bottom of which will be a glass cover slip which is incorporated in the last

step. Once the mold was complete, the fluid chip is placed into the depression with a small amount of wet PDMS added to the top of the sample to assure adhesion between the sample surface and the solid PDMS of the mold. Be careful to prevent any wet PDMS from getting into the channels, as this will surely block them and at best impede their flow. Partial “coating” of the bottom surface of the channels with PDMS may however, decrease cavitation or local boiling due to current leakage to the substrate during voltage application (see Chapter 5.2.3) and should be pursued in future work. Let the wet PDMS adhering the sample to the mold cure for 2 days, or in a glass Petri dish under a heat lamp (40 °C) for 10 minutes. It should be noted that cured PDMS adheres semi-permanently to glass on its own with little need for additional adhesive, however in order to assure final isolation of the reservoirs additional adhesive was applied between the sample and the PDMS mold.

Finally, a glass cover slip is placed on the bottom of the mold, such that with the sample in place, the two reservoirs were enclosed on 5 of 6 sides. The reservoirs should now be isolated from each other so that fluid can only travel between the reservoirs by passing through the linear channels of the chip. Electrical leads (wires) from a voltage supply can be placed in the reservoirs with desired fluids for electrophoresis. A picture of a complete chip in a mold with wire leads in place is presented in Figure 5.2.19.

Bibliography

[1] C. V. Shank, R. Yen, and C. Hirlimann, *Time-resolved reflectivity measurements of femtosecond-optical-pulse induced phase transformations in silicon*, Physical Review Letters **50**, 454 (1983).
[2] D. Hulin, M. Combescot, J. Bok, A. Migus, J. Y. Vinet, and A. Antonetti, *Energy transfer during silicon irradiation by femtosecond laser pulse*, Physical Review Letters **52**, 1998 (1984).
[3] M. C. Downer, R. L. Fork, and C. V. Shank, *Femtosecond imaging of melting and evaporation at a photoexcited silicon surface*, Journal of the Optical Society of America B **2**, 595 (1985).
[4] R. W. Schoenlein, W. Z. Lin, J. G. Fujimoto, and G. L. Eesley, *Femtosecond studies of nonequilibrium processes in metals*, Physical Review Letters **58**, 1680 (1987).
[5] W.-Z. Lin, R. W. Shoenlein, J. G. Fujimoto, and E. P. Ippen, *Femtosecond absorption saturation studies of hot carriers in GaAs and AlGaAs*, IEEE Journal of Quantum Electronics **24**, 267 (1988).
[6] H. W. K. Tom, G. D. Aumiller, and C. H. Brito-Cruz, *Time-resolved study of laser-induced disorder of Si surfaces*, Physical Review Letters **60**, 1438 (1988).
[7] M. Dantus, M. J. Rosker, and A. H. Zewail, *Real-time femtosecond probing of transition-states in chemical-reactions*, Journal of Chemical Physics **87**, 2395 (1987).
[8] Y. J. Yan, L. E. Fried, and S. Mukamel, *Ultrafast pump-probe spectroscopy: Femtosecond dynamics in Liouville space*, Journal of Physical Chemistry **93**, 8149 (1989).
[9] M. J. Rosker, M. Dantus, and A. H. Zewail, *Femtosecond real-time probing of reactions 1. The technique*, Journal of Chemical Physics **89**, 6113 (1988).
[10] P. Maine, D. Strickland, P. Bado, M. Pessot, and G. Mourou, *Generation of ultrahigh peak power pulses by chirped pulse amplification*, IEEE Journal of Quantum Electronics **24**, 398 (1988).
[11] M. Pessot, J. Squier, G. Mourou, and D. J. Harter, *Chirped-pulse amplification of 100-fsec pulses*, Optics Letters **14**, 797 (1989).
[12] M. Lenzner, J. Kruger, S. Sartania, C. Spielmann, G. Mourou, W. Kautek, and F. Krausz, *Femtosecond optical breakdown in dielectrics*, Physical Review Letters **80**, 4076 (1998).
[13] B. C. Stuart, M. D. Feit, S. Herman, A. M. Rubenchik, B. W. Shore, and M. D. Perry, *Nanosecond-to-femtosecond laser-induced breakdown in dielectrics*, Physical Review B **53**, 1749 (1996).
[14] X. Liu, D. Du, and G. Mourou, *Laser ablation and micromachining with ultrashort laser pulses*, IEEE Journal of Quantum Electronics **33**, 1706 (1997).
[15] A. Cavalleri, K. Sokolowski-Tinten, J. Bialkowski, M. Schreiner, and D. v. d. Linde, *Femtosecond melting and ablation of semiconductors studied with time of flight mass spectroscopy*, Journal of Applied Physics **85**, 3301 (1999).
[16] T.-H. Her, R. J. Finlay, C. Wu, S. Deliwala, and E. Mazur, *Microstructuring of silicon with femtosecond laser pulses*, Applied Physics Letters **73**, 1673 (1998).
[17] M. Weingartner, R. Elschner, and O. Bostanjoglo, *Patterning of silicon - differences between nanosecond and femtosecond laser pulses*, Applied Surface Science **138-139**, 499 (1999).

[18] P. P. Pronko, S. K. Dutta, D. Du, and R. K. Singh, *Thermophysical effects in laser processing of materials with picosecond and femtosecond pulses*, Journal of Applied Physics **78**, 6233 (1995).
[19] C. Momma, B. N. Chichkov, S. Nolte, F. von Alvensleben, A. Tunnermann, H. Welling, and B. Wellegehausen, *Short-pulse ablation of solid targets*, Optics Communications **129**, 134 (1996).
[20] S. Nolte, C. Momma, H. Jacobs, A. Tunnermann, B. N. Chichkov, B. Wellegehausen, and H. Welling, *Ablation of metals by ultrashort laser pulses*, Journal of the Optical Society of America B **14**, 2716 (1997).
[21] P. P. Pronko, S. K. Dutta, J. Squier, J. V. Rudd, D. Du, and G. Mourou, *Machining of submicron holes using a femtosecond laser at 800-nm*, Optics Communications **114**, 106 (1995).
[22] K. Furusawa, K. Takahashi, H. Kumagai, K. Midorikawa, and M. Obara, *Ablation characteristics of Au, Ag, and Cu metals using a femtosecond Ti:sapphire laser*, Applied Physics A **69**, S359 (1999).
[23] D. Du, X. Liu, G. Korn, J. Squier, and G. Mourou, *Laser-induced breakdown by impact ionization in SiO_2 with pulse widths from 7 ns to 150 fs*, Applied Physics Letters **64**, 3071 (1994).
[24] B. N. Chichkov, C. Momma, S. Nolte, F. Von Alvensleben, and A. Tunnermann, *Femtosecond, picosecond, and nanosecond laser ablation of solids*, Applied Physics A **63**, 109 (1996).
[25] M. S. Amer, M. A. El-Ashry, L. R. Dosser, K. E. Hix, J. F. Maguire, and B. Irwin, *Femtosecond versus nanosecond laser machining: a comparison of induced stresses and structural changes in silicon wafers*, Applied Surface Science **242**, 162 (2005).
[26] M. Hashida, A. F. Semerok, O. Gobert, G. Petite, Y. Izawa, and J. F.-. Wagner, *Ablation threshold dependence on pulse duration for copper*, Applied Surface Science **197-198**, 862 (2002).
[27] S. Preuss, A. Demchuk, and M. Stuke, *Subpicosecond UV laser-ablation of metals*, Applied Physics A **61**, 33 (1995).
[28] R. Le Harzic, N. Huot, E. Audouard, C. Jonin, P. Laporte, S. Valette, A. Fraczkiewicz, and R. Fortunier, *Comparison of heat-affected zones due to nanosecond and femtosecond laser pulses using transmission electron microscopy*, Applied Physics Letters **80**, 3886 (2002).
[29] S. Valette, E. Audouard, R. Le Harzic, N. Huot, P. Laporte, and R. Fortunier, *Heat affected zone in alumunimum single crystals submitted to femtosecond laser irradiations*, Applied Surface Science **239**, 381 (2005).
[30] M. D. Perry, B. C. Stuart, P. S. Banks, M. D. Feit, V. Yanovsky, and A. M. Rubenchik, *Ultrashort-pulse laser machining of dielectric materials*, Journal of Applied Physics **85**, 6803 (1999).
[31] J. Bekesi, J.-H. Klein-Wiele, and P. Simon, *Efficient submicron processing of metals with femtosecond UV pulses*, Applied Physics A **76**, 355 (2003).
[32] F. Korte, S. Nolte, B. N. Chichkov, T. Bauer, G. Kamlage, T. Wagner, C. Fallnich, and H. Welling, *Far-field and near-field materials processing with femtosecond laser pulses*, Applied Physics A **69**, S7 (1999).

[33] A. P. Joglekar, H. Liu, G. J. Spooner, E. Meyhofer, G. Mourou, and A. J. Hunt, *A study of the deterministic character of optical damage by femtosecond laser pulses and applications to nanomachining*, Applied Physics B **77**, 25 (2003).
[34] K. Sokolowski-Tinten, J. Bialkowski, A. Cavalleri, D. von der Linde, A. Oparin, J. Meyer-ter-Vehn, and S. I. Anisimov, *Transient states of matter during short pulsed laser ablation*, Physical Review Letters **81**, 224 (1998).
[35] D. von der Linde, and K. Sokolowski-Tinten, *The physical mechanisms of short-pulse laser ablation*, Applied Surface Science **154-155**, 1 (2000).
[36] S. I. Anisimov, N. A. Inogamov, A. Oparin, B. Rethfeld, T. Yabe, M. Ogawa, and V. E. Fortov, *Pulsed laser evaporation: equation-of-state effects*, Applied Physics A **69**, 617 (1999).
[37] B. Rethfeld, K. Sokolowski-Tinten, D. von der Linde, and S. I. Anisimov, *Ultrafast thermal melting of laser-exited solids by homogeneous nucleation*, Physical Review B **65**, 092103 (2002).
[38] D. A. Reis, K. J. Gaffney, G. H. Gilmer, and B. Torralva, *Ultrafast dynamics of laser excited solids*, Materials Research Society Bulletin **31**, 601 (2006).
[39] I. H. Chowdhury, and X. Xu, *Heat transfer in femtosecond laser processing of metal*, Numerical Heat Transfer, Part A **44**, 219 (2003).
[40] F. Vidal, T. W. Johnson, S. Laville, O. Barthemlemy, M. Chaker, B. Le Drogoff, J. Margot, and M. Sabsabi, *Critical point phase seperation in laser ablation of conductors*, Physical Review Letters **86**, 2573 (2001).
[41] J. Konig, S. Nolte, and A. Tunnermann, *Plasma evolution during metal ablation with ultrashort laser pulses*, Optics Express **13**, 10597 (2005).
[42] J. K. Chen, and J. E. Beraun, *Modelling of ultrashort laser ablation of gold films in vacuum*, Journal of Optics A: Pure and Applied Optics **5**, 168 (2003).
[43] A. Miotello, and R. Kelly, *Critical assessment of thermal models for laser sputtering at high fluences*, Applied Physics Letters **67**, 3535 (1995).
[44] P. Lorazo, L. J. Lewis, and M. Meunier, *Thermodynamic pathways to melting, ablation, and solidification in absorbing solids under pulsed laser irradiation*, Physical Review B **73**, 134108 (2006).
[45] A. K. Upadhyay, and H. M. Urbassek, *Effect of laser pulse width on material phenomena in ultrathin metal films irradiated by an ultrafast laser: molecular-dynamics study*, Journal of Physics D: Applied Physics **40**, 3518 (2007).
[46] A. Borowiec, and H. K. Haugen, *Subwavelength ripple formation on the surfaces of compound semiconductors irradiated with femtosecond laser pulses*, Applied Physics Letters **82**, 4462 (2003).
[47] A. Borowiec, M. Mackenzie, G. C. Weatherly, and H. K. Haugen, *Femtosecond laser pulse ablation of GaAs and InP: studies utilizing scanning transmission electron microscopy*, Applied Physics A **77**, 411 (2003).
[48] A. Borowiec, M. Mackenzie, G. C. Weatherly, and H. K. Haugen, *Femtosecond laser pulse ablation of GaAs and InP: studies utilizing scanning and transmission electron microscopy*, Applied Physics A **77**, 411 (2003).
[49] A. Borowiec, and H. K. Haugen, *Femtosecond laser micromachining of grooves in indium phosphide*, Applied Physics A **79**, 521 (2004).

[50] J. Bonse, S. Baudach, J. Kruger, W. Kautek, and M. Lenzner, *Femtosecond laser ablation of silicon-modification thresholds and morphology*, Applied Physics A **74**, 19 (2002).
[51] J. Bonse, J. M. Wrobel, K. W. Brzezinka, N. Esser, and W. Kautek, *Femtosecond laser irradiation of indium phosphide in air: Raman spectroscopic and atomic force microscopic investigations*, Applied Surface Science **202**, 272 (2002).
[52] J. Bonse, K. W. Brzezinka, and A. J. Meixner, *Modifying single-crystalline silicon by femtosecond laser pulses: an analysis by micro Raman spectroscopy, scanning laser microscopy and atomic force microscopy*, Applied Surface Science **221**, 215 (2004).
[53] J. Bonse, M. Munz, and H. Sturm, *Scanning force microscopy investigations of the femtosecond laser pulse irradiation of indium phosphide in air*, IEEE Transactions on Nanotechnology **3**, 358 (2004).
[54] P. Caron, and T. Khan, *Evolution of Ni-based superalloys for single crystal gas turbine blade applications*, Aerospace Science and Technology **3**, 513 (1999).
[55] T. M. Pollock, and S. Tin, *Nickel-based superalloys for advanced turbine engines: chemistry, microstructure, and properties*, Journal of Propulsion and Power **22**, 361 (2006).
[56] J. P. McDonald, S. Ma, J. A. Nees, T. M. Pollock, and S. M. Yalisove, *Pump-probe imaging of single pulse femtosecond laser ablation of the CMSX-4 Ni-based superalloy*, In preparation.
[57] J. P. McDonald, D. K. Das, J. A. Nees, T. M. Pollock, and S. M. Yalisove, *Quasi non-destructive orthogonal dual-pulse LIBS of the Ni-based superalloy CMSX-4*, In preparation.
[58] M. Das, J. P. McDonald, T. M. Pollock, S. M. Yalisove, and K. S. Thornton, *Pump-probe shadowgraphic imaging and 2D-Flash simulation of femtosecond laser ablation of the CMSX-4 Ni-based superalloy*, In preparation.
[59] C. Jacoboni, C. Canali, G. Ottaviani, and A. A. Quaranta, *Review of some charge transport properties of silicon*, Solid State Electronics **20**, 77 (1977).
[60] S. R. Hofstein, and F. P. Heiman, *Silicon insulated-gate field-effect transistor*, Proceedings of the IEEE **51**, 1190 (1963).
[61] J. M. Liu, L. A. Lompre, H. Kurz, and N. Bloembergen, *Phenomenology of picosecond heating and evaporation of silicon surfaces coated with SiO_2 layers*, Applied Physics A **34**, 25 (1984).
[62] P. Stampfli, and K. H. Bennemann, *Theory for the laser-induced femtosecond phase transition of silicon and GaAs*, Applied Physics A **60**, 191 (1995).
[63] P. P. Pronko, P. A. V. Rompay, C. Horvath, F. Loesel, T. Juhasz, X. Liu, and G. Mourou, *Avalanche ionization and dielectric breakdown in silicon with ultrafast laser pulses*, Physical Review B **58**, 2387 (1998).
[64] K. Sokolowski-Tinten, and D. von der Linde, *Generation of dense electron-hole plasmas in silicon*, Physical Review B **61**, 2643 (2000).
[65] T. Y. Choi, and C. P. Grigoropoulos, *Plasma and ablation dynamics in ultrafast laser processing of crystalline silicon*, Journal of Applied Physics **92**, 4918 (2002).
[66] A. J. Sabbah, and D. M. Riffe, *Femtosecond pump-probe reflectivity study of silicon carrier dynamics*, Physical Review B **66**, 165217 (2002).

[67] A. Borowiec, M. Mackenzie, G. C. Weatherly, and H. K. Haugen, *Transmission and scanning electron microscopy studies of single femtosecond-laser-pulse ablation of silicon*, Applied Physics A **76**, 201 (2003).
[68] S. Amoruso, C. Altucci, R. Bruzzese, C. De Lisio, N. Spinelli, R. Velotta, M. Vitiello, and X. Wang, *Study of the plamsa plume generated during near IR femtosecond laser irradiation of silicon targets*, Applied Physics A **79**, 1377 (2004).
[69] A. V. Bulgakov, I. Ozerov, and W. Marine, *Silicon clusters produced by femtosecond laser ablation: non-thermal emission and gas-phase condensation*, Applied Physics A **79**, 1591 (2004).
[70] J. Jia, M. Li, and C. V. Thompson, *Amorphization of silicon by femtosecond laser pulses*, Applied Physics Letters **84**, 3205 (2004).
[71] X. Mao, X. Zeng, S.-B. Wen, and R. E. Russo, *Time-resolved plasma properties for double pulsed laser-induced breakdown spectroscopy of silicon*, Spectrochimica Acta Part B: Atomic Spectroscopy **60**, 960 (2005).
[72] X. Zeng, X. L. Mao, R. Greif, and R. E. Russo, *Experimental investigation of ablation efficiency and plasma expansion during femtosecond and nanosecond laser ablation of silicon*, Applied Physics A **80**, 237 (2005).
[73] J. P. McDonald, A. A. McClelland, Y. N. Picard, and S. M. Yalisove, *Role of a native oxide on femtosecond laser interaction with silicon (100) near the damage threshold*, Applied Physics Letters **86**, 264103 (2005).
[74] J. P. McDonald, V. R. Mistry, K. E. Ray, J. A. Nees, N. R. Moody, and S. M. Yalisove, *Femtosecond-laser-induced delamination and blister formation in thermal oxide films on silicon (100)*, Applied Physics Letters **88**, 153121 (2006).
[75] J. P. McDonald, V. R. Mistry, K. E. Ray, and S. M. Yalisove, *Femtosecond pulsed laser direct write production of nano- and microfluidic channels*, Applied Physics Letters **88**, 183113 (2006).
[76] B. R. Tull, J. E. Carey, E. Mazur, J. P. McDonald, and S. M. Yalisove, *Silicon surface morphologies after femtosecond laser irradiation*, Materials Research Society Bulletin **31**, 626 (2006).
[77] J. P. McDonald, J. A. Nees, and S. M. Yalisove, *Pump-probe imaging of femtosecond pulse laser abaltion of silicon with thermally grown oxide films*, In preparation.
[78] J. W. Chan, T. R. Huser, S. H. Risbud, and D. M. Krol, *Modification of the fused silica glass network associated with waveguide fabrication using femtosecond laser pulses*, Applied Physics A **76**, 367 (2003).
[79] T. Gorelik, M. Will, S. Nolte, A. Tuennermann, and U. Glatzel, *Transmission electron microscopy studies of femtosecond laser induced modifications in quartz*, Applied Physics A **76**, 309 (2003).
[80] P. T. Mannion, J. Magee, E. Coyne, G. M. O'Connor, and T. J. Glynn, *The effect of damage accumulation behaviour on ablation thresholds and damage morphology in ultrafast laser micro-machining of common metals in air*, Applied Surface Science **233**, 275 (2004).
[81] D. V. Tran, H. Y. Zheng, Y. C. Lam, V. M. Murukeshan, J. C. Chai, and D. E. Hardt, *Femtosecond laser-induced damage morphologies of crystalline silicon by sub-threshold pulses*, Optics and Lasers in Engineering **43**, 977 (2005).

[82] S. E. Kirkwood, A. C. V. Popta, Y. Y. Tsui, and R. Fedosejevs, *Single and multiple shot near-infrared femtosecond laser pulse ablation thresholds of copper*, Applied Physics A **81**, 729 (2005).
[83] S. Baudach, J. Bonse, J. Kruger, and W. Kautek, *Ultrashort pulse laser ablation of polycarbonate and polymethylmethacrylate*, Applied Surface Science **154-155**, 555 (2000).
[84] D. Ashkenasi, M. Lorenz, R. Stoian, and A. Rosenfeld, *Surface damage threshold and structuring of dielectrics using femtosecond laser pulses: the role of incubation*, Applied Surface Science **150**, 101 (1999).
[85] A. Rosenfeld, M. Lorenz, R. Stoian, and D. Ashkenasi, *Ultrashort-laser-pulse damage threshold of transparent materials and the role of incubation*, Applied Physics A **69**, S373 (1999).
[86] H. O. Jeschke, M. E. Garcia, M. Lenzner, J. Bonse, J. Kruger, and W. Kautek, *Laser ablation thresholds of silicon for different pulse durations: theory and experiment*, Applied Surface Science **197-198**, 839 (2002).
[87] N. Yasumaru, K. Miyazaki, and J. Kiuchi, *Femtosecond-laser-induced nanostructure formed on hard thin films TiN and DLC*, Applied Physics A **76**, 983 (2003).
[88] C. B. Schaffer, A. Brodeur, and E. Mazur, *Laser-induced breakdown and damage in bulk transparent materials induced by tightly focused femtosecond laser pulses*, Measurement Science and Technology **12**, 1784 (2001).
[89] S. Martin, A. Hertwig, M. Lenzner, J. Kruger, and W. Kautek, *Spot-size dependence of the ablation threshold in dielectrics for femtosecond laser pulses*, Applied Physics A **77**, 883 (2003).
[90] T. Q. Jia, R. X. Li, Z. Liu, and Z. Z. Xu, *Thresholds of femtosecond laser-induced damage in transparent materials*, Applied Physics A **74**, 503 (2002).
[91] K. K. Thornber, *Applications of scaling to problems in high-field electronic transport*, Journal of Applied Physics **52**, 279 (1981).
[92] B. Rethfeld, *Free-electron generation in laser irradiated dielectrics*, Physical Review B **73**, 035101 (2006).
[93] S. Z. Xu, T. Q. Jia, H. Y. Sun, C. B. Li, X. X. Li, D. H. Feng, J. R. Qiu, and Z. Z. Xu, *Mechanisms of femtosecond laser-induced breakdown and damage in MgO*, Optics Communications **259**, 274 (2006).
[94] F. Quere, S. Guizard, and P. Martin, *Time-resolved study of laser induced breakdown in dielectrics*, Europhysics Letters **56**, 138 (2001).
[95] C. B. Schaffer, A. Broduer, J. F. Garcia, and E. Mazur, *Micromachining bulk glass by use of femtosecond laser pulses with nanojoule energy*, Optics Letters **26**, 93 (2001).
[96] B. Rethfeld, *Unified model for the free-electron avalanche in laser irradiated dielectrics*, Physical Review Letters **92**, 187401 (2004).
[97] E. G. Gamaly, A. V. Rode, V. T. Tikhonchuk, and B. Luther-Davies, *Electrostatic mechanism of ablation by femtosecond lasers*, Applied Surface Science **197-198**, 699 (2002).
[98] E. G. Gamaly, A. V. Rode, V. T. Tikhonchuk, and B. Luther-Davies, *Ablation of solids by femtosecond lasers: ablation mechanism and ablation thresholds for metals and dielectrics*, Physics of Plasmas **9**, 949 (2002).

[99] R. Stoian, A. Rosenfeld, D. Ashkenasi, I. V. Hertel, N. M. Bulgakova, and E. E. B. Campbell, *Surface charging and impulsive ion ejection during ultrashort pulsed laser ablation*, Physical Review Letters **88**, 097603 (2002).
[100] R. Stoian, D. Ashkenasi, A. Rosenfeld, and E. E. B. Campbell, *Coulomb explosion in ultrashort pulsed laser ablation of Al_2O_3* Physical Review B **62**, 13168 (2000).
[101] N. M. Bulgakova, R. Stoian, A. Rosenfeld, I. V. Hertel, and E. E. B. Campbell, *Electronic transport and consequences for material removal in ultrafast pulsed laser ablation of materials*, Physical Review B **69**, 054102 (2004).
[102] S. S. Mao, F. Quere, S. Guizard, X. Mao, R. E. Russo, G. Petite, and P. Martin, *Dynamics of femtosecond laser interactions with dielectrics*, Applied Physics A **79**, 1695 (2004).
[103] A. Kaiser, B. Rethfeld, M. Vicanek, and G. Simon, *Microscopic processes in dielectrics under irradiation by subpicosecond laser pulses*, Physical Review B **61**, 11437 (2000).
[104] T. Elsaesser, J. Shah, L. Rota, and P. Lugli, *Initial thermalization of photo-excited carriers in GaAs studied by femtosecond luminescence spectroscopy*, Physical Review Letters **66**, 1757 (1991).
[105] K. Sokolowski-Tinten, J. Bialkowski, and D. von der Linde, *Ultrafast laser-induced order-disorder transistions in semiconductors*, Physical Review B **51**, 14186 (1995).
[106] B. Rethfeld, K. Sokolowski-Tinten, D. von der Linde, and S. I. Anisimov, *Timescales in the response of materials to femtosecond laser excitation*, Applied Physics A **79**, 767 (2004).
[107] A. Rousse, C. Rischel, S. Fourmaux, I. Uschmann, S. Sebban, G. Grillon, P. Balcou, E. Forster, J. P. Geindre, P. Auderbert, J. C. Gauthier, and D. Hulin, *Non-thermal melting in semiconductors measured at femtosecond resolution*, Nature **410**, 65 (2001).
[108] J. Hohlfeld, S.-S. Wellershoff, J. Gudde, U. Conrad, V. Jahnke, and E. Matthias, *Electron and lattice dynamics following optical excitation of metals*, Chemical Physics **251**, 237 (2000).
[109] V. Schmidt, W. Husinsky, and G. Betz, *Ultrashort laser ablation of metals: pump-probe experiments, the role of ballistic electrons, and the two-temperature model*, Applied Surface Science **197-198**, 145 (2002).
[110] S.-S. Wellershoff, J. Hohlfeld, J. Gudde, and E. Matthias, *The role of electron-phonon coupling in femtosecond laser damage of metals*, Applied Physics A **69**, S99 (1999).
[111] J. Gudde, J. Hohlfeld, J. G. Mullter, and E. Matthias, *Damage threshold dependence on electron-phonon coupling in Au and Ni films*, Applied Surface Science **127-129**, 40 (1998).
[112] V. Schmidt, W. Husinsky, and G. Betz, *Dynamics of laser desorption and ablation of metals at the threshold on the femtosecond time scale*, Physical Review Letters **85**, 3516 (2000).
[113] Y. Hirayama, and M. Obara, *Heat-affected zone and ablation rate of copper ablated with femtosecond laser*, Journal of Applied Physics **97**, 064903 (2005).

[114] A. E. Wynne, and B. C. Stuart, *Rate dependence of short-pulse laser ablation of metals in air and vacuum*, Applied Physics A **76**, 373 (2003).
[115] Q. Feng, Y. N. Picard, H. Liu, S. M. Yalisove, G. Mourou, and T. M. Pollock, *Femtosecond laser machining of a single-crystal superalloy*, Scripta Materialia **53**, 511 (2005).
[116] S. Ma, J. P. McDonald, B. Tryon, S. M. Yalisove, and T. M. Pollock, *Femtosecond laser ablation regimes in a single crystal superalloy*, Metallurgical and Material Transactions A **In press** (2007).
[117] T. Kim, H. S. Kim, M. Hetterich, D. Jones, J. M. Girkin, E. Bente, and M. D. Dawson, *Femtosecond laser machining of gallium nitride*, Materials Science and Engineering **B82**, 262 (2001).
[118] J. Bonse, G. Bachelier, J. Siegel, and J. Solis, *Time- and space-resolved dynamics of melting, ablation, and solidification phenomena induced by femtosecond laser pulses in germanium*, Physical Review B **74**, 134106 (2006).
[119] D. Ramanathan, and P. A. Molian, *Micro- and sub-micromachining of type IIa single crystal diamond using a Ti:sapphire femtosecond laser*, Journal of Manufacturing Science and Engineering **124**, 389 (2002).
[120] S. Preuss, and M. Stuke, *Subpicosecond ultraviolet laser ablation of diamond: Nonlinear properties at 248 nm and time-resolved characterization of ablation dynamics*, Applied Physics Letters **67**, 338 (1995).
[121] M. Mero, J. Liu, W. Rudolph, D. Ristau, and K. Starke, *Scaling laws of femtosecond laser pulse induced breakdown in oxide films*, Physical Review B **71**, 115109 (2005).
[122] J. Bonse, S. M. Wiggins, J. Solis, and T. Lippert, *Phase change dynamics in a polymer thin film upon femtosecond and picosecond laser irradiation*, Applied Surface Science **247**, 440 (2005).
[123] Y. Dong, H. Sakata, and P. Molian, *Femtosecond pulsed laser ablation of diamond-like carbon films on silicon*, Applied Surface Science **252**, 352 (2005).
[124] C. Li, D. Feng, T. Jia, H. Sun, X. Li, S. Xu, X. Wang, and Z. Xu, *Ultrafast dynamics in ZnO thin films irradiated by femtosecond lasers*, Solid State Communications **136**, 389 (2005).
[125] M. Park, B. H. Chon, H. S. Kim, S. C. Jeoung, D. Kim, J.-I. Lee, H. Y. Chu, and H. R. Kim, *Ultrafast laser ablation of indium tin oxide thin films for organic light-emitting diode applications*, Optics and Lasers in Engineering **44**, 138 (2006).
[126] Z. Wu, H. Jiang, Z. Zhang, Q. Sun, H. Yang, and Q. Gong, *Morphological investigation at the front and rear surfaces of fused silica processed with femtosecond laser pulses in air*, Optics Express **10**, 1244 (2002).
[127] A. Ben-Yakar, and R. L. Byer, *Femtosecond laser ablation properties of borosilicate glass*, Journal of Applied Physics **96**, 5316 (2004).
[128] A. Ben-Yakar, R. L. Byer, A. Harkin, J. Ashmore, H. A. Stone, M. Shen, and E. Mazur, *Morphology of femtosecond-laser-ablated borosilicate glass surfaces*, Applied Physics Letters **83**, 3030 (2003).
[129] J. Kruger, P. Meja, M. Autric, and W. Kautek, *Femtosecond pulse laser ablation of anodic oxide coatings on aluminum alloys with on-line acoustic observation*, Applied Surface Science **186**, 374 (2002).

[130] F. Costache, S. Kouteva-Arguirova, and J. Reif, *Sub-damage-threshold femtosecond laser ablation from crystalline Si: surface nanostructures and phase transformation*, Applied Physics A **79**, 1429 (2004).
[131] T. Matsumura, A. Kazama, and T. Yagi, *Generation of debris in the femtosecond laser machining of a silicon substrate*, Applied Physics A **81**, 1393 (2005).
[132] N. Barsch, K. Korber, A. Ostendorf, and K. H. Tonshoff, *Ablation and cutting of planar silicon devices using femtosecond laser pulses*, Applied Physics A **77**, 237 (2003).
[133] N. N. Nedialkov, S. E. Imamova, and P. A. Atanasov, *Ablation of metals by ultrashort laser pulses*, Journal of Physics D: Applied Physics **37**, 638 (2004).
[134] R. Le Harzic, D. Breitling, M. Weikart, S. Sommer, C. Fohl, S. Valette, C. Donnet, E. Audouard, and F. Dausinger, *Pulse width and energy influence on laser micromachining of metals in a range of 100 fs to 5 ps*, Applied Surface Science **249**, 322 (2005).
[135] R. Le Harzic, D. Breitling, M. Weikart, S. Sommer, C. Fohl, S. Valette, C. Donnet, E. Audouard, and F. Dausinger, *Ablation comparison with low and high energy densities for Cu and Al with ultra-short laser pulses*, Applied Physics A **80**, 1589 (2005).
[136] W. Perrie, M. Gill, G. Robinson, P. Fox, and W. O'Neill, *Femtosecond laser micro-structuring of aluminium under helium*, Applied Surface Science **230**, 50 (2004).
[137] L. Urech, T. Lippert, A. Wokaun, S. Martin, H. Madebach, and J. Kruger, *Removal of doped poly(methylmetacrylate) from tungsten and titanium substrates by femto- and nanosecond laser cleaning*, Applied Surface Science **252**, 4754 (2006).
[138] D. Kawamura, A. Takita, Y. Hayasaki, and N. Nishida, *Method for reducing debris and thermal destruction in femtosecond laser processing by applying transparent coating*, Applied Physics A **82**, 523 (2006).
[139] X. Ni, C.-Y. Wang, L. Yang, L. Jianping, L. Chai, W. Jia, R. Zhang, and Z. Zhang, *Parametric study on femtosecond laser pulse ablation of Au films*, Applied Surface Science **253**, 1616 (2006).
[140] X. Zhu, D. M. Villeneuve, A. Y. Naumov, S. Nikumb, and P. B. Corkum, *Experimental study of drilling sub-10 μm holes in thin metal foils with femtosecond laser pulses*, Applied Surface Science **152**, 138 (1999).
[141] G. Zhang, D. Gu, X. Jiang, Q. Chen, and F. Gan, *Femtosecond laser pulse irradiation of Sb-rich AgInSbTe films: scanning electron microscopy and atomic force microscopy investigations*, Applied Physics A **80**, 1039 (2005).
[142] J. Koch, F. Korte, T. Bauer, C. Fallnich, A. Ostendorf, and B. N. Chichkov, *Nanotexturing of gold films by femtosecond laser-induced melt dynamics*, Applied Physics A **81**, 325 (2005).
[143] Y. N. Picard, in *Materials Science and Engineering* (University of Michigan, Ann Arbor, 2006).
[144] D. B. Marshall, and A. G. Evans, *Measurement of adherence of residually stressed thin films by indentation. I. Mechanics of interface delamination*, Journal of Applied Physics **56**, 2632 (1984).

[145] H. M. Jensen, *Energy release rates and stability of straight-sided, thin-film delaminations*, Acta Metallurgica Materialia **41**, 601 (1993).
[146] H. M. Jensen, and M. D. Thouless, *Effects of residual stresses in the blister test*, International Journal of Solids and Structures **30**, 779 (1993).
[147] M. P. De Boer, and W. W. Gerberich, *Microwedge indentation of the thin film fine line - I. Mechanics*, Acta Materialia **44**, 3169 (1996).
[148] M. P. De Boer, and W. W. Gerberich, *Microwedge indentation of the thin film fine line - II. Experiment*, Acta Materialia **44**, 3177 (1996).
[149] M. W. Moon, H. M. Jensen, J. W. Hutchinson, K. H. Oh, and A. G. Evans, *The characterization of telephone cord buckling of compressed thin films on substrates*, Journal of the Mechanics and Physics of Solids **50**, 2355 (2002).
[150] M. W. Moon, K.-R. Lee, K. H. Oh, and J. W. Hutchinson, *Buckle delamination on patterned substrates*, Acta Materialia **52**, 3151 (2004).
[151] S. Faulhaber, C. Mercer, M. W. Moon, J. W. Hutchinson, and A. G. Evans, *Buckling delamination in compressed multilayers on curved substrates with accompanying ridge cracks*, Journal of the Mechanics and Physics of Solids **54**, 1004 (2006).
[152] K. Xiao, Z. S. Guan, G. J. Wang, D. B. Zhu, and Y. R. Wang, *Laser-induced wavy pattern formation in metal thin films*, Applied Physics Letters **85**, 1934 (2004).
[153] J. R. Serrano, and D. G. Cahill, *Micron-scale buckling of SiO_2 on Si*, Journal of Applied Physics **92**, 7606 (2002).
[154] J. Bonse, S. Baudach, W. Kautek, E. Welsh, and J. Kruger, *Femtosecond laser induced damage of a high reflecting mirror*, Thin Solid Films **408**, 297 (2002).
[155] J. Bonse, P. Rudolph, J. Kruger, S. Baudach, and W. Kautek, *Femtosecond pulse laser processing of TiN on silicon*, Applied Surface Science **154-155**, 659 (2000).
[156] H. M. van Driel, J. E. Sipe, and J. F. Young, *Laser-induced periodic surface structure on solids: a universal phenomenon*, Physical Review Letters **49**, 1955 (1982).
[157] Z. Guosheng, P. M. Fauchet, and A. E. Siegman, *Growth of spontaneous periodic surface structures on solids during laser illumination*, Physical Review B **26**, 5366 (1982).
[158] F. Costache, M. Henyk, and J. Reif, *Modification of dielectric surfaces with ultra-short laser pulses*, Applied Surface Science **186**, 352 (2002).
[159] A. Y. Vorobyev, V. S. Makin, and C. Guo, *Periodic ordering of random surface nanostructures induced by femtosecond laser pulses on metals*, Journal of Applied Physics **101**, 034903 (2007).
[160] J. E. Sipe, J. F. Young, J. S. Preston, and H. M. van Driel, *Laser-induced periodic surface structure. I. Theory*, Physical Review B **27**, 1141 (1983).
[161] V. I. Emel'yanov, and D. V. Babak, *Defect capture under rapid solidification of the melt produced by the action of femtosecond laser pulses and formation of periodic surface structures on a semiconductor surface*, Applied Physics A **74**, 797 (2002).
[162] J. Reif, F. Costache, M. Henyk, and S. V. Pandelov, *Ripples revisited: non-classical morphology at the bottom of femtosecond laser ablation craters in transparent dielectrics*, Applied Surface Science **197**, 891 (2002).

[163] M. A. Sheehy, L. Winston, J. E. Carey, C. M. Friend, and E. Mazur, *Role of the background gas in the morphology and optical properties of laser-microstructured silicon*, Chemistry of Materials **17**, 3582 (2005).
[164] S. Woutersen, U. Emmerichs, and H. J. Bakker, *Femtosecond mid-IR pump-probe microscopy of liquid water: Evidence for a two-component structure*, Science **278**, 658 (1997).
[165] T. Brixner, J. Stenger, H. M. Vaswani, M. Cho, R. E. Blankenship, and G. R. Fleming, *Two-dimensional spectroscopy of electronic couplings in photosynthesis*, Nature **434**, 625 (2005).
[166] V. Margetic, T. Ban, O. Samek, F. Leis, K. Niemax, and R. Hergenroder, *Shock-wave velocity of a femtosecond-laser-induced plasma*, Czechoslovak Journal of Physics **54**, 423 (2004).
[167] T. W. Murray, and J. W. Wagner, *Laser generation of acoustic waves in the ablative regime*, Journal of Applied Physics **85**, 2031 (1999).
[168] D. Perez, and L. J. Lewis, *Molecular-dynamics study of ablation of solids under femtosecond laser pulses*, Physical Review B **67**, 184102 (2003).
[169] L. I. Sedov, *Similarity and dimensional methods in mechanics* (Academic Press, New York, 1959).
[170] G. I. Taylor, *The formation of a blast wave by a very intense explosion. 2. The atomic explosion of 1945*, Proceedings of the Royal Society of London A **201**, 175 (1950).
[171] J. Gruber, J. Heitz, H. Strasser, D. Bauerle, and N. Ramaseder, *Rapid in-situ analysis of liquid steel by laser induced breakdown spectroscopy*, Spectrochimica Acta Part B: Atomic Spectroscopy **56**, 685 (2001).
[172] A. K. Rai, F.-Y. Yueh, and J. P. Singh, *Laser-induced breakdown spectroscopy of molten aluminum alloy*, Applied Optics **42**, 2078 (2003).
[173] C. Aragon, J. A. Aguilera, and J. Campos, *Determination of carbon contenct in molten steel using laser-induced breakdown spectroscopy*, Applied Spectroscopy **47**, 606 (1993).
[174] K. L. Eland, D. N. Stratis, D. M. Gold, S. R. Goode, and S. M. Angel, *Energy dependence of emission intensity and temperature in LIBS plasma using femtosecond excitation*, Applied Spectroscopy **55**, 286 (2001).
[175] V. Sturm, L. Peter, and R. Noll, *Steel analysis with laser-induced breakdown spectrometry in the vacuum ultraviolet*, Applied Spectroscopy **54**, 1275 (2000).
[176] I. V. Cravetchi, M. T. Taschuk, Y. Y. Tsui, and R. Fedosejevs, *Evaluation of femtosecond LIBS for spectrochemical microanalysis of aluminum alloys*, Analytical and Bioanalytical Chemistry **385**, 287 (2006).
[177] B. Le Drogoff, J. Margot, M. Chaker, M. Sabsabi, O. Barthemlemy, T. W. Johnston, S. Laville, F. Vidal, and Y. von Kaenel, *Temporal characterization of femtosecond laser pulses induced plasma for spectrochemical analysis of aluminum alloys*, Spectrochimica Acta Part B: Atomic Spectroscopy **56**, 987 (2001).
[178] V. Margetic, M. Bolshov, A. Stockhaus, K. Niemax, and R. Hergenroder, *Depth profiling of multi-layer samples using femtosecond laser ablation*, Journal of Analytic Atomic Spectrometry **16**, 616 (2001).

[179] B. Le Drogoff, F. Vidal, Y. Von Kaenel, M. Chaker, T. W. Johnston, S. Laville, M. Sabsabi, and J. Margot, *Ablation of aluminum thin films by ultrashort laser pulses*, Journal of Applied Physics **89**, 8247 (2001).
[180] D. Grojo, J. Hermann, and A. Perrone, *Plasma analyses during femtosecond laser ablation of Ti, Zr, and Hf*, Journal of Applied Physics **97**, 063306 (2005).
[181] K. Amal, S. H. Elnaby, V. Palleschi, and M. A. Harith, *Comparison between single- and double-pulse LIBS at different air pressures on silicon target*, Applied Physics B: Lasers and Optics **83**, 651 (2006).
[182] M. Milan, P. Lucena, L. M. Cabalin, and J. J. Laserna, *Depth profiles of phosphorus in photonic-grade silicon using laser-induced breakdown spectrometry*, Applied Spectroscopy **52**, 444 (1998).
[183] C. F. Su, S. M. Feng, J. P. Singh, F. Y. Yuen, J. T. Rigsby, D. L. Monts, and R. L. Cook, *Glass composition measurement using laser induced breakdown spectrometry*, Glass Technology **41**, 16 (2000).
[184] N. Carmona, M. Oujja, S. Gaspard, M. Garcia-Heras, M. A. Villegas, and M. Castillejo, *Lead determination in glasses by laser-induced breakdown spectroscopy*, Spectrochimica Acta Part B: Atomic Spectroscopy **62**, 94 (2007).
[185] L. Dudragne, P. Adam, and J. Amouroux, *Time-resolved laser-induced breakdown spectroscopy: application for qualitative and quantitative detection of fluorine, chlorine, sulfur, and carbon in air*, Applied Spectroscopy **52**, 1321 (1998).
[186] J. E. Carranza, B. T. Fisher, G. D. Yoder, and D. W. Hahn, *On-line analysis of ambient air aerosols using laser-induced breakdown spectroscopy*, Spectrochimica Acta Part B: Atomic Spectroscopy **56**, 851 (2001).
[187] A. Ciucci, M. Corsi, V. Palleschi, S. Rastelli, A. Salvetti, and E. Tognoni, *New procedure for quantitative elemental analysis by laser-induced plasma spectroscopy*, Applied Spectroscopy **53**, 960 (1999).
[188] V. Margetic, A. Pakulev, A. Stockhaus, M. Bolshov, K. Niemax, and R. Hergenroder, *A comparison of nanosecond and femtosecond laser-induced plasma spectroscopy of brass samples*, Spectrochimica Acta Part B: Atomic Spectroscopy **55**, 1771 (2000).
[189] K. L. Eland, D. N. Stratis, T. S. Lai, M. A. Berg, S. R. Goode, and S. M. Angel, *Some comparisons of LIBS measurements using nanosecond and picosecond laser pulses*, Applied Spectroscopy **55**, 279 (2001).
[190] S. M. Angel, D. N. Stratis, K. L. Eland, T. S. Lai, M. A. Berg, and D. M. Gold, *LIBS using dual- and ultra-short laser pulses*, Analytical Chemistry **369**, 320 (2001).
[191] J. Uebbing, J. Brust, W. Sdorra, F. Leis, and K. Niemax, *Reheating of a laser-produced plasma by a 2nd pulse laser*, Applied Spectroscopy **45**, 1419 (1991).
[192] J. Scaffidi, J. Pender, W. Pearman, S. R. Goode, B. W. Colston, J. C. Carter, and S. M. Angel, *Dual-pulse laser-induced breakdown spectroscopy with combinations of femtosecond and nanosecond laser pulses*, Applied Optics **42**, 6099 (2003).
[193] D. N. Stratis, K. L. Eland, and S. M. Angel, *Dual-pulse LIBS using a pre-ablation spark for enhanced ablation and emission*, Applied Spectroscopy **54**, 1270 (2000).

[194] D. N. Stratis, K. L. Eland, and S. M. Angel, *Enhancement of aluminum, titanium, and iron in glass using pre-ablation spark dual-pulse LIBS*, Applied Spectroscopy **54**, 1719 (2000).
[195] D. N. Stratis, K. L. Eland, and S. M. Angel, *Effect of pulse delay time on a pre-ablation dual-pulse LIBS plasma*, Applied Spectroscopy **55**, 1297 (2001).
[196] G. Cristoforetti, S. Legnaioli, L. Pardini, V. Palleschi, A. Salvetti, and E. Tognoni, *Spectroscopic and shadowgraphic analysis of laser induced plasmas in the orthogonal double pulse pre-ablation configuration*, Spectrochimica Acta Part B: Atomic Spectroscopy **61**, 340 (2006).
[197] M. A. Ismail, G. Cristoforetti, S. Legnaioli, L. Pardini, V. Palleschi, A. Salvetti, E. Tognoni, and M. A. Harith, *Comparison of detection limits for two metallic matricies of laser-induced breakdown spectroscopy in the single and double-pulse configurations*, Analytical and Bioanalytical Chemistry **385**, 316 (2006).
[198] C. Gautier, P. Fichet, D. Menut, J. L. Lacour, D. L'Hermite, and J. Dubessy, *Main parameters influencing the double-pulse laser-induced breakdown spectroscopy in the collinear beam geometry*, Spectrochimica Acta Part B: Atomic Spectroscopy **60**, 792 (2005).
[199] A. Santagata, A. De Bonis, P. Villani, R. Teghil, and G. P. Parisi, *Fs/ns-dual-pulse orthogonal geometry plasma plume reheating for copper-based-alloys analysis*, Applied Surface Science **252**, 4685 (2006).
[200] V. I. Babushok, F. C. DeLucia, J. L. Gottfried, C. A. Munson, and A. W. Miziolek, *Double pulse laser ablation and plasma: Laser induced breakdown spectroscopy signal enhancement*, Spectrochimica Acta Part B: Atomic Spectroscopy **61**, 999 (2006).
[201] J. Scaffidi, S. M. Angel, and D. A. Cremers, *Emission enhancement mechanisms in dual-pulse LIBS*, Analytical Chemistry **78**, 24 (2006).
[202] J. Scaffidi, W. Pearman, J. C. Carter, and S. M. Angel, *Observations in collinear femtosecond-nanosecond dual-pulsed laser-induced breakdown spectroscopy*, Applied Spectroscopy **60**, 65 (2006).
[203] J. Scaffidi, W. Pearman, M. Lawrence, J. C. Carter, B. W. Colston, and S. M. Angel, *Spatial and temporal dependence of interspark interactions in femtosecond-nanosecond dual-pulse laser-induced breakdown spectroscopy*, Applied Optics **43**, 5243 (2004).
[204] J. Scaffidi, W. Pearman, J. C. Carter, B. W. Colston, and S. M. Angel, *Effects of sample temperature in femtosecond single-pulse laser-induced breakdown spectroscopy*, Applied Optics **43**, 2786 (2004).
[205] H. Matsuta, and K. Wagatsuma, *Emission characteristics of a low-pressure laser-induced plasma: selective excitation of ionic emission lines of copper*, Applied Spectroscopy **56**, 1165 (2002).
[206] S. Yalcin, Y. Y. Tsui, and R. Fedosejevs, *Pressure dependence of emission intensity in femtosecond laser-induced breakdown spectroscopy*, Journal of Analytic Atomic Spectrometry **19**, 1295 (2004).
[207] P. Colella, and P. R. Woodward, *The piecewise parabolic method (PPM) for gas-dynamical simulations*, Journal of Computational Physics **54**, 174 (1984).
[208] M. J. Berger, and P. Colella, *Local adaptive mesh refinement for shock hydrodynamics*, Journal of Computational Physics **82**, 64 (1989).

[209] D. deZeeuw, and K. G. Powell, *An adaptive refined cartesian mesh solver for the euler equations*, Journal of Computational Physics **104**, 56 (1993).
[210] A. M. Rubenchik, M. D. Feit, M. D. Perry, and J. T. Larsen, *Numerical simulation of ultra-short laser pulse energy deposition and bulk transportaton for material processing*, Applied Surface Science **129**, 193 (1998).
[211] J. T. Larsen, and S. M. Lane, *HYADES - A plasma hydrodynamics code for dense plasma studies*, Quant. Spectrosc. Radiat. Transfer **51**, 179 (1994).
[212] T. E. Itina, J. Hermann, P. Delaporte, and M. Sentis, *Modeling of metal ablation induced by ultrashort laser pulses*, Thin Solid Films **453-454**, 513 (2004).
[213] P. A. Atanasov, N. N. Nedialkov, S. E. Imamova, A. Ruf, H. Hugel, F. Dausinger, and P. Berger, *Laser ablation of Ni by ultrashort pulses: molecular dynamics simulation*, Applied Surface Science **186**, 369 (2002).
[214] N. N. Nedialkov, P. A. Atanasov, S. E. Imamova, A. Ruf, P. Berger, and F. Dausinger, *Dynamics of the ejected material in ultra-short laser ablation of metals*, Applied Physics A **79**, 1121 (2004).
[215] N. N. Nedialkov, S. E. Imamova, P. A. Atanasov, P. Berger, and F. Dausinger, *Mechanism of ultrashort laser ablation of metals: molecular dynamics simulation*, Applied Surface Science **247**, 243 (2005).
[216] S. Amoruso, R. Bruzzese, M. Vitiello, N. N. Nedialkov, and P. A. Atanasov, *Experimental and theoretical investigations of femtosecond laser ablation of aluminum in vacuum*, Journal of Applied Physics **98**, 044907 (2005).
[217] C. Cheng, and X. Xu, *Mechanisms of decomposition of metal during femtosecond laser ablation*, Physical Review B **72**, 165415 (2005).
[218] N. M. Bulgakova, and I. M. Bourakov, *Phase explosion under ultrashort pulsed laser ablation: modeling with analysis of metastable state of melt*, Applied Surface Science **197-198**, 41 (2002).
[219] B. Fryxell, K. Olsen, P. Ricker, F. X. Timmes, M. Zingale, D. Q. Lamb, P. MacNeice, R. Rosner, J. W. Turan, and H. Tufo, *FLASH: An adaptice mesh hydrodynamics code for modeling astrophysical thermonuclear flashes*, Astrophysical Journal Supplement Series **131**, 273 (2000).
[220] P. A. Rosen, J. M. Foster, R. J. R. Williams, B. H. Wilde, R. F. Coker, B. Blue, T. S. Perry, P. Hartigan, R. P. Drake, K. Dannenberg, A. M. Khokhlov, A. Frank, and J. P. Knauer, *Laboratory-astrophysics jet experiments at the omega laser facility*, Journal De Physique IV **133**, 1019 (2006).
[221] J. M. Liu, *Simple technique for measurements of pulsed Gaussian-beam spot sizes*, Optics Letters **7** (1982).
[222] Y. J. Chabal, H. G. Raghavacharik, and V. A. Burrows, *Infrared-spectroscopy of Si(111) and Si(100) surfaces after HF treatment - Hydrogen termination and surface-morphology*, Journal of Vacuum Science and Technology **7**, 2104 (1989).
[223] Y. J. Chabal, H. G. Raghavacharik, and J. C. Tully, *Infrared spectroscopy of H-terminated silicon surfaces*, International Journal of Modern Physics B **7**, 1031 (1993).
[224] P. E. Thompson, M. E. Twigg, D. J. Godbey, K. D. Hobart, and D. S. Simons, *Low-temperature cleaning processes for Si molecular-beam epitaxy*, Journal of Vacuum Science and Technology B **11**, 1077 (1993).

[225] S. Nolte, C. Momma, G. Kamlage, A. Ostendorf, C. Fallnich, F. Von Alvensleben, and H. Welling, *Polarization effects in ultrashort-pulse laser drilling*, Applied Physics A **68**, 563 (1999).
[226] R. F. Smith, *Microscopy and photomicrography: a working manual* (CRC Press, Boca Raton, 1994).
[227] D. Murphy, *Differential interference contrast (DIC) microscopy and modulation contrast microscopy: Fundamentals of Light Microscopy and Digital Imaging* (Wiley-Liss, New York, 2001).
[228] J. Reader, and C. H. Corliss, in *CRC Handbook of Chemistry and Physics*, edited by D. R. Lide (CRC Press, Boca Raton, 2007).
[229] R. P. Drake, *High Energy Density Physics* (Springer-Verlag, New York, 2006).
[230] R. D. Guenther, *Modern Optics* (Wiley, New York, 1990).
[231] G. R. Fowles, *Introduction to Modern Optics* (Dover, New York, 1975).
[232] J. Bloch, J. G. Mihaychuk, and H. M. Van Driel, *Electron photoinjection from silicon to ultrathin SiO_2 films via ambient oxygen*, Physical Review Letters **77**, 920 (1996).
[233] J. H. Weaver, and H. P. R. Frederikse, in *Handbook of Chemistry and Physics*, edited by D. R. Lide (CRC Press, Boca Raton, 2007).
[234] C. B. Schaffer, J. F. Garcia, and E. Mazur, *Bulk heating of transparent materials using a high-repetition-rate femtosecond laser*, Applied Physics A **76**, 351 (2003).
[235] M. Will, S. Nolte, B. N. Chichkov, and A. Tunnermann, *Optical properties of waveguides fabricated in fused silica by femtosecond laser pulses*, Applied Optics **41**, 4360 (2002).
[236] K. M. Davis, K. Miura, N. Sugimoto, and K. Hirao, *Writing waveguides in glass with a femtosecond laser*, Optics Letters **21**, 1729 (1996).
[237] J. W. Chan, T. R. Huser, S. H. Risbud, and D. M. Krol, *Structural changes in fused silica after exposure to focused femtosecond laser pulses*, Optics Letters **26**, 1726 (2001).
[238] S. Guizard, P. Martin, G. Petite, P. D'Oliveira, and P. Meynadier, *Time-resolved study of laser-induced colour centers in SiO_2*, Journal of Physics: Condens. Matter **8**, 1281 (1996).
[239] O. M. Efimov, K. Gabel, S. V. Garnov, L. B. Glebov, S. Grantham, M. Richardson, and M. J. Soileau, *Color-center generation in silicate glasses exposed to infrared femtosecond pulses*, Journal of the Optical Society of America B **15**, 193 (1998).
[240] A. Zoubir, M. Richardson, L. Canioni, A. Brocas, and L. Sarger, *Optical properties of infrared femtosecond laser-modified fused silica and appliation to waveguide fabrication*, Journal of the Optical Society of America B **22**, 2138 (2005).
[241] A. Zoubir, C. Rivero, R. Grodsky, K. Richardson, M. Richardson, T. Cardinal, and M. Couzi, *Laser-induced defects in fused silica by femtosecond IR irradiation*, Physical Review B **73**, 224117 (2006).
[242] M. Stadtmueller, *Mechanical Stress of CVD-dielectrics*, Journal of the Electrochemical Society **139**, 3669 (1992).

[243] S. C. H. Lin, and I. Pugacz-Muraszkiewicz, *Local stress measurement in thin thermal SiO_2 films on Si substrates*, Journal of Applied Physics **43**, 119 (1972).
[244] E. Kobeda, and E. A. Irene, *A measurement of intrinsic SiO_2 film stress resulting from low temperature thermal oxidation of Si*, Journal of Vacuum Science and Technology B **4**, 720 (1986).
[245] M. J. Cordhill, D. F. Bahr, N. R. Moody, and W. W. Gerberich, *Adhesion measurements using telephone cord buckles*, Materials Science and Engineering A **443**, 150 (2007).
[246] G. Gille, and B. Rau, *Buckling instability and adhesion of carbon layers*, Thin Solid Films **120**, 109 (1984).
[247] I. Langmuir, *Vapor pressures, evaporation, condensation and adsorption*, Journal of the American Chemical Society **54**, 2797 (1932).
[248] S. Hjerten, and M. Kiessling-Johansson, *High-performance displacement electrophoresis in 0.025 - 0.050 mm capillaries coated with a polymer to supress adsorption and electroendosmosis*, Journal of Chromatography **550**, 811 (1991).
[249] A. Manz, D. J. Harrison, E. M. J. Verpooorte, J. C. Fettinger, A. Paulus, H. Ludi, and H. M. WIdmer, *Planar chips technology for miniaturization and integration of seperation techniques into monitoring systems: Capillary electrophoresis on a chip*, Journal of Chromatography **593**, 253 (1992).
[250] E. B. Cummings, and A. K. Singh, *Dielectrophoresis in microchips containing arrays of insulating posts: Theoretical and experimental results*, Analytical Chemistry **75**, 4724 (2003).
[251] J. O. Tegenfeldt, C. Prinz, H. Cao, R. L. Huang, R. H. Austin, S. Y. Chou, E. C. Cox, and J. C. Sturm, *Micro- and nanofluidics for DNA analysis*, Analytical and Bioanalytical Chemistry **378**, 1678 (2004).
[252] D. J. Harrison, P. G. Glavina, and A. Manz, *Towards miniturized electrophoresis and chemical-analysis systems on silicon - an alternative to chemical sensors*, Sensors and Actuators B - Chemical **10**, 107 (1993).
[253] A. Rasmussen, M. Gaitan, L. E. Locascio, and M. E. Zaghloul, *Fabrication techniques to realize CMOS-compatible microfluidic microchannels*, Journal of Microelectromechanical Systems **10**, 286 (2001).
[254] D. Mijatovic, J. C. T. Eijkel, and A. van den Berg, *Technologies for nanofluidic systems: top-down vs. bottom-up - a review*, Lab on a Chip **5**, 492 (2005).
[255] D. J. Hwang, T. Y. Choi, and C. P. Grigoropoulos, *Liquid-assisted femtosecond laser drilling of straight and three-dimensional microchannels in glass*, Applied Physics A **79**, 605 (2004).
[256] T. N. Kim, K. Campbell, A. Groisman, D. Kleinfeld, and C. B. Schaffer, *Femtosecond laser-drilled capillary integrated into a microfluidic device*, Applied Physics Letters **86**, 201106 (2005).
[257] K. Ke, E. F. Hasselbrink, and A. J. Hunt, *Rapidly prototyped three dimensional nanofluidic channel network in glass substrates*, Analytical Chemistry **77**, 5083 (2005).
[258] D. Gomez, I. Goenaga, I. Lizuain, and M. Ozaita, *Femtosecond laser ablation for microfluidics*, Optical Engineering **44**, 051105 (2005).
[259] J. W. Hutchinson, and Z. Suo, *Mixed-mode cracking in layered materials*, Advances in Applied Mechanics **29**, 63 (1992).

[260] J. Stringer, *Stress generation and relief in growing oxide films*, Corrosion Science **10**, 513 (1970).
[261] L. F. Henderson, *Handbook of shockwaves: Volume 2, Shock wave interactions and propagation* (Academic Press, San Diego, 2001), Vol. 2.
[262] Y. Hirayama, and M. Obara, *Heat effects of metals ablated with femtosecond laser pulses*, Applied Surface Science **197-198**, 741 (2002).
[263] M. Born, and E. Wolf, *Principles of optics* (Cambridge University Press, New York, 1999).
[264] W. Merzkirch, *Flow Visualization* (Academic Press, New York, 1974).
[265] A. E. Siegman, *Lasers* (University Science Books, Sausalito, CA, 1986).
[266] D. Halliday, R. Resnick, and J. Walker, *Fundamentals of Physics* New York, 1997).
[267] S. Ma, *Personal Communication*, (2007).
[268] Q. Feng, Y. N. Picard, J. P. McDonald, P. A. Van Rompay, S. M. Yalisove, and T. M. Pollock, *Femtosecond laser machining of single-crystal superalloys through thermal barrier coatings*, Materials Science and Engineering A **430**, 203 (2006).
[269] U. Schulz, C. Leyens, K. Fritscher, M. Peters, B. Saruhan-Brings, O. Lavigne, J. M. Dorvaux, M. Poulain, R. Mevrel, and M. L. Caliez, *Some recent trends in research and technology of advanced thermal barrier coatings*, Aerospace Science and Technology **7**, 73 (2003).
[270] D. K. Das, J. P. McDonald, S. M. Yalisove, and T. M. Pollock, *Depth profiling of a Pt-aluminide bond coat using femtosecond laser induced breakdown spectroscopy*, Submitted for publication (2007).
[271] X. L. Mao, and R. E. Russo, *Observation of plasma shielding by measuring transmitted and reflected laser pulse temporal profiles*, Applied Physics A **64**, 1 (1997).
[272] F. Korte, J. Koch, and B. N. Chichkov, *Formation of microbumps and nanojets on gold targets by femtosecond laser pulses*, Applied Physics A **79**, 879 (2004).
[273] Y. P. Meshcheryakov, and N. M. Bulgakova, *Thermoelastic modeling of microbump and nanojet formation on nanosize gold films under femtosecond laser irradiation*, Applied Physics A **82**, 363 (2006).
[274] N. Singh, D. R. Alexander, J. Schiffern, and D. Doerr, *Femtosecond laser production of metal surfaces having unique surface structures that are broadband absorbers*, Journal of Laser Applications **18**, 242 (2006).
[275] A. Y. Vorobyev, and C. L. Guo, *Effects of nanostrucutre covered femtosecond laser-induced periodic suface structures on optical absorptance of metals*, Applied Physics A **86**, 321 (2007).
[276] D. Lim, Y. Kamotani, B. Cho, J. Mazumder, and S. Takayama, *Fabrication of microfluidic mixers and artificial vasculatures using a high-brightness diode-pumped Nd:YAG laser direct write method*
Lab on a Chip **3**, 318 (2003).
[277] S. M. Kim, M. A. Burns, and E. F. Hasselbrink, *Electrokinetic protein preconcentration using a simple glass/poly(dimethylsiloxane) microfluidic chip*, Analytical Chemistry **78**, 4779 (2006).

[278] L. Tollier, and R. Fabbro, *Study of the laser-driven spallation process by the VISAR interferometry technique. II. Experiment and simulation of the spallation process*, Journal of Applied Physics **83**, 1231 (1998).
[279] CVI, *Dispersion equations for optical materials*, http://www.cvilaser.com/Common/PDFs/Dispersion_Equations.pdf, June 4, 2007
[280] G. E. Jellison, *Examination of thin SiO_2 films on Si using spectroscopic polarization modulation ellipsometry*, Journal of Applied Physics **69**, 7627 (1991).
[281] P. M. Fauchet, and K. D. Li, *The dielectric function of laser-produced molten Si*, Journal of Non-Crystalline Solids **97-98**, 1267 (1987).
[282] G. E. Jellison, and H. H. Burke, *The temperature dependence of the refractive index of silicon at elevated temperatures at several laser wavelengths*, Journal of Applied Physics **60**, 841 (1986).
[283] G. E. Jellison, and D. H. Lowndes, *Measurements of the optical properties of liquid silicon and germanium using nanosecond time-resolved ellipsometry*, Applied Physics Letters **51**, 352 (1987).
[284] T. B. Norris, *Lecture Notes: Classical Optics (EECS 537) Fall Term 2003*, (2003).